FAULT EVOLUTION AND EARTHQUAKES: A FINITE ELEMENT STUDY

A Dissertation

presented to

the Faculty of the Graduate School

University of Missouri-Columbia

In Partial Fulfillment

Of the Requirements for the Degree

Doctor of Philosophy

---

by
QINGSONG LI
Dr. Mian Liu, Dissertation Supervisor

MAY 2006

The undersigned, appointed by the Dean of the Graduate School, have examined the dissertation entitled

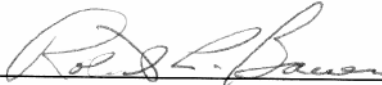# FAULT EVOLUTION AND EARTHQUAKES: A FINITE ELEMENT STUDY

Presented by Qingsong Li
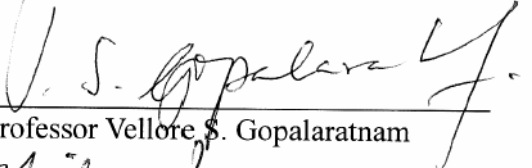
A candidate for the degree of Doctor of Philosophy

And hereby certify that in their opinion it is worthy of acceptance.
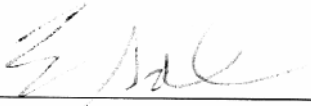
_____

Professor Mian Liu

_____

Professor Robert L. Bauer

_____

Professor Vellore S. Gopalaratnam

_____

Professor Michael B. Underwood

_____

Professor Eric Sandvol

ACKNOWLEDGEMENTS

Until now, I start to realize the heavy 'weight' of a PhD degree. I have been pursuing this degree for five and half years! In the past, I was focusing on studying, working and looking for positions, and did not notice the long time passed away. Fortunately, in this long PhD 'journey', I have made some nice contributions to scientific research in the field of active tectonics. And I am glad that my scientific work has been recognized by part of the geosciences community. All of these accomplishments are based on the help from many others who deserve recognition.

First, I would like to thank Professor Mian Liu, my advisor, who brought me to his lab, and gave me the freedom to work on projects that I am most interested in. He has spent a huge amount of time teaching me all aspects of scientific research. He teaches me how to read, to write, to present, to organize thoughts and to do scientific thinking. With his help, I have made significant progress in these aspects.

I would also like to acknowledge the members of my dissertation committee, who have continuously supported my work. I thank Professor Eric Sandvol for his insightful suggestions in my research on connecting model results with seismic observations. I thank Professor Robert Bauer, Professor Michael Underwood, and Professor Vellore Gopalaratnam for teaching me the knowledge of structure geology, plate tectonics, and mechanics, which has been the foundation of my research.

My sincere appreciation is extended to Professor Kevin Shelton, Professor Peter Nabelek, Professor Francisco Gomez, Dr. Youqing Yang, Dr. Huai Zhang, Mrs. Linda Garrison, Mrs. Marsha Huckabey, and Mr. Stephen Stanton for their academic,

TABLE OF CONTENTS

LIST OF FIGURES

FAULT EVOLUTION AND EARTHQUAKES: A FINITE ELEMENT STUDY

Qingsong Li

Dr. Mian Liu, Dissertation Supervisor

ABSTRACT

Earthquakes result from sudden fault slip; thus understanding the physics of faulting and fault evolution is important for mitigating earthquake hazards. In this study, I explore stress and strain evolution in faulting and fault evolution and their impacts on earthquakes, using 3D visco-elasto-plastic finite element (FE) models. These models are designed to incorporate the coupling between elasto-frictional upper crust and visco-elastic lower crust and uppermost mantle, and the coupling between fault slip and failure of surrounding upper crust. These couplings are important when studying the stress and strain evolution in a time period of decades to thousands of years long.

The New Madrid Seismic Zone (NMSZ) in central United States is a good example of intraplate seismicity, which cannot be readily explained by the plate tectonics theory and remains poorly understood. I have developed a 3D FE model to simulate stress evolution in the NMSZ and surrounding regions. I find that, following a large earthquake, intraplate seismic zones tend to stay in a Coulomb stress shadow for thousands of years, while significant amount of stress and strain energy relieved from the large earthquakes may migrate to and remain within the surrounding crust. The results are consistent with seismicity in the NMSZ region following the 1811-1812 large events.

To investigate fault evolution and seismicity in plate boundary zone, I have built a 3D dynamic model for the entire San Andreas Fault (SAF) system in California, with the first-order characters of its surface geometry. The results indicate that the geometry of the

SAF may be the primary cause of the observed along-strike variation of slip rate, stress states, and seismicity. In particular, the Big Bend of the SAF causes the scattered seismicity in southern California and may have facilitated the development of the San Jacinto Fault (SJF) and other active faults there. I have explored the dynamic interactions between the SAF and SJF in the model and found that the initiation of the SJF tends to decrease fault slip rate on the southernmost SAF and focus strain energy in the Mojave Desert and along the East California Shear Zone. These results are consistent with the spatial distribution of earthquakes in southern California, and provide some insights into evolution of fault systems in the plate boundary zone as it continuously seeks the optimal way to accommodate the relative plate motion.

Chapter 1   INTRODUCTION

1.1 Earthquakes and Faulting, and Several Unsettled Questions

Earthquakes have posed one of the most important natural hazards in the world. Globally, one M>8 earthquake, a dozen M>7 earthquakes and hundreds of M>6 earthquakes occur each year on average [Lay and Wallace, 1995]. Some of them are shallow earthquakes and close to areas with high population that can cause devastating damage to properties and human lives. Recent devastating earthquakes include 2001 Bhuj, India earthquake (M7.7), which caused >20,000 people death, the 2003 Bam, Iran earthquake (M6.6) with >20,000 people killed, the 2004 Sumatra, Indonesia earthquake (M9.0) with >150,000 people killed, and the 2005 Kashmir, Pakistan earthquake (M7.6) with a death toll > 80,000.

To minimize the possible damages caused by earthquakes, it is important to understand the physics of earthquakes and their relations with fault evolution. To contribute to our understanding of earthquake physics and fault evolution, extensive studies have been conducted to explore earthquake triggering [Freed and Lin, 2001; Gomberg et al., 2003; Hardebeck et al., 1998; King et al., 1994; Marsan, 2003; Zeng, 2001], postseismic deformation [Freed and Buergmann, 2004; Pollitz, 2003; Pollitz and Dixon, 1998], and secular fault slip [Bird and Kong, 1994; Fitzenz and Miller, 2004; Lavier and Buck, 2002; Meade and Hager, 2005; Savage and Lisowski, 1998; Weldon and Sieh, 1985]. However, present knowledge about earthquakes and faulting is still very limited and inadequate for

making accurate tempo-spatial estimations of seismic potentials. For example, the potential of seismic hazard in central eastern United States is under intense debate due to lack of knowledge of the cause of earthquakes there. Even in the well studied California plate boundary zone, seismic potentials on many faults of the San Andreas fault system are still uncertain.

In this study, I explore several unsettled questions about earthquakes and faulting. One is of the difference between stress/strain energy evolution in interplate and intraplate seismic zones. Seismic zones may be categorized into interplate and intraplate seismic zones based on their proximity to plate boundaries. They have significant differences. Compared with interplate seismic zones, intraplate seismic zones have shorter fault zone length, lower deformation rates, lower seismicity rates, larger stress drop in large earthquakes, larger seismic wave attenuation rates, and slower aftershocks decay rates. However, the fundamental causes of these differences are still unclear.

The second question is of the relation between historical large intraplate earthquakes and the present-day seismicity in intraplate seismic zones and surrounding regions. Intraplate seismic zones are generally characterized by both large historical earthquakes and instrumentally recorded seismicity that are above the average level for intraplate regions. Whether or not some of the instrumentally recorded small earthquakes are aftershocks of large historical earthquakes remains unclear. If they are aftershocks, they have little to do with future seismic hazards. Otherwise, they may indicate ongoing loading and thus may lead to future large earthquakes. The idea of aftershocks is challenged by the present seismicity in some intraplate seismic zones that occurs more than 100 years after large historical earthquakes, while normal aftershocks occur within decades after the main

shock. However, the aftershock idea is consistent with many middle-sized earthquakes occurring at tip regions of the fault zone, where historical large earthquakes have caused stress increase.

The third question is of the cause for some large intraplate earthquakes. The seismicity in intraplate regions is sparse. However, large devastating earthquakes do occur in these regions. Whereas it is well known that interplate earthquakes are caused by relative plate motion, the causes of intraplate earthquakes are still enigmatic. One hypothesis is reactivation of ancient weak zones [Johnston, 1996; Johnston and Kanter, 1990]. Others suggest that some intraplate earthquakes may be triggered by isostatic rebound for deglaciation [Grollimund and Zoback, 2001]. Another hypothesis links intraplate earthquakes to some local change of properties or driving forces, such as sudden failure of lower crust [Kenner and Segall, 2000a] or sudden sinking of mafic intrusive bodies [Pollitz et al., 2001a]. Moreover, some intraplate earthquakes are proposed to be caused by diffuse plate boundary processes, such as the 2001 Bhuj, India earthquake [Stein et al., 2002].

The fourth question is of the cause for spatial variation of seismicity and secular fault slip rates in plate boundary zones. Seismicity and fault slip rates may vary significantly along the fault strike. For instance, in California high slip rates and clustered seismicity occur along the straight central San Andreas Fault (SAF), while low slip rates and diffused seismicity occur along the bended southern SAF. Although along-strike variations of seismicity and slip rate may have numerous causes, such as stressing rate [Parsons, 2006] and distribution and properties of active secondary faults [Bird and Kong, 1994], a particularly important cause may be the geometry of main plate boundary faults. Main plate boundary faults account for a large portion of relative plate motions. Secular fault slip

3

on them may have significant impacts on stress and strain evolution in regional crust, especially when the faults have a non-planar geometry [Du and Aydin, 1996; Duan and Oglesby, 2005; Fitzenz and Miller, 2004; Lynch and Richards, 2001].

The fifth question relates to the dynamic interaction between major faults in plate boundary zones in a long time scale. The evolution of neighboring faults may interact with each other, which is especially apparent in plate boundary zones. For example, the slip rate on the southernmost San Andreas Fault (SAF) is codependent with the slip rate on the San Jacinto Fault (SJF) [Bennett et al., 2004]. The cause is not clear. Hypotheses include continuous bending of the SAF, initiation of the SJF, and formation of the transverse ranges. These hypotheses have yet to be vigorously tested. Moreover, it is not clear how the fault interaction is influenced by lithosphere rheology structure, fault properties and distribution, and loading mechanism. These factors are proposed to have effects on fault zone formation and evolution, and secular fault slip rates [Bird and Kong, 1994; Griffith and Cooke, 2005; Lavier and Buck, 2002; Lavier et al., 2000].

1.2 Geodynamic Modeling and Model Constraints

To address the questions outlined above, we need to understand the dynamic interplays of driving sources (relative plate motion and plate interior deformation), fault strength, and lithosphere rheology. One important way to explore these dynamic interplays is through geodynamic modeling, which is to simulate how lithosphere deforms under various driving forces. Geodynamic modeling generally uses numerical modeling methods, such as finite element method, distinct element method, finite difference method, and finite volume method. The typical applications of geodynamic modeling to earthquakes and faulting

include coseismic stress change [King et al., 1994], postseismic stress evolution [Freed and Lin, 2001], secular fault slip [Bird and Kong, 1994], fault formation [Lavier and Buck, 2002].

Geodynamic modeling has to be constrained to give out useful insights of the physics in geological and geophysical phenomena. The more the model is constrained, the more information the model results have to compare with observations. The typical constraints used in modeling studies of earthquakes and faulting include lithosphere rheology structure, ground surface movement, and secular fault slip rate.

Lithospheric rheology has been derived from two distinct approaches. One approach is based on experimental results of mineral properties as function of mineral composition, fluid contents, temperature and pressure in the lithosphere [Ranalli, 1995]. The continental crust generally consists of granitic rocks and the mantle is generally composed of olivine dominated mafic rocks. Given the temperature and pressure variations with depth, the lithosphere typically has a yield envelope like a sandwich with a relatively strong upper crust and uppermost mantle and a weak lower crust. However, latest studies about earthquake depth and dynamics at Moho start to challenge the 'jelly sandwich model' [Houseman and Billen, 2005; Jackson, 2002]. Their results suggest a relatively stronger lower crust and weaker uppermost mantle. The other approach is based on geodetic measurements and geodynamic modeling of ground surface movements following earthquakes and deglaciation [Hager, 1991; Kenner and Segall, 2000b; Pollitz et al., 2001b].

The ground surface movement related with earthquakes may be detected by GPS (Global Positioning System) and InSAR (Interferometric Synthetic Aperture Radar)

methods [Fialko et al., 2001; Pollitz and Dixon, 1998]. The geometry of faults may be inferred from geological and seismological studies. The ruptured fault planes are delineated by the locations of aftershocks following the main earthquake. Fault slip distribution on the fault plane can be inversed from elastic half space dislocation model with detail InSAR surface displacement measurements [Simons et al., 2002].

Two approaches have been used to estimate secular fault slip rates. One is based on geomorphology and trenching studies (geological method). By measuring the off-set of fault zones and determining the time period of shifting, one can calculate the long-term average fault slip rate [Keller et al., 1982]. Trenching study is to detect ancient fault rupture events and their slip distance in trenches. Various dating methods may be used to determine the age of the fault slip events. The slip distance and timing yield fault slip rates [Weldon et al., 2004].

The other approach is based on inverse models and GPS and InSAR surface velocity measurements (geodetic method). The models used in geodetic inversion include elastic dislocation model [Savage and Burford, 1973], viscoelastic coupling model [Savage and Prescott, 1978], viscoelastic cycle model with boundary element approach [Johnson and Segall, 2004], and three dimensional elastic block models [Meade and Hager, 2005]. Each of these models incorporates a series of parameters, including secular fault slip rate. The models predict patterns of surface deformation and stresses, which are compared with observations. By minimizing the misfit between model predictions and observations, inverse modeling finds the best-fitting secular fault slip rates and other model parameters [Becker et al., 2005].

1.3 A New Finite Element Model and its Applications

Previous geodynamic models of earthquakes and faulting generally assume elastic or visco-elastic rheology [Freed and Lin, 2001; Griffith and Cooke, 2005; King et al., 1994; Pollitz et al., 2001b; Smith and Sandwell, 2003]. However, more realistic faulting associated with earthquake cycles involves simultaneous elastic, visco-elastic, and frictional (plastic) deformation. Elastic strain in the upper crust is accumulated in interseismic period and released coseismically. In postseismic period, viscous relaxation of the lower crust and upper mantle cause stress and strain evolution in the lithosphere. Frictional failure occurs in fault rupture and failure of surrounding upper crust.

To simulate simultaneous visco-elasto-plastic deformation in 3D lithospheric model is computationally challenging, that is the main reason limiting previous models to various simplifications. Fortunately, affordable PC clusters have made supercomputing power widely available in recent years.

In this study, I developed a three dimensional parallel visco-elasto-plastic finite element model (details in chapter 2), and successfully applied the model into studying faulting and seismicity in both intraplate and interplate settings. The results are presented in five articles (four published, one in preparation). They are presented as Chapter 3-7 in the following.

1.4 References

Becker, T.W., J.L. Hardebeck, and G. Anderson, Constraints on fault slip rates of the southern California plate boundary from GPS velocity and stress inversions, *Geophys. J. Int.*, *160*, 634-650, 2005.

Bennett, R.A., A.M. Friedrich, and K.P. Furlong, Codependent histories of the San

Andreas and San Jacinto fault zones from inversion of fault displacement rates, *Geology*, *32*, 961-964, 2004.

Bird, P., and X. Kong, Computer simulations of California tectonics confirm very low strength of major faults, *GSA Bull.*, *106* (2), 159-174, 1994.

Du, Y., and A. Aydin, Is the San Andreas big bend responsible for the landers earthquake and the Eastern California shear zone?, *Geology*, *24* (3), 219-222, 1996.

Duan, B., and D.D. Oglesby, Multicycle dynamics of nonplanar strike-slip faults, *J. Geophys. Res.*, *110*, B03304, 2005.

Fialko, Y., M. Simons, and D.C. Agnew, The complete (3-D) surface displacement field in the epicentral area of the 1999 Mw 7.1 Hector Mine earthquake, California, from space geodetic observations, *Geophys. Res. Lett.*, *28* (16), 3063-3066, 2001.

Fitzenz, D.D., and S.A. Miller, New insights on stress rotations from a forward regional model of the San Andreas fault system near its Big Bend in southern California, *J. Geophys. Res.*, *109*, B08404, 2004.

Freed, A.M., and R. Buergmann, Evidence of power-law flow in the Mojave Desert mantle, *Nature*, *430* (6999), 548-551, 2004.

Freed, A.M., and J. Lin, Delayed triggering of the 1999 Hector Mine earthquake by viscoelastic stress transfer, *Nature*, *411* (6834), 180-183, 2001.

Gomberg, J., P. Bodin, and P.A. Reasenberg, Observing earthquakes triggered in the near field by dynamic deformations, *Bull. Seismol. Soc. Am.*, *93* (1), 118-138, 2003.

Griffith, W.A., and M.L. Cooke, How sensitive are fault-slip rates in the Los Angeles basin to tectonic boundary conditions?, *Bull. Seismol. Soc. Am.*, *95* (4), 1263-1275, 2005.

Grollimund, B., and M.D. Zoback, Did deglaciation trigger intraplate seismicity in the New Madrid seismic zone?, *Geology*, *29* (2), 175-178, 2001.

Hager, B.H., Mantle viscosity: A comparison of models from postglacial rebound and from the geoid, plate driving forces, and advected heat flux, in *Glacial Isostacy, Sea Level and Mantle Rheology*, edited by R. Sabadini, K. Lambeck, and E. Boschi, pp. 493-513, Kluwer Academic Publishers, London, 1991.

Hardebeck, J.L., J.J. Nazareth, and E. Hauksson, The static stress change triggering model: constraints from two Southern California aftershock sequences, *J. Geophys. Res.*, *103* (10), 24,427-24,437, 1998.

Houseman, G.A., and M.I. Billen, Is the continental crust stronger or weaker than the mantle lithosphere?, *Eos Trans. AGU*, *86* (52), Fall Meet. Suppl., Abstract

V14A-01, 2005.

Jackson, J.A., Strength of the continental lithosphere: Time to abandon the jelly sandwich?, *GSA Today*, *12* (9), 4-9, 2002.

Johnson, K., and P. Segall, Viscoelastic earthquake cycle models with deep stress-driven creep along the San Andreas fault system, *J. Geophys. Res.*, *109* (B10403), doi:10.1029/2004JB003096, 2004.

Johnston, A.C., Seismic moment assessment of earthquakes in stable continental regions; III, New Madrid 1811-1812, Charleston 1886 and Lisbon 1755, *Geophys. J. Int.*, *126* (2), 314-344, 1996.

Johnston, A.C., and L.R. Kanter, Earthquakes in stable continental crust, *Sci. Am.*, *262(3)*, 68-75, 1990.

Keller, E.A., M.S. Bonkowski, R.J. Korsch, and R.J. Shlemon, Tectonic geomorphology of the San Andreas fault zone in the southern Indio Hills, Coachella Valley, California, *Geol. Soc. Am. Bull.*, *93* (1), 46-56, 1982.

Kenner, S.J., and P. Segall, A mechanical model for intraplate earthquakes; application to the New Madrid seismic zone, *Science*, *289* (5488), 2329-2332, 2000a.

Kenner, S.J., and P. Segall, Postseismic deformation following the 1906 San Francisco earthquake, *J. Geophys. Res.*, *105* (6), 13,195-13,209, 2000b.

King, G.C.P., R.S. Stein, and J. Lin, Static stress changes and the triggering of earthquakes, *Bull. Seismol. Soc. Am.*, *84* (3), 935-953, 1994.

Lavier, L.L., and W.R. Buck, Half graben versus large-offset low-angle normal fault: Importance of keeping cool during normal faulting, *J. Geophys. Res.*, *107* (B6), doi:10.1029/2001JB000513, 2002.

Lavier, L.L., W.R. Buck, and A.B.N. Poliakov, Factors controlling normal fault offset in an ideal brittle layer, *J. Geophys. Res.*, *105*, 23,431-23,442, 2000.

Lay, T., and T.C. Wallace, *Modern Global Seismology*, Academic Press, San Diego, 1995.

Lynch, J.C., and M.A. Richards, Finite element models of stress orientations in well-developed strike-slip fault zones: Implications for the distribution of lower crustal strain, *J. Geophys. Res.*, *106* (B11), 26,707-26,729, 2001.

Marsan, D., Triggering of seismicity at short timescales following California earthquakes, *J. Geophys. Res.*, *108* (B5), doi: 108:10.1029/2002JB001946, 2003.

Meade, B.J., and B.H. Hager, Block models of crustal motion in southern California

constrained by GPS measurements, *J. Geophys. Res.*, *110* (B3), B03403, 2005.

Parsons, T., Tectonic stressing in California modeled from GPS observations, *J. Geophys. Res.*, *111*, doi:10.1029/2005JB003946, 2006.

Pollitz, F.F., The relationship between the instantaneous velocity field and the rate of moment release in the lithosphere, *Geophys. J. Int.*, *153*, 595-608, 2003.

Pollitz, F.F., and T. Dixon, GPS measurements across the northern Caribbean plate boundary zone: impact of postseismic relaxation following historic earthquakes, *Geophys. Res. Lett.*, *25*, 2233-2236, 1998.

Pollitz, F.F., L. Kellogg, and R. Buergmann, Sinking mafic body in a reactivated lower crust; a mechanism for stress concentration at the New Madrid seismic zone, *Bull. Seismol. Soc. Am.*, *91* (6), 1882-1897, 2001a.

Pollitz, F.F., C. Wicks, and W. Thatcher, Mantle flow beneath a continental strike-slip fault; postseismic deformation after the 1999 Hector Mine earthquake, *Science*, *293* (5536), 1814-1818, 2001b.

Ranalli, G., *Rheology of the Earth*, 413 pp., Chapman & Hall, London, 1995.

Savage, J.C., and R. Burford, Geodetic determination of relative plate motion in central California, *J. Geophys. Res.*, *78*, 832-845, 1973.

Savage, J.C., and M. Lisowski, Viscoelastic coupling model of the San Andreas Fault along the big bend, Southern California, *J. Geophys. Res.*, *103* (4), 7281-7292, 1998.

Savage, J.C., and W. Prescott, Asthenosphere readjustment and the earthquake cycle, *J. Geophys. Res.*, *83*, 3369-3376, 1978.

Simons, M., Y. Fialko, and L. Rivera, Coseismic deformation from the 1999 Mw 7.1 Hector Mine, California, earthquake as inferred from InSAR and GPS observations, *Bull. Seismol. Soc. Am.*, *92* (4), 1390-1402, 2002.

Smith, B., and D. Sandwell, Coulomb stress accumulation along the San Andreas Fault system, *Journal of Geophysical Research-Solid Earth*, *108* (B6), 2003.

Stein, S., G.F. Sella, and E.A. Okal, The January 26, 2001, Bhuj earthquake and the diffuse western boundary of the Indian plate, in *Plate Boundary Zone*, edited by S. Stein, and J. Freymueller, pp. this volume, American Geophysical Union, Washington, D.C., 2002.

Weldon, R., K. Scharer, T. Fumal, and G. Biasi, Wrightwood and the earthquake cycle: What a long recurrence record tells us about how faults work, *GSA Today*, *14* (9),

4-10, 2004.

Weldon, R.J., and K.E. Sieh, Holocene rate of slip and tentative recurrence interval for large earthquakes on the San Andreas fault, Cajon Pass, southern California, *Geol. Soc. Am. Bull.*, *96*, 793-812, 1985.

Zeng, Y., viscoelastic stress-triggering of the 1999 Hector Mine earthquake by the 1992 Landers earthquake, *Geophys. Res. Lett.*, *28* (15), 3007-3010, 2001.

Chapter 2   FINITE ELEMENT MODEL

2.1 Model Description

I have developed a 3D model to simulate fault evolution associated with earthquakes. The main features of the model include: (1) a more realistic visco-elasto-plastic rheology for simulating simultaneous elastic deformation, viscous relaxation, and frictional failure of the lithosphere; (2) parallel codes for Beowulf computer clusters and other parallel supercomputers.

The governing equations and computation strategy for finite element modeling of elasto-plastic material can be found in many books, such as Cook et al. [2002]. I have modified the equations to incorporate the visco-elasto-plastic rheology. The governing equations for semi-static deformation of a visco-elasto-plastic lithosphere include equilibrium equations, strain-displacement equations and constitutive equations:

For the Lagrangian-type Cartesian coordinates, the 3-D equilibrium equations are

$$\frac{\partial \sigma_{xx}}{\partial x} + \frac{\partial \sigma_{xy}}{\partial y} + \frac{\partial \sigma_{xz}}{\partial z} + f_x = 0$$

$$\frac{\partial \sigma_{xy}}{\partial x} + \frac{\partial \sigma_{yy}}{\partial y} + \frac{\partial \sigma_{yz}}{\partial z} + f_y = 0$$

$$\frac{\partial \sigma_{xz}}{\partial x} + \frac{\partial \sigma_{yz}}{\partial y} + \frac{\partial \sigma_{zz}}{\partial z} + f_z = 0$$

$$(2\text{-}1)$$

where σ_{ij} $(i,j=x,y,z)$ are components of the stress tensor, f_x, f_y, f_z are components of the body force vector. The strain-displacement equations are

$$\varepsilon_{xx} = \frac{\partial u}{\partial x}$$

$$\varepsilon_{yy} = \frac{\partial v}{\partial y}$$

$$\varepsilon_{zz} = \frac{\partial w}{\partial z}$$

$$\varepsilon_{yz} = \frac{\partial w}{\partial y} + \frac{\partial v}{\partial z}$$

$$\varepsilon_{xz} = \frac{\partial w}{\partial x} + \frac{\partial u}{\partial z}$$

$$\varepsilon_{xy} = \frac{\partial u}{\partial y} + \frac{\partial v}{\partial x} \tag{2-2}$$

where ε_{ij} $(i, j = x, y, z)$ are components of engineering strain or conventional strain,

u, v, w are components of the displacement vector.

The constitutive equations for the visco-elasto-plastic media may be illustrated by a model consisting of a dashpot, a spring and a slider in series (Fig. 2.1).

Figure 2.1 One dimensional illustration of visco-elasto-plastic rheology.

Stain increments include viscous, elastic and plastic components,

$$\{d\varepsilon\} = \{d\varepsilon^v\} + \{d\varepsilon^e\} + \{d\varepsilon^p\} \tag{2-3}$$

where superscripts v, e and p denote viscous, elastic and plastic, respectively. Here

13

$\{\}$ contains all six components of strain increments. Viscous component is associated with stress, and elastic component is associated with stress increments.

$$\{d\varepsilon^v\} = [Q]^{-1}\{\sigma^t\}dt$$
$$\{d\varepsilon^e\} = [D]^{-1}\{d\sigma\}$$

(2-4)

where $\{\sigma^t\}$ are stresses at time t, dt is time increment, $\{d\sigma\}$ is stress increments, $[Q]$ is the viscous material property matrix, $[D]$ is the elastic material property matrix.

$$[Q]^{-1} = \frac{1}{q}\begin{pmatrix} \frac{1}{3} & -\frac{1}{6} & -\frac{1}{6} & 0 & 0 & 0 \\ -\frac{1}{6} & \frac{1}{3} & -\frac{1}{6} & 0 & 0 & 0 \\ -\frac{1}{6} & -\frac{1}{6} & \frac{1}{3} & 0 & 0 & 0 \\ 0 & 0 & 0 & 1 & 0 & 0 \\ 0 & 0 & 0 & 0 & 1 & 0 \\ 0 & 0 & 0 & 0 & 0 & 1 \end{pmatrix}$$

(2-5)

$$[D] = \frac{E}{(1+v)(1-2v)}\begin{pmatrix} 1-v & v & v & 0 & 0 & 0 \\ v & 1-v & v & 0 & 0 & 0 \\ v & v & 1-v & 0 & 0 & 0 \\ 0 & 0 & 0 & 0.5-v & 0 & 0 \\ 0 & 0 & 0 & 0 & 0.5-v & 0 \\ 0 & 0 & 0 & 0 & 0 & 0.5-v \end{pmatrix}$$

(2-6)

where q is viscosity, E is the Young's Modulus, v is the Poisson's Ratio. In order to use backward differentiation formulas, stresses at time t are divided into two parts:

$$\{\sigma^t\} = \{d\sigma\} + \{\sigma^{t-dt}\}$$

(2-7)

From Eqs. 2-3, 2-4 and 2-7, I obtain

$$\{d\sigma\} = [\tilde{D}](\{d\varepsilon\} - \{d\varepsilon^p\}) + \{d\tilde{\sigma}\}$$

(2-8)

where

14

$$[\tilde{D}] = ([D]^{-1} + [Q]^{-1} dt)^{-1}$$

$$\{d\tilde{\sigma}\} = -[\tilde{D}][Q]^{-1} dt \{\sigma^{t-dt}\}$$

(2-9)

The yield function, which only incorporate isotropic hardening here, can be written as

$$F = F(\{\sigma\}, W_p)$$

(2-10)

where W_p is plastic work per unit volume

$$W_p = \int \{\sigma\}^T \{d\varepsilon^p\}$$

(2-11)

Plastic strain direction (the flow rule) is specified with a function G, which is called a "plastic potential". Plastic strain increments are given by

$$\{d\varepsilon^p\} = \{\frac{\partial G}{\partial \sigma}\} d\lambda$$

(2-12)

where $d\lambda$ is a "plastic multiplier". The flow rule is called "associated" if it is derived

from the yield surface ($G = F$) and "non-associated" if a separate flow potential is used.

During an increment of plastic straining, $dF = 0$, then

$$\{\frac{\partial F}{\partial \sigma}\}^T \{d\sigma\} + \frac{\partial F}{\partial W_p} dW_p = 0$$

(2-13)

Substitution of Eq. 2-12 into Eqs. 2-8 and 2-11 provides

$$\{d\sigma\} = [\tilde{D}](\{d\varepsilon\} - \{\frac{\partial G}{\partial \sigma}\} d\lambda) + \{d\tilde{\sigma}\}$$

$$dW_p = \{\sigma\}^T \{\frac{\partial G}{\partial \sigma}\} d\lambda$$

(2-14)

By substituting Eq. 2-14 into Eq. 2-13, I obtain

$$d\lambda = \frac{\{\frac{\partial F}{\partial \sigma}\}^T ([\tilde{D}]\{d\varepsilon\} + \{d\tilde{\sigma}\})}{\{\frac{\partial F}{\partial \sigma}\}^T [\tilde{D}]\{\frac{\partial G}{\partial \sigma}\} - \frac{\partial F}{\partial W_p} \{\sigma\}^T \{\frac{\partial G}{\partial \sigma}\}}$$

(2-15)

15

Finally, from Eqs. 2-14 and 2-15 I obtain

$$\{d\sigma\} = ([\tilde{D}] - [D_p])\{d\varepsilon\} + \{d\tilde{\sigma}\} - \{d\tilde{\sigma}_p\}$$

(2-16)

where

$$[D_p] = \frac{[\tilde{D}]\{\frac{\partial G}{\partial \sigma}\}\{\frac{\partial F}{\partial \sigma}\}^T [\tilde{D}]}{\{\frac{\partial F}{\partial \sigma}\}^T [\tilde{D}]\{\frac{\partial G}{\partial \sigma}\} - \frac{\partial F}{\partial W_p}\{\sigma\}^T \{\frac{\partial G}{\partial \sigma}\}}$$

$$\{d\tilde{\sigma}_p\} = \frac{[\tilde{D}]\{\frac{\partial G}{\partial \sigma}\}\{\frac{\partial F}{\partial \sigma}\}^T \{d\tilde{\sigma}\}}{\{\frac{\partial F}{\partial \sigma}\}^T [\tilde{D}]\{\frac{\partial G}{\partial \sigma}\} - \frac{\partial F}{\partial W_p}\{\sigma\}^T \{\frac{\partial G}{\partial \sigma}\}}$$

(2-17)

2.2 Finite Element Formulation

Finite element method is a method for numerical solution of field problems described by partial differential equations or by an integral expression. It divided the model domain into small pieces (finite elements). In each finite element a field variable is allowed to have only a simple spatial variation, such as linear approximation. Thus the field variable over the entire model domain is approximated element by element. The Galerkin weighted residual method is commonly used for formulating finite elements from partial differential equations and boundary conditions. The partial differential equations are satisfied over model domain in an integral sense rather than at every point.

With the Galerkin method, from equilibrium equation 2-1 I obtain

$$\int_V \left\{ \begin{array}{l} (\frac{\partial \sigma_{xx}^t}{\partial x} + \frac{\partial \sigma_{xy}^t}{\partial y} + \frac{\partial \sigma_{xz}^t}{\partial z} + f_x^t)\delta u + (\frac{\partial \sigma_{xy}^t}{\partial x} + \frac{\partial \sigma_{yy}^t}{\partial y} + \frac{\partial \sigma_{yz}^t}{\partial z} + f_y^t)\delta v \\ + (\frac{\partial \sigma_{xz}^t}{\partial x} + \frac{\partial \sigma_{yz}^t}{\partial y} + \frac{\partial \sigma_{zz}^t}{\partial z} + f_z^t)\delta w \end{array} \right\} dV = 0$$

(2-18)

where V is the whole model domain, superscript t means that the equilibrium exists at

16

time t. By changing Eq. 2-18 to a weak form, I obtain

$$\int_V \sigma_{xx}^t \delta\varepsilon_{xx} + \sigma_{yy}^t \delta\varepsilon_{yy} + \sigma_{zz}^t \delta\varepsilon_{zz} + \sigma_{yz}^t \delta\varepsilon_{yz} + \sigma_{xz}^t \delta\varepsilon_{xz} + \sigma_{xy}^t \delta\varepsilon_{xy} dV =$$
$$\int_V f_x^t \delta u + f_y^t \delta v + f_z^t \delta w dV + \int_\Gamma T_x^t \delta u + T_y^t \delta v + T_z^t \delta w d\Gamma$$

$$(2\text{-}19)$$

where T are boundary forces at boundary Γ. Substitution of Eqs. 2-7 and 2-16 into Eq. 2-19 provides

$$\int_V \{\delta\varepsilon\}^T ([\tilde{D}] - [D_p]) \{d\varepsilon\} dV = \int_V \{\delta\varepsilon\}^T (\{d\tilde{\sigma}_p\} - \{d\tilde{\sigma}\}) dV +$$
$$\int_V \{\delta u\}^T \{f^t\} dV + \int_\Gamma \{\delta u\}^T \{T^t\} d\Gamma - \int_V \{\delta\varepsilon\}^T \{\sigma^{t-dt}\} dV$$

$$(2\text{-}20)$$

When yielding has not appeared (F<0) or unloading has occurred (F=0 and dF<0), $[D_p]$ and $\{d\tilde{\sigma}_p\}$ are set to zero. Element tangent stiffness matrix and load vector are

$$[K_e] = \int_e [B]^T ([\tilde{D}] - [D_p]) [B] dV$$
$$\{dR_e\} = \int_e [B]^T (\{d\tilde{\sigma}_p\} - \{d\tilde{\sigma}\}) dV +$$
$$\int_e [N]^T \{f^t\} dV + \int_e [N]^T \{T^t\} d\Gamma - \int_e [B]^T \{\sigma^{t-dt}\} dV$$

$$(2\text{-}21)$$

where [B] is the displacement-strain matrix, [N] is the shape function.

Assembled equations for a finite element structure are

$$[K]\{dU\} = \{dR\}$$

$$(2\text{-}22)$$

where $\{dU\}$ is the displacement increment from time $t-dt$ to t, $[K]$ is the assembled stiffness matrix, and $\{dR\}$ is the assembled loading vector.

2.3 Computational Procedure

The goal of the FE model is to determine nodal displacements and stresses in a time period with known quasi-static external loads, such as tectonic loading due to continuous relative plate motion. Calculations described in this section are performed at each Gaussian

17

point. Selective reduced integration method [Kavanagh and Key, 1972] is used to prevent dilatational locking.

Here I assume that deformation and stress produced at time $t - dt$ do not violate equilibrium conditions, compatibility conditions, or the yield criterion. Then the following steps are taken to determine displacement and stress at time t after a time increment dt.

1. Stress increments are calculated with displacement increments obtained in the last iteration step (displacement increments are set to zero at the beginning of the first iteration step).

$$\{d\sigma\} = [\tilde{D}]\{d\varepsilon\} + \{d\tilde{\sigma}\} \qquad (2\text{-}23)$$

2. Trial visco-elastic update of stresses is calculated.

$$\{\sigma\}_{trial} = \{\sigma^{t-dt}\} + \{d\sigma\} \qquad (2\text{-}24)$$

3. Yield function is calculated with trial stresses.

$$F_C = F(\{\sigma\}_{trial}, W_p) \qquad (2\text{-}25)$$

4. If $F_C < 0$, then conditions remain visco-elastic, so accept trial stresses as correct $\{\sigma^t\}$, and calculate displacement increments using Eq. 2-22 or 2-20, in which $[D_p]$ and $\{d\tilde{\sigma}_p\}$ are set to zero. Go to step 9.

5. If $F_C > 0$, determine the fraction β of the step that is visco-elastic. Here I solve for β in the nonlinear problem

$$F_C = F(\{\sigma^{t-dt}\} + \beta([\tilde{D}]\{d\varepsilon\} + \{d\tilde{\sigma}\}), W_p) = 0 \qquad (2\text{-}26)$$

6. Estimate stresses $\{\sigma\}_C$ that result from the visco-elastic portion of the increment.

$$\{\sigma\}_C = \{\sigma^{t-dt}\} + \beta([\tilde{D}]\{d\varepsilon\} + \{d\tilde{\sigma}\}) \tag{2-27}$$

7.   Estimate stresses $\{\sigma\}_B$ that include the result from plastic increment.

$$\{\sigma\}_B = \{\sigma\}_C + (1-\beta)([\tilde{D}] - [D_p])\{d\varepsilon\} + (1-\beta)(\{d\tilde{\sigma}\} - \{d\tilde{\sigma}_p\}) \tag{2-28}$$

Where $[D_p]$ and $\{d\tilde{\sigma}_p\}$ are average values of stress state B and C. So $\{\sigma\}_B$ is calculated with iteration method.

8.   Stresses $\{\sigma\}_B$ usually do not satisfy the yield condition. A ratio r is iteratively calculated to return stresses to the yield surface.

$$F(\{\sigma\}_B - r\{\frac{\partial G}{\partial \sigma}\}_B, W_p) = 0 \tag{2-29}$$

Finally the correct stress at time t is

$$\{\sigma^t\} = \{\sigma\}_B - r\{\frac{\partial G}{\partial \sigma}\}_B \tag{2-30}$$

9.   Calculate displacement increments using Eq. 2-22 or 2-20, in which $[D_p]$ and $\{d\tilde{\sigma}_p\}$ are set with stresses at time t. Return to step 1 until convergence is reached.

2.4 Parallel Computation

The parallelization of the finite element code is based on Message Passing Interface (MPI). The parallel code has been successfully run on Beowulf computer clusters and other parallel supercomputers. The procedure of parallel computation includes:

1.   The finite element mesh is divided equally into a number of individual parts with METIS, a set of libraries based on multilevel graph partitioning algorithms [Karypis and Kumar, 1999]. The resulting information is of the elements and

nodes in each part, the mapping to original finite element mesh, and the elements and nodes at boundaries between neighboring parts.

2. The information of elements and nodes are read at the master computation node and then sent to each computation node. (In this code, only master node is allowed to read and write disk).

3. Each computation node makes element matrixes and assembles matrixes for each individual part in parallel.

4. Assembled equations are solved with AZTEC, a massively parallel iterative solver library for solving sparse linear systems [Tuminaro et al., 1999]. In every iterative steps of the solving process, the computation nodes exchange results with each other.

5. Nodal stresses are calculated with nodal displacements at each computation node.

6. Master computation node receives nodal displacements and stresses from all computation nodes. If the nodal displacements of the nonlinear problem haven't converged yet, go back to step 3. Otherwise write nodal displacements and stresses on the disk.

2.5 References

Cook, R.D., D.S. Malkus, M.E. Plesha, and R.J. Witt, *Concepts and Applications of Finite Element Analysis*, John Wiley & Sons, Inc., New York, 2002.

Karypis, G., and V. Kumar, A fast and high quality multilevel scheme for partitioning irregular graphs, *SIAM Journal on Scientific Computing, 20* (1), 359-392, 1999.

Kavanagh, K., and S.W. Key, A note on selective and reduced integration techniques in the finite element method, *Int. J. Numer. Meth. Engrg., 4*, 148-150, 1972.

Tuminaro, R.S., M. Heroux, S.A. Hutchinson, and J.N. Shadid, Official Aztec User's Guide: Version 2.1, 1999.

Chapter 3   THE 01/26/2001 BHUJ, INDIA, EARTHQUAKE: INTRAPLATE OR INTERPLATE?

Qingsong Li, Mian Liu, and Youqing Yang

Abstract. The Mw=7.7 Republic Day (01/26/2001) earthquake near Bhuj in western India killed nearly 20,000 people and destroyed tens of thousands of homes. The cause and the tectonic implication of this earthquake have been the subject of intensive debate. Located ~400 km from the plate boundary, the Bhuj earthquake bears significant similarities with some intraplate earthquakes such as those in the New Madrid seismic zone in central United States. On the other hand, the plate boundary in western India is known to be diffuse, thus the Bhuj earthquake may reflect broad plate boundary deformation. To investigate the cause of the Bhuj earthquake and numerous other historic earthquakes concentrated in this part of the Indian plate, we have developed a viscoelastic finite element model to simulate the stress state within the lithosphere of western India. Our results indicate that the intracontinental thrusting and shearing along the northwestern Indian plate boundary may have caused deviatoric stresses to broadly diffuse into the Indian continent. When the internal rheologic heterogeneities of the Indian plate, such as the inherited mechanical weakening in the Kutch rift basin, is included, the model predicts a broad earthquake-prone zone extending hundreds of kilometers into the interior of the Indian plate that includes the Bhuj earthquake and most historic earthquakes in western India.

3.1 Introduction

The paradigm of plate tectonics predicts concentrations of earthquakes, volcanism, and other tectonic activity within narrowly defined plate boundaries, but no significant deformation within the rigid plates. Thus the infrequent, but often large intraplate earthquakes, such as the three Mw > 7.0 earthquakes that occurred between 1811-1812 in the New Madrid area in central United States [*Johnston and Schweig*, 1996; *Hough et al.*, 2000; *Ellis et al.*, 2001], have been enigmatic, and their rare occurrence has further hampered studies of intraplate earthquakes. Thus the Mw= 7.7 earthquake near Bhuj in western India, which occurred on 1/26/2001, has stimulated considerable interests and debate (Fig. 3.1). This earthquake was one of the most devastating earthquakes in this region, causing > 19,000 fatalities and billions of US dollars of damage [*Bendick et al.*, 2001]. Located ~400 km away from the nominal plate boundary, the Bhuj earthquake shared significant similarities with those in the New Madrid Seismic Zone (NMSZ), such as the extensive liquefaction and the lack of surface ruptures. Some workers regard the Bhuj earthquake as a new example of intraplate earthquakes that may provide a rare chance for understanding intraplate earthquakes in general and the large earthquakes in the NMSZ in particular [*Bendick et al.*, 2001; *Ellis et al.*, 2001]. Others, however, recognize the diffuse plate boundary zone deformation in western India and many other places in the world and suggest that the Bhuj earthquake resulted directly from the plate boundary processes and thus may provide more insight into the dynamics of diffuse plate boundaries than intraplate deformation [*Stein et al.*, 2002]. Thus the debate of whether the Bhuj earthquake was an intraplate or an interplate event is by no means purely semantic; the real focus of this debate is on the tectonic implications of this event.

23
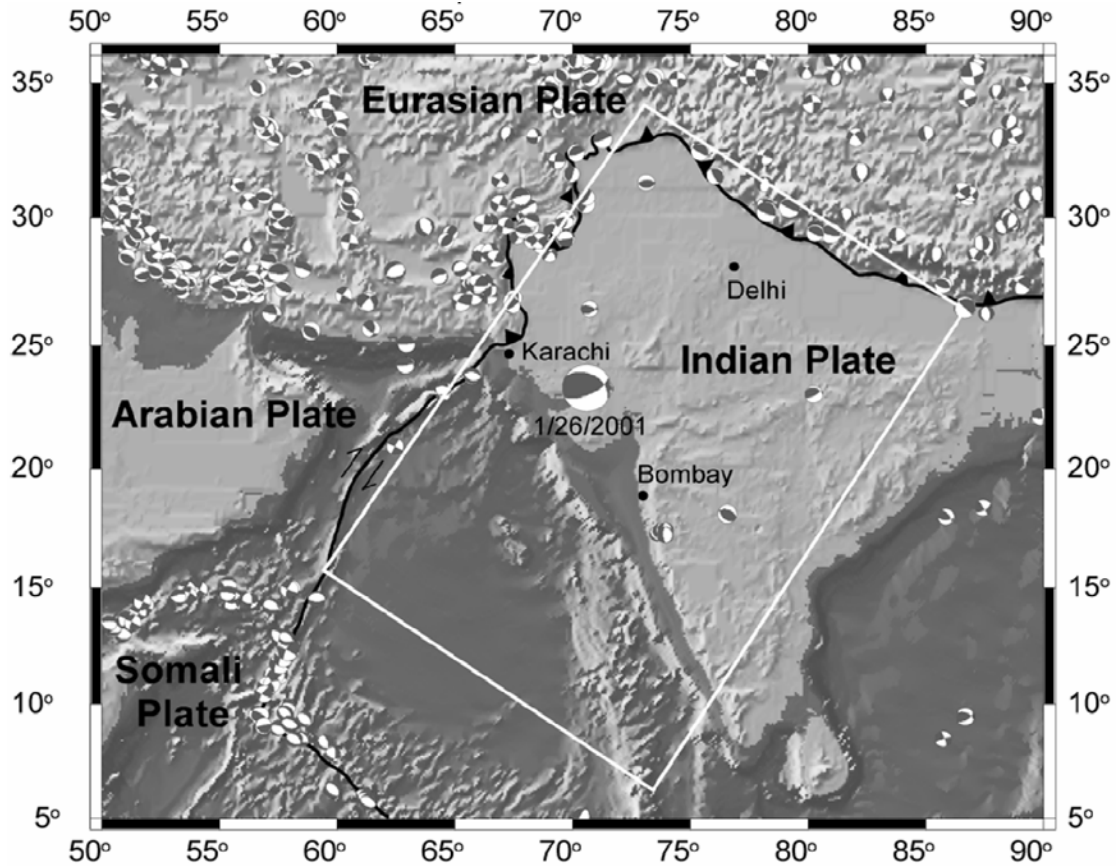
Figure 3.1 Topographic relief and seismicity (Harvard CMT catalog 1976-2001, M≥5) of the Indian Peninsular and the surrounding area. The enlarged fault-plane solution is for the 01/26/2001 Bhuj earthquake [NEIC]. The white rectangle is the model domain.

To get to the heart of this debate, we need to address the question of what caused the Bhuj earthquake. Numerous hints have been provided by geological observations. The Bhuj earthquake occurred in a region of abnormally concentrated seismicities [*Malik et al.*, 1999; *Talwani and Gangopadhyay*, 2001]; the 1819 Rann of Kutch earthquake (Mw=7.5-7.8) that caused considerable casualties and massive property damage occurred only 180 km north of Bhuj. Since 1668 there have been more than 10 major (M> 5) earthquakes in this region [*Malik et al.*, 1999; *Rajendran and Rajendran*, 2001] (Fig. 3.2). Most of these earthquakes, including the Bhuj earthquake, occurred within an ancient rift

complex and on reverse faults with a roughly E-W strike (Fig. 3.2). The nearly N-S principal compressional stresses indicated by these events are consistent with the Indo-Asian plate convergence [*Chung and Gao*, 1995; *Talwani and Gangopadhyay*, 2001]. The specific questions we attempt to address in this work are: 1) why did the Bhuj event and many historic earthquakes concentrate in this part of the Indian plate? 2) were these earthquakes mainly controlled by plate boundary processes or by the rift complex?

We explore the answers to these questions by numerically simulating stress evolution in the lithosphere of western India in a three-dimensional finite element model. Systematic numerical experiments were conducted to evaluate each major factor that may have contributed to the concentration of seismicity in this region. Our results indicate that the intracontinental thrusting along the north-western corner of the Indian plate is the major cause of broad diffusion of deviatoric stresses into the Indian continent. A number of factors, including the contrast in mechanical strength between the oceanic and continental part of the Indian plate and structural weakening of the rift basins, may have contributed to the concentration of seismicity into a broad zone extending hundreds of kilometers into the Indian plate.

3.2 The Bhuj Earthquake and its Tectonic Setting

The Mw=7.7 earthquake occurred in the morning of January 26, 2001, on the Republic Day of India. The epicenter is located at 23.40ºN and 70.32ºE [NEIC: http: //neic.usgs.gov], near Bhuj in the province of Gujarat, India (Fig. 3.2). The official death toll from the India government was close to twenty thousand [*Bendick et al.*, 2001]. Thousands of houses were destroyed and more than half million of people were left homeless. Initial results

indicate a shallow (~20 km) focal depth, with a roughly E-W trending thrust fault plane [NEIC; *Gaur et al.*, 2001]. Based on the aftershock data, the rapture was estimated to have occurred along a plane with a 50-100 km along-strike length and 15-30 km down-dip rapture width. The slip was 1-4 m, reaching ~12 m near the hypocenter [*Antolik and Dreger*, 2001; *Bendick et al.*, 2001]. This event apparently caused few surface scarps [*EERI*, 2001; *Rajendran et al.*, 2001].

The Bhuj earthquake occurred in the Kutch (Kachchh) rift basin, part of a Mesozoic rift complex formed during the break-up of the Gondwana and subsequent northward drift of the Indian plate [*Biswas*, 1982; *Rajendran and Rajendran*, 2001; *Talwani and Gangopadhyay*, 2001] (Fig. 3.2a). It is bounded by the Nagar Parkar fault to the north, the Kathiawar fault to the south, and the nearly north-trending Cambay rift basin to the east. A shallow seismic reflection survey in the Gulf of Kachchh shows an E-W trending offshore basin parallel to the southern boundary of the Kutch rift basin. The basin is filled with sediments ranging in age from Middle Jurassic to recent. Around 65 Ma extensive flood basalts erupted in this part of the Indian plate when it passed over the Deccan/Reunion hotspot [*Courtillot et al.*, 1986], forming the enormous flood basalt province known as the Deccan Traps. The Mesozoic sediments in the Kutch rift basin were intruded and covered by the Deccan basalts [*Biswas*, 1982]. Seismic tomography indicates a pronounced low-velocity structure in the upper mantle under the Kutch region [*Zhou and Murphy*, manuscript in prep.], probably a relic of the thermal perturbation by the mantle plume. Following the Indo-Asian collision ~50 million years ago, the Kutch rift basin, like other parts of the Indian plate, was subjected to north-south compression, resulting in roughly
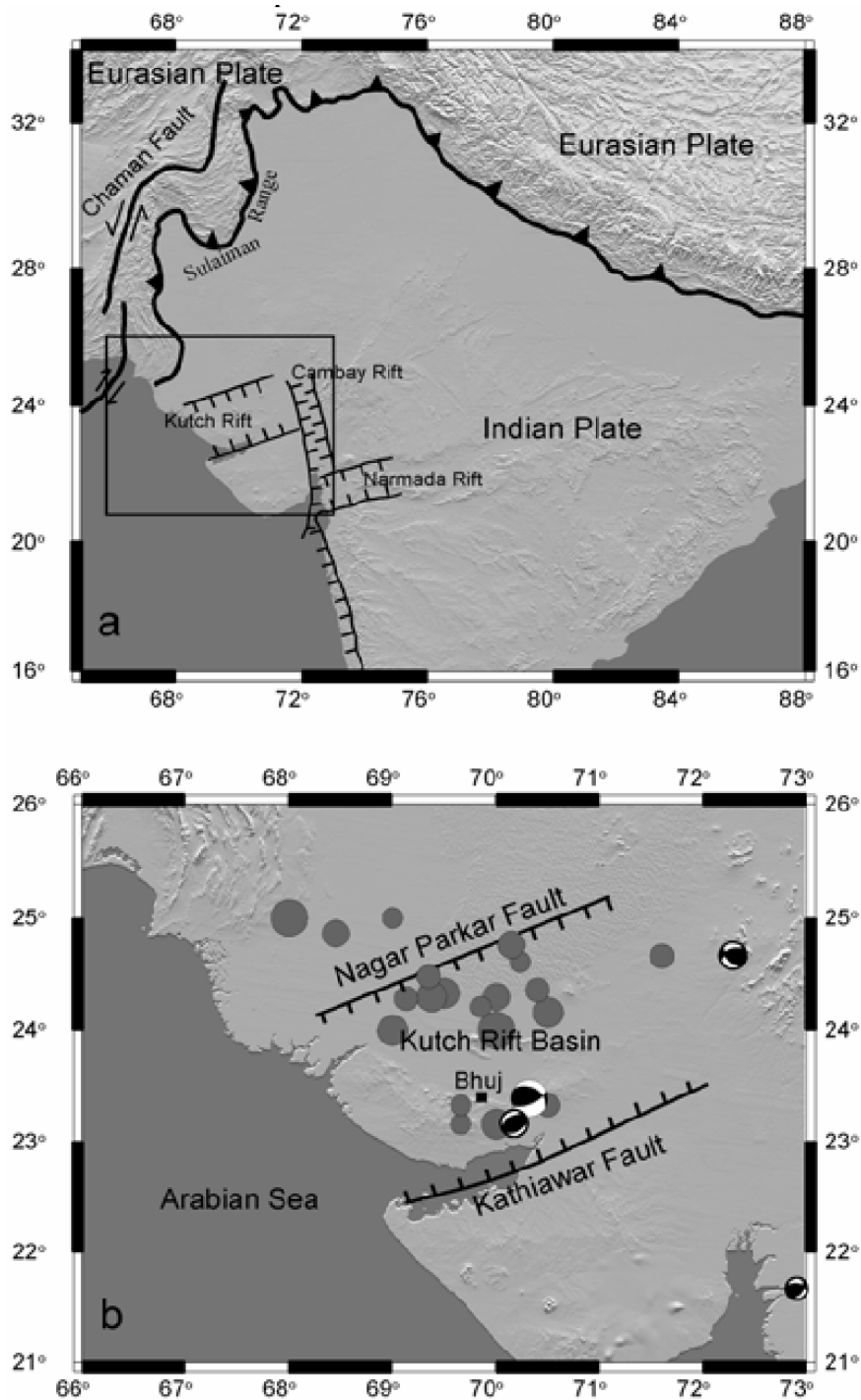
Figure 3.2 (a) Regional topographic relief and simplified structures showing the complex plate boundary of strike-slip shearing and intracontinental thrusting along the northwestern corner of the Indian continent, and the Mesozoic rift complex (after *Biswas [1982]*). The rectangular frame is for (b). (b) Filled circles show the historic seismicity in the Kutch region (data from Malik et al., [1999]). The largest fault-plane solution is the Bhuj earthquake, other fault-plane solutions are from *Chuan and Gao* [1995].

E-W trending fold-thrust structures within the rift basin [*Malik et al.*, 2000; *Rajendran and Rajendran*, 2001]. The rift complex in western India has been the site of numerous large earthquakes [*Malik et al.*, 1999; *Talwani and Gangopadhyay*, 2001]; most of these earthquakes occurred in the Kutch rift basin and surrounding regions (Fig. 3.2b).

3.3 Numerical Model

To investigate why many of the large earthquakes concentrated in the Kutch rift basin and surrounding regions, we developed a three-dimensional finite element model to simulate stress distribution and evolution in western India. Fig. 3.3 shows the model geometry and boundary conditions. The low-relief Indian plate is approximated by a flat viscolastic plate. The rheologic parameters for the basic model include a 2.0×10^{10} Pa Young's modulus, a 0.3 Poison's ratio, and a 1.0×10^{23} Pa s effective viscosity. These are conventional values [*Turcotte and Schubert*, 1982; *Williams and Richardson*, 1991; *Flesch et al.*, 2001], and because our focus here is on stress patterns instead of absolute stress values, our general conclusions are not sensitive to the chosen parameters. In some cases the rheologic difference between continental and oceanic parts of the Indian plate and the rheologic effects of the rift complex are considered. The southern side of the model domain is a velocity boundary, and viscous damping is imposed on the northern side to produce internal shortening within the India continent consistent with the GPS data, which is $2\text{-}7 \times 10^{-9}$ yr^{-1} [*Paul et al.*, 2001]. To be conservative, we used a value of 2×10^{-9} yr^{-1} in the model, whereas using a greater shortening rate will enhance the stress patterns shown below. We used 35 mm yr^{-1} on the southern side of the model based on the GPS measurements of the Indian plate [*Holt et al.*, 2000; *Paul et al.*, 2001; *Sella et al.*, 2002].

However, we produced similar results using 50 mm yr-1 as indicated by the plate motion models [*DeMets et al.*, 1990; *DeMets et al.*, 1994]. This is because that, in either case, the viscose damping on the northern side of the model was adjusted to produce the same shortening rate within the model Indian plate, which is constrained by the GPS data. The right side is in the middle of the Indian plate and can be viewed as a symmetric boundary; we used viscous damping elements to resist motion normal to this boundary. The left side represents the western boundary of the Indian plate, which changes from strike-slip between the Indian and Arabian plates to a complex of strike-slip motion and intracontinental thrusting north of the poorly defined triple junction (Fig. 3.1). Considerable thrusting and crustal shortening along the festoon-shaped Sulaiman range and other ranges are reflected in high seismicity in this region, and 5-14 mm yr-1 of N-S motion between India-Eurasia is accommodated here by intracontinental thrusting [*Bernard et al.*, 2000]. We used additional viscous damping to simulate resistance to the northward motion of the Indian plate along this boundary (Fig. 3.3) and will show that this boundary is important for deviatoric stresses to diffuse into the Indian plate.

Deviatoric stresses within the model Indian plate result from the northward motion imposed on the southern side and resistance on the northern and northwestern sides of the model domain. Flexural stresses due to loading of the Himalayas and stresses acting on the base of the plate arising from the asthenosphere are not included. The distribution and evolution of the deviatoric stresses are obtained by solving the force balance equation:

$$\partial \tau_{ij} / \partial x_j + F_i = 0 \qquad\qquad (3\text{-}1)$$

using the finite element method. Here τ_{ij} is the stress tensor, F_i is the body force, and $i,j=1,2,3$. In this model no topographic loading is assumed because of the low relief of the

Indian plate, and lithostatic body force is removed when calculating the deviatoric stresses [*Liu et al.*, 2000a]. We build the numerical model using the commercial finite element package FEPG (www.fegensoft.com/English/index.htm).
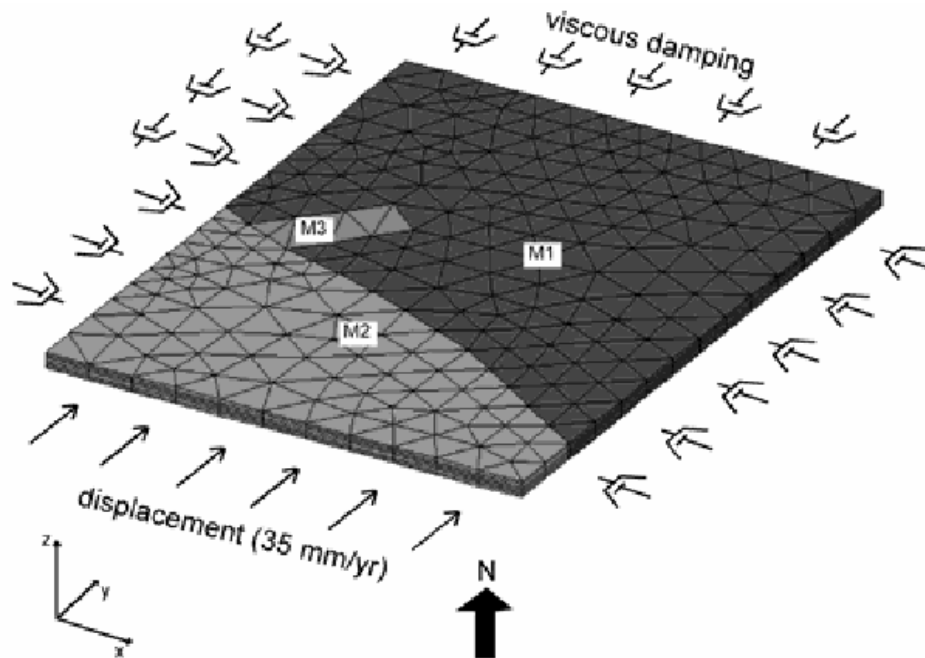
Figure 3.3 Finite element mesh and boundary conditions of the numerical model. M1, M2, M3 are model domains for the continental part of the Indian plate, oceanic part of the Indian plate, and the Kutch rift basin, respectively. See text for discussions.

3.4 Model Results

Systematic numerical experiments were conducted to evaluate the effects of boundary conditions and major factors that may have contributed to the concentration of deviatoric stresses in the Kutch region. Fig. 3.4 shows the predicted pattern of the principal compressional stress ($\sigma 1$). As expected, $\sigma 1$ is horizontal and nearly parallel to the direction of plate convergence. The slightly westward rotation in the northwestern part of the Indian

plate was caused by the resistive boundary condition in the model simulating the effects of intracontinental thrusting along this part of the Indian plate boundary (Fig. 3.3). The rotation would be larger if the resistance was greater; however, the resistance used here is the same as that along the northern side of the model – the Himalayan front, where the value is constrained by the GPS-measured strain rate within the Indian plate and is likely greater than the resistance along the northwestern plate boundary. The general pattern of $\sigma 1$ remained similar when other reasonable boundary conditions and model rheology were used, so the results will not be discussed below. The stress pattern in Fig. 3.4 is consistent
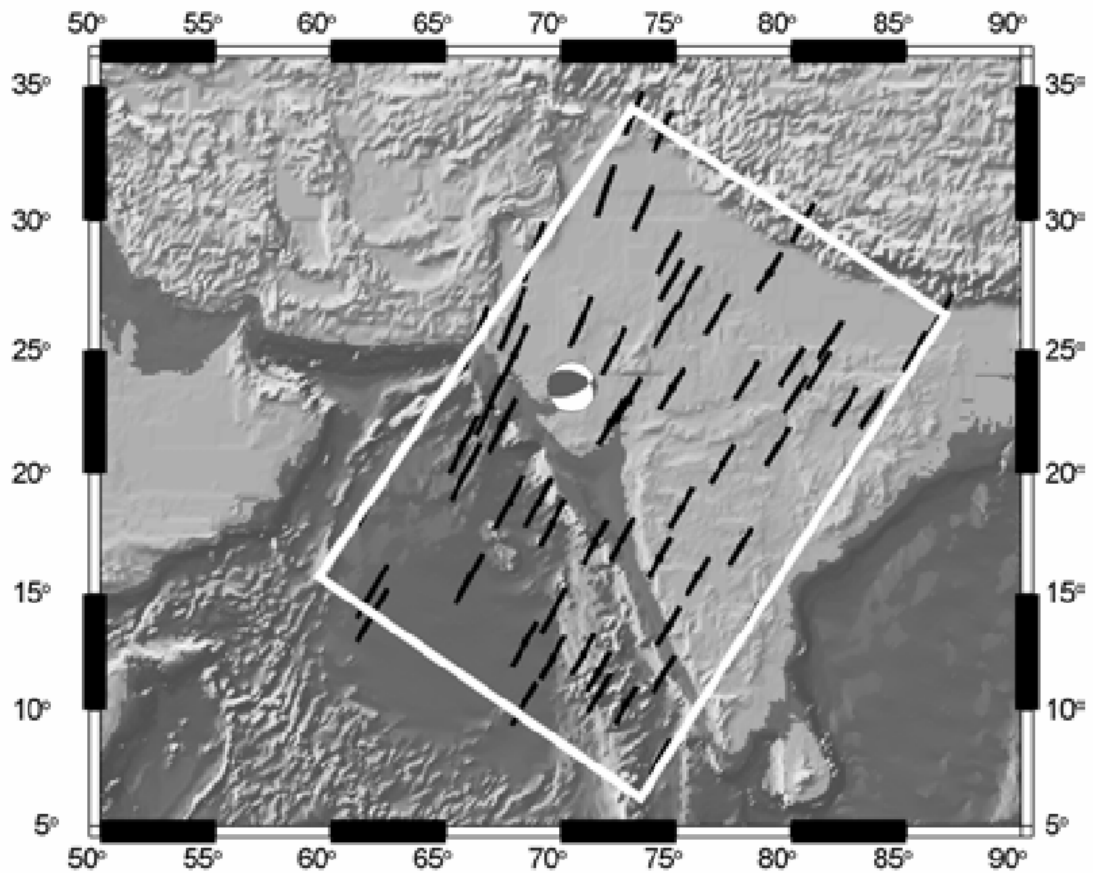
Figure 3.4 Predicted principal compressional stress ($\sigma 1$) within the crust at 20 km depth. The fault-plane solution is for the Bhuj earthquake.

with Late Miocene-present structures and the focal mechanisms of earthquakes in the Kutch region that indicate predominant N-S compression (Fig. 3.2).

Fig. 3.5a shows the predicted surface velocity and deviatoric stresses within the upper crust. The intracontinental thrusting along the northwestern boundary of the Indian plate slows the plate motion near it, distorting the velocity field. The results are analogous to those of a moving glacier slowed near its margins by friction. The deviatoric stresses, which would be uniformly distributed at a given depth without the resistive northwestern boundary, diffuse into the Indian plate with the maximum centered near the triple junction (Fig. 3.5b).

The results in Fig. 3.5a may be regarded as an instantaneous velocity field, because displacement associated with earthquakes was not considered. In nature, the deviatoric stress would be released by earthquakes or aseismic slip when its value is greater than the yield strength of the lithosphere. We simulated such processes in the model by capping the deviatoric stresses below the lithospheric strength. Whenever the deviatoric stress grows beyond the lithospheric strength at a point in the model, a small, instantaneous displacement is added to dissipate the strain energy during a time-step, effectively simulating a seismic (or aseismic) slip. This process is repeated until the deviatoric stress at this point drops below the yield strength at the same point. The resulting velocity field is shown in Fig. 3.6a. Calculated over a period of a few thousand years with many cycles of stress accumulation and release, these results represent the averaged velocity field. Whereas the general pattern is similar to that in Fig. 3.5a, a high velocity gradient is localized near the plate boundary just north of the triple junction. The cumulative seismic slips lead to increased average velocity near the western coastal area while reducing the

velocity north of it, roughly at the location of the Sulaiman range (see Fig. 3.2a). This velocity pattern indicates concentrated crustal contraction near the Sulaiman range, consistent with observations there [*Bernard et al.*, 2000] (Figs. 1-2). The resulting deviatoric stresses are shown in Fig. 3.6b. Comparison with Fig. 3.5b shows that diffusion of deviatoric stresses is further inland. In other words, the high seismicity near western Indian plate boundary facilitates inland diffusion of deviatoric stresses. The physical process may be analogous to earthquake-triggered stress migration along strike-slip faults [*Stein*, 1999].

The strength envelope of the model for the western Indian plate is shown in Fig. 3.7a. We calculated the yield strength assuming a 40-km thick granitic crust and a geotherm characterized by a steady-state surface heat flux of 60 mW m^{-2} [*Pollack et al.*, 1993]. Given the paucity of heat flow data and the uncertainty of lithospheric structure in this region, this strength envelope is used only as a general guide for vertical stress distributions. The predicted vertical distribution of the deviatoric stresses is shown in Fig. 3.7b in an E-W section. The stresses are concentrated near the plate boundary (left side) but diffuse broadly into the plate interior. The high stresses are in the competent layers: the upper-middle crust and the uppermost mantle. To better delineate seismic zones we define an index parameter called fault intensity: fault intensity = deviatoric stress / lithospheric yield strength. Given the uncertainty of lithospheric strength and physical mechanisms controlling earthquakes, the fault intensity provides a useful indication of the likelihood of having earthquakes in a given region.   Using the fault intensity, we re-plot the results of Fig. 3.5 and 3.6 in Fig. 3.8a and 3.8b, respectively. The results show a diffuse seismic zone extending hundreds of kilometers into the Indian plate, enhanced by high seismicity near the western Indian plate

boundary.
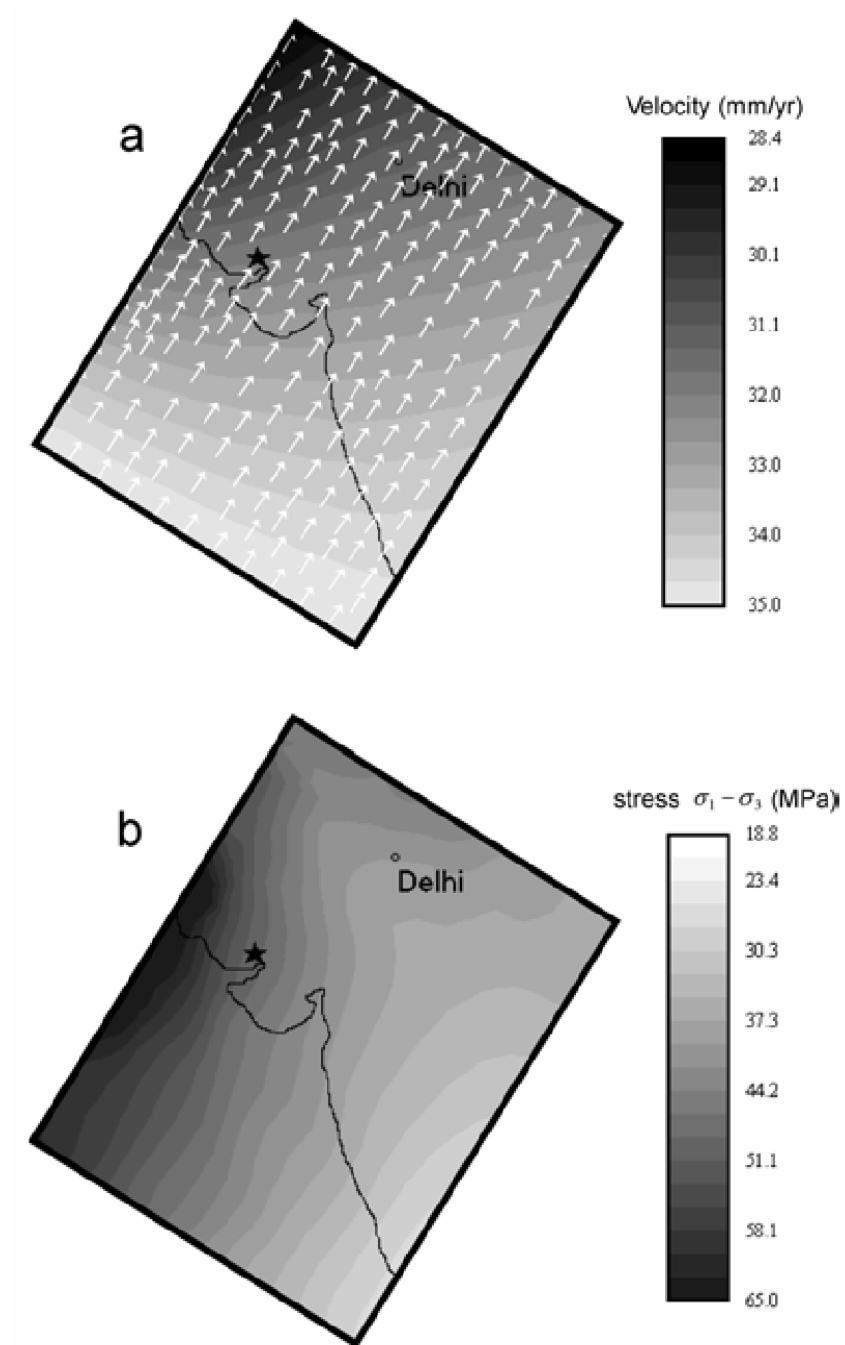
Figure 3.5 (a) Arrows are the predicted surface velocity. The gray background shows the northward velocity contour. The black line indicates the coastline, and the star marks the epicenter of the Bhuj earthquake. (b) The resulting shear stress ($\sigma 1 - \sigma 3$) contour in the crust (at 20 km depth).
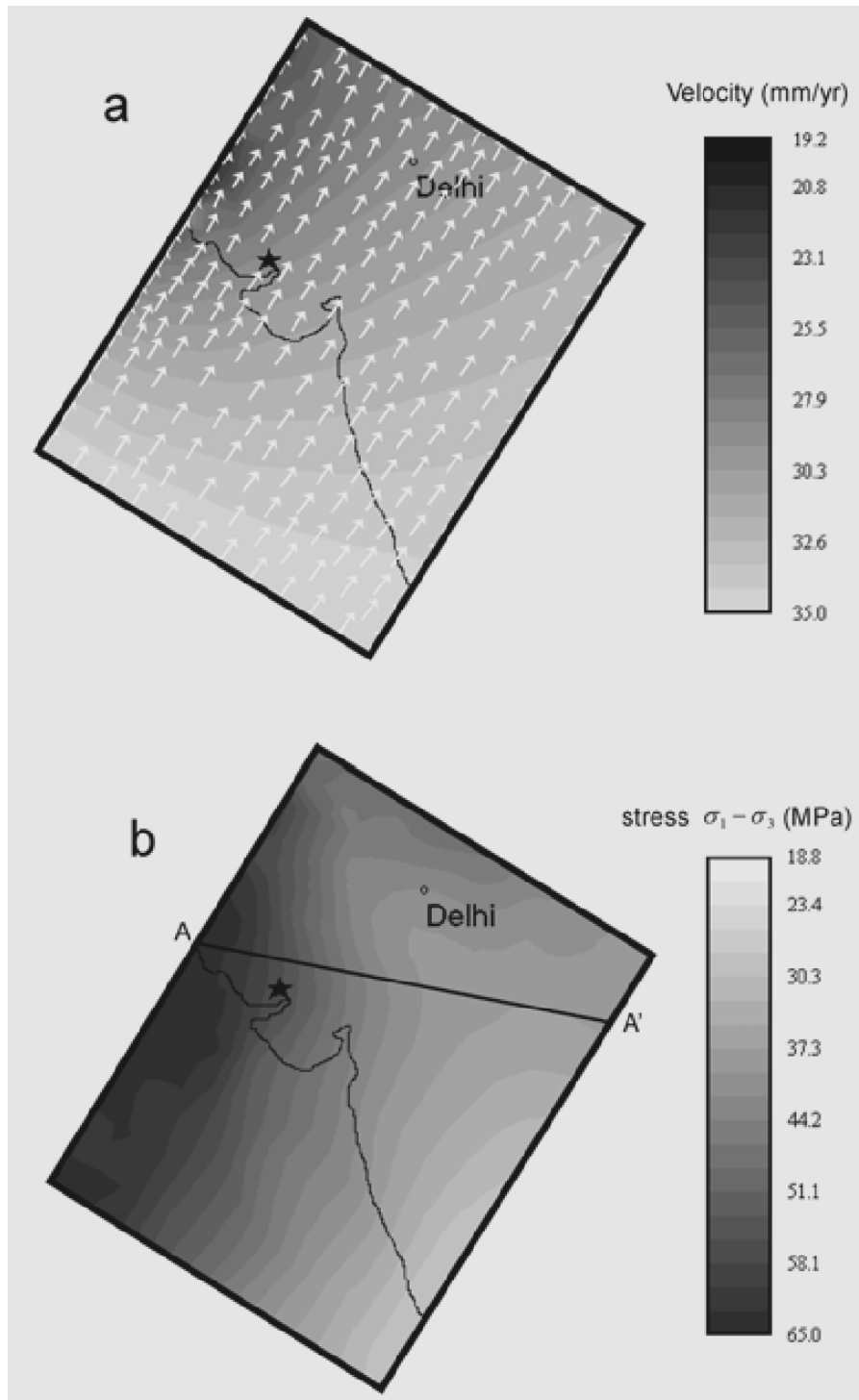
Figure 3.6 (a) Predicted northward surface velocity similar to Fig. 3.5a, but in this case incremental strain (slip) was added to release the shear stress when it is greater than the yield strength of the lithosphere. Other symbols are the same as in Fig. 3.5. (b) The resulting shear stress ($\sigma 1$-$\sigma 3$) in the crust (at 20 km depth). The line A-A' indicates the location of the vertical section in Fig. 3.7b.

Although we have shown that intracontinental thrusting along the northwestern Indian plate boundary can cause broad diffusion of deviatoric stresses into the Indian plate, the patterns shown in Figs. 8 a-b do not resemble the distribution of seismicity in the Kutch region (Fig. 3.2b). One possible reason is the simplified plate boundary geometry used in the model. As shown in Fig. 3.2a, the thrust zone along the northwestern Indian plate boundary is very irregular. This is true especially for the extruding Sulaiman lobe and range, which accommodate 5-14 mm yr-1 N-S plate convergence between the Indian and Eurasian plates [*Bernard et al.*, 2000]. Using more realistic plate boundary geometries may predict more concentrated stresses in front of the Sulaiman range. Another reason may be the contrast between oceanic and continental lithospheric strength. It is well known that the oceanic lithosphere is generally much stronger than continental lithosphere [*Kirby and Kronenberg*, 1987; *Lynch and Morgan*, 1987]. Fig. 3.8c shows the results when we assume the oceanic part of the Indian plate is 10 MPa stronger than the continental part of the Indian plate. Such a rheologic contrast causes further inland diffusion of seismicity, and the predicted seismic zone is now more defined around the Kutch rift basin and surrounding regions. A better-defined seismic zone can be obtained if we assume the crust under the Kutch rift basin has been structurally weakened (Fig. 3.8d). In this case we predicted a distinctive seismic zone extending hundreds of kilometers into the Indian continent that is centered on the Kutch rift basin and includes most of the historic earthquakes in western India.

The 10 MPa structural weakening of the Kutch rift basin used in Fig. 3.8d is arbitrary. There are no reliable constraints on the extent of crustal weakening in the rift complex. One may argue that, with sufficient structural weakening of the Kutch rift basin, a seismic zone
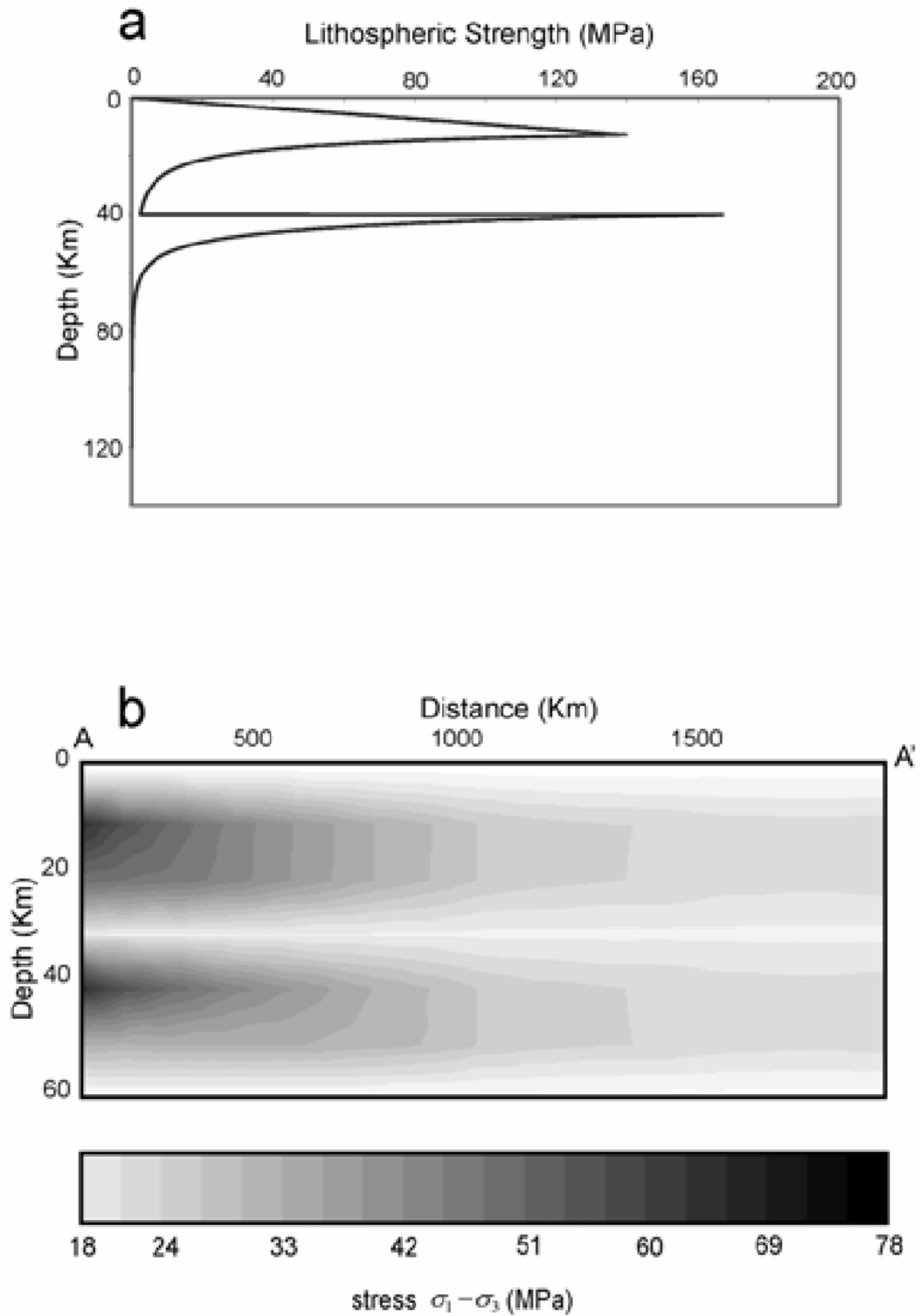
Figure 3.7 (a) The strength envelope of the model lithosphere of western India. (b) Vertical distribution of the deviatoric stress along the A-A' profile in Fig. 3.6b.
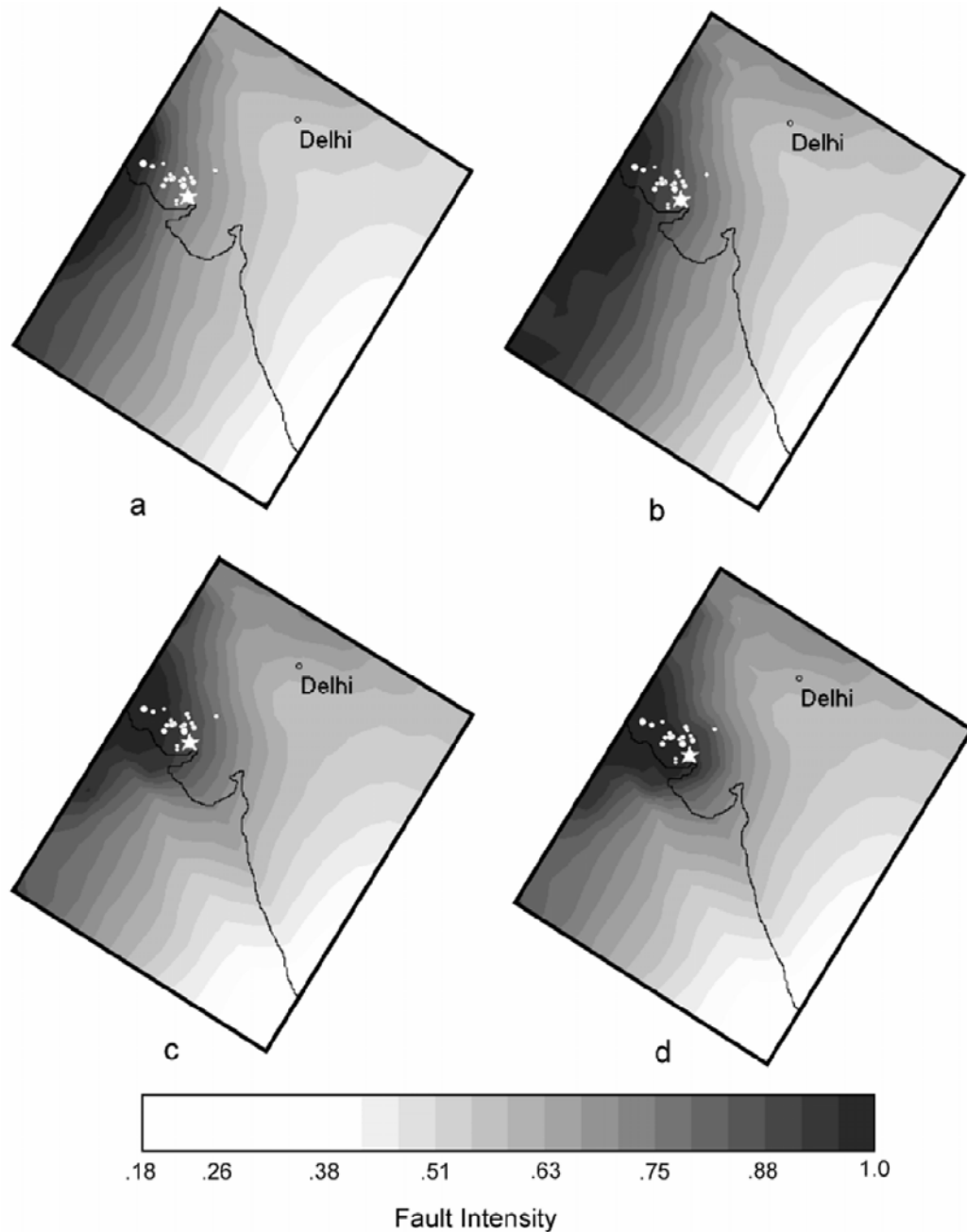
Figure 3.8 Predicted fault intensity in the crust (at 20 km depth). The black line indicates the coastline, the star shows the Bhuj earthquake, and the white dots mark the epicenters of the historic earthquakes in the Kutch region (from Malik et al., [1999]). (a) Fault intensity for the basic case (Fig. 3.5). (b) Fault intensity similar to those in (a), but stress release by earthquakes or aseismic slip is considered (Fig. 3.6). (c) Fault intensity similar to those in (b), but also assuming that the oceanic part of the Indian plate is stronger than the continental part of the Indian plate. (d) Fault intensity similar to those in (c), but also assuming the Kutch rift basin to be a weak zone.

similar to that in Fig. 3.8d can be predicted without requiring changes in plate boundary conditions along the western side of the Indian plate and/or rheologic contrast between the continental and oceanic Indian plate. However, we suggest that mechanical weakening in the rift system is unlikely the dominant cause of the concentrated seismicity in western India. Although a few moderate earthquakes indeed occurred in the Cambay and the Narmada rifts [*Chung*, 1993; *Chung and Gao*, 1995], suggesting that structural weakening of the rifts may be a factor triggering earthquakes, structural weakening alone cannot explain why most of the large earthquakes are concentrated in the Kutch rift basin, which should have the similar amount of structural weakening as the other rifts in western Indian because of their similar origin and evolution history.

We also ran a case with a thinner and weaker mantle lithosphere under the Kutch rift basin as suggested by seismic tomography [*Zhou and Murphy*, manuscript in prep.] and found its contribution to the Kutch seismic zone is likely minor, because most deviatoric stresses can be supported by the strong upper-middle crust.

3.5 Interplate vs. Intraplate Processes

We have shown that the Bhuj earthquake and many historic earthquakes in the Kutch region may have resulted from interactions between the diffuse plate boundary processes and the mechanical heterogeneity within the Indian plate. Intracontinental thrusting along the northwestern Indian plate boundary impedes the northward motion of the Indian plate relative to stable Eurasia, distorting the velocity field and causing deviatoric stresses to diffuse over a broad zone into the Indian plate. High seismicity near the western boundary of the Indian plate limits the deviatoric stresses that can be supported by the lithosphere

near the plate boundary, thus leading to further inland diffusion of deviatoric stresses. On the other hand, mechanical heterogeneity within the Indian plate, mainly the contrasting mechanical strength between the continental and oceanic parts of the Indian plate and the inherited mechanical weakening of the Kutch rift basin, causes seismicity to concentrate in the Kutch rift basin and surrounding regions.

The predictions of this study may be testable. In our model the major cause of broad inland-diffusion of deviatoric stresses is the impeding intracontinental thrusting zone along the Sulaiman range and other ranges in the northwestern part of the Indian plate boundary. This plate boundary process would cause an E-W velocity gradient for the motion of the Indian plate (Fig. 3.5a). Within the Sulaiman Range and the neighboring region such a velocity gradient is suggested by the crustal strain rates inferred from seismicity [*Bernard et al.*, 2000]. Kinematic data away from the plate boundary in this region are lacking. Fig. 3.5a predicts up to 4-5 mm yr^{-1} short-term velocity difference between Delhi and areas near the Sulaiman Range, and Fig. 3.6a indicates a greater long-term velocity difference. This could be tested by future geodetic measurements.

Our results suggest that the Bhuj event and the historic earthquakes in this region cannot be adequately described by any narrowly defined "interplate" or "intraplate" earthquakes. Whereas its epicenter is located ~400 km away from the nominal plate boundary and shares some common characteristics with other intraplate earthquakes like those in the NMSZ [*Bendick et al.*, 2001; *Ellis et al.*, 2001], there is a fundamental difference: the Bhuj event and other historic earthquakes in the Kutch region were strongly influenced by the plate boundary processes. The same cannot be said for the 1811-1812 New Madrid earthquakes, which were located nearly 2000 km from plate boundaries and

showed no clear link to plate boundary processes [*Stein et al.*, this volume]. On the other hand, the diffuse plate boundary deformation reflected by earthquakes in the Kutch region is significantly different from that on the northern side of the Indo-Asian plate boundary, where the weak Asian plate caused broadly diffusing seismicity and crustal deformation. Because of the high rigidity of the Indian plate [*Paul et al.*, 2001; *Yang and Liu*, 2002], the diffuse plate boundary deformation here is strongly controlled by intraplate rheologic heterogeneities.

With the continued refinement of relative motion of the Earth's crust, the definition of a plate boundary has become increasingly blurred [*Gordon and Stein*, 1992; *Gordon*, 1998]. Although many oceanic plate boundaries indeed appear to be well defined, other plate boundaries, especially those in continents, are characterized by diffuse deformation that may extend thousands of kilometers into the plate interior, such as in the Himalayan-Tibetan plateau and western United States. Attempts to understand the diffuse plate boundary deformation have propelled geoscience to advance from the kinematic plate tectonics approximation towards a more comprehensive understanding of the Earth's dynamic system [*Molnar*, 1988]. We now understand that tectonic plates are essentially the top thermal boundary layer of the Earth's convection system powered by heat transfer from the Earth's interior [*Parsons and McKenzie*, 1978]. The tectonic plates behave as rigid plates because they are cold and therefore hard. However, rigid-plate definitions are only an approximation of the lithospheric rheology, which is timescale dependant and spatially heterogeneous [*Ranalli*, 1995; *Liu et al.*, 2000b]. The internal rheologic heterogeneity, either inherited from previous tectonic history or resulting from differential thermal perturbations and tectonic stresses, can cause significant differential motion within the

plates. Within the relatively rigid oceanic plates the internal rheologic change usually

occurs over narrow zones, sometimes causing a rigid block to move at a significantly

different rate from the rest of the plate, or in other words, to behave as "microplates"

[*Engeln and Stein*, 1988]. Similar rheology-controlled differential motion is also common

within continental plates, for instance the rigid Tarim block has experienced considerably

differential motion with respect to the surrounding Asian continent [*Avouac et al.*, 1993;

Neil and Houseman, 1997]. However, in continents the lateral change of lithospheric

rheology is usually more gradual, so the boundary of microplates is less well defined. The

Indian plate is an exceptionally rigid plate with an overall rigidity similar to typical oceanic

plates [*Yang and Liu*, 2002]. If part of the Indian plate breaks up, a distinct microplate may

result. *Stein et al.* [this volume] suggest that such a microplate is forming around the Kutch

Peninsula, and the Bhuj earthquake may be part of the breaking-up process. However, the

present kinematic data are insufficient to verify this hypothesis. Our results suggest that the

diffuse deviatoric stresses associated with plate boundary processes, in conjunction with

the rheologic heterogeneity within the Indian plate, caused the Bhuj earthquake and other

historic seismicity to concentrate in the Kutch region. Further studies of the Bhuj

earthquake may lead to a better understanding of why earthquakes occur within stable

plates and how diffuse plate boundary processes may interact with rheologic heterogeneity

of tectonic plates.

3.6 Acknowledgments

3.7 References

Antolik, M., and D.S. Dreger, Source rapture process of the 26 January, 2001 Bhuj, India, earthquake (M 7.6), *Eos, Transactions, AGU*, *82*, F941, 2001.

Avouac, J.P., P. Tapponnier, M. Bai, H. You, and G. Wang, Active thrusting and folding along the northern Tien Shan and late Cenozoic   rotation of the Tarim relative to Dzungaria and Kazakhstan, *J. Geophys. Res.*, *98*, 6755-6804, 1993.

Bendick, R., R. Bilham, E. Fielding, V.K. Gaur, S.E. Hough, G. Kier, M.N. Kulkarni, S. Martin, K. Mueller, and M. Mukul, The 26 January 2001 "Republic Day" earthquake, India, *Seism. Res.   Lett., 72*, 328-335, 2001.

Bernard, M., T.B. Shen, W.E. Holt, and D.M. Davis, Kinematics of active deformation in the Sulaiman Lobe and Range, Pakistan, *J. Geophys. Res.*, *105*, 13,253-13,279, 2000.

Biswas, S.K., Rift basins in western margin of India and their hydrocarbon prospects with special reference to Kutch Basin, *AAPG Bulletin*, *66*, 1497-1513, 1982.

Chung, W.Y., Source parameters of two rift-associated intraplate earthquakes in peninsular India; the Bhadrachalam earthquake of April 13, 1969 and the Broach earthquake of March 23, 1970, *Tectonophysics*, *225*, 219-230, 1993.

Chung, W.Y., and H. Gao, Source parameters of the Anjar earthquake of July 21, 1956, India, and its seismotectonic implications for the Kutch rift basin, *Tectonophysics*, *242*, 281-292, 1995.

Courtillot, V., J. Besse, D. Vandamme, R. Montigny, J.J. Jaeger, and H. Cappetta, Deccan flood basalts at the Cretaceous/ Tertiary boundary?, *Earth Planet. Sci. Lett., 80*, 361-374, 1986.

DeMets, C., R.G. Gordon, D.F. Argus, and S. Stein, Current plate motions, *Int. J. Geophys.*, *101*, 425-478, 1990.

DeMets, C., R.G. Gordon, D.F. Argus, and S. Stein, Effect of recent revisions to the

geomagnetic reversal time scale on estimates of current plate motion, *Geophys. Res. Lett.*, *21*, 2191-2194, 1994.

EERI, Preliminary observations on the origin and effects of the January 26, 2001 Bhuj (Gujarat, India) earthquake, special report, Earthqu. Engin. Res. Inst., 2001.

Ellis, M., J. Gomberg, and E. Schweig, Indian earthquake may serve as analog for New Madrid earthquakes, *Eos, Transactions, AGU*, *82*, 345, 350, 2001.

Engeln, J., and S. Stein, Microplate and shear zone models for oceanic spreading center reorganization, *J. Geophys. Res.*, *93*, 2839-2856, 1988.

Flesch, L.M., A.J. Haines, and W.E. Holt, Dynamics of the India-Eurasia collision zone, *J. Geophys. Res.*, *106*, 16435-16460, 2001.

Gaur, V.K., A. Magi, K. Priestly, S.S. Rai, and S. Davuluri, Source parameters of the Bhuj mainshock and larger aftershocks from modeling   of broadband teleseismic and regional waveform data, *Eos, Transactions, AGU*, *82*, F941, 2001.

Gordon, R.G., The plate tectonic approximation: plate non-rigidity, diffuse pate boundaries, and global reconstructions, *Ann. Rev. Earth Planet. Sci.*, *26*, 615-642, 1998.

Gordon, R.G., and S. Stein, Global tectonics and space geodesy, *Science, 256*, 333-342, 1992.

Holt, W.E., R.N. Chamot, P.X. Le, A.J. Haines, T.B. Shen, and J. Ren, Velocity field in Asia inferred from Quaternary fault slip rates and Global Positioning System observations, *J. Geophys. Res.*, *105*, 19,185-19,209, 2000.

Hough, S.E., J.G. Armbruster, L. Seeber, and J.F. Hough, On the modified Mercalli intensities and magnitudes of the 1811-1812 New Madrid earthquakes, *J. Geophys. Res.*, *105*, 23,839-23,864, 2000.

Johnston, A.C., and E.S. Schweig, The enigma of the New Madrid earthquakes of 1811-1812, *Ann. Rev.   Earth Planet. Sci.*, 1996.

Kirby, S.H., and A.K. Kronenberg, Rheology of the lithosphere: Selected topics, *Rev. Geophys.*, *25*, 1,219-1,244, 1987.

Liu, M., Y. Shen, and Y. Yang, Gravitational collapse of orogenic crust: A preliminary three-dimensional finite element study, *J. Geophys. Res.*, *105*, 3159-3173, 2000a.

Liu, M., Y. Yang, S. Stein, Y. Zhu, and J. Engeln, Crustal shortening in the Andes: Why do GPS rates differ from geological rates?, *Geophys. Res. Lett.*, *27*, 3005-3008, 2000b.

Lynch, H.D., and P. Morgan, The tensile strength of the lithosphere and the localization of

extension, in *Continental Extensional Tectonics*, edited by M.P. Coward, J.F. Dewey, and P.L. Hancock, pp. 53-66, Geol. Soc. spec. pub., 1987.

Malik, J.N., P.S. Sohoni, S.S. Merh, and R.V. Karanth, Palaeoseismology and neotectonism of Kachchh, western India, in *Active Fault Research for the New Millennium*, edited by K. Okumura, K.H. Goto, and K. Takada, pp. 251-259, Proceedings of the Hokudan International Symposium and School on Active Faulting, 2000.

Malik, J.N., P.S. Sohoni, S.S. Merh, and K. R.V., Modern and historic seismicity of Kachchh, western India, *J. Geol. Soc. India*, *54*, 545-550, 1999.

Molnar, P., Continental tectonics in the aftermath of plate tectonics, *Nature*, *335*, 131-137, 1988.

Neil, E., and G. Houseman, geodynamics of the Tarim Basin and the Tian Shan in central Asia, *Tectonics*, *16*, 571-584, 1997.

Parsons, B., and D.P. McKenzie, Mantle convection and the thermal structure of the plates, *J. Geophys. Res.*, *83*, 4495-4496, 1978.

Paul, J., R. Burhmann, V.K. Gaur, R. Bilham, K. Larson, M.B. Ananda, S. Jade, M. Mukal, T.S. Anupama, G. Satyal, and D. Kumar, The motion and active deformation of India, *Geophys. Res. Lett.*, *28*, 647-650, 2001.

Pollack, H.N., S.J. Hurter, and J.R. Johnson, Heat flow from the Earth's interior: Analysis of the global data set, *Rev. Geophys.*, *31*, 267-280, 1993.

Rajendran, C.P., and K. Rajendran, Characteristics of deformation and past seismicity associated with the 1819 Kutch earthquake, northwestern India, *Bull. Seism. Soc. Am.*, *91*, 407-426, 2001.

Rajendran, K., C.P. Rajendran, M. Thakkar, and M.P. Tuttle, The 2001 Kutch (Bhuj) earthquake: Coseismic surface features and their significance, *Current Science*, *80*, 1397-1405, 2001.

Ranalli, G., *Rheology of the Earth*, 413 pp., Chapman & Hall, London, 1995.

Sella, G.F., T. Dixon, and A. Mao, REVEL: A model for recent plate velocities from space geodesy, *J. Geophys. Res.*, in press, 2002.

Stein, R.S., The role of stress transfer in earthquake occurrence, *Nature*, *402*, 605-609, 1999.

Stein, S., G.F. Sella, and E.A. Okal, The January 26, 2001 Bhuj earthquake and the diffuse western boundary of the Indian plate, in *Plate Boundary Zone*, edited by S. Stein, and J. Freymueller, (this volume), AGU, Washington, D.C., 2002.

Talwani, P., and A. Gangopadhyay, Tectonic framework of the Kachchh earthquake of 26 January 2001, *Seism. Res. Lett.*, *72*, 336-345, 2001.

Turcotte, D.L., and G. Schubert, *Geodynamics: Applications of continuum physics to geological problems*, 450 pp., John Wiley & Sons, New York, 1982.

Williams, C.A., and R.M. Richardson, A rheological layered three-dimensional model of the San Andreas Fault in central and southern California, *J. Geophys. Res.*, *96*, 16597-16623, 1991.

Yang, Y., and M. Liu, Deformation of convergent plates: Evidence from discrepancies between GPS velocities and rigid-plate motions, *Geophys. Res. Lett.*, in press, 2002.

Chapter 4   STRESS EVOLUTION FOLLOWING THE 1811-1812 LARGE EARTHQUAKES IN THE NEW MADRID SEISMIC ZONE

Qingsong Li, Mian Liu, and Eric Sandvol

Abstract. Following a series of large (Mw=7.0-7.5) earthquakes in the New Madrid Seismic Zone (NMSZ) in the central US during 1811 and 1812, more than a dozen moderate-size (M>5) earthquakes occurred in this region, but mostly outside of the NMSZ fault zone. We have simulated the evolution of Coulomb stress and strain energy in the NMSZ and surrounding regions following the large 1811-1812 events in a three-dimensional viscoelastic finite element model. The results show that much of the stress and strain energy released by the large 1811-1812 events has migrated to southern Illinois and eastern Arkansas, consistent with the seismicity distribution. This inherited strain energy in these areas is capable of producing damaging (M 6-7) earthquakes today.

4.1 Introduction

During the winter between 1811 and 1812, at least three large earthquakes (Mw 7.0-7.5) [*Hough et al.*, 2000] occurred in the New Madrid Seismic zone (NMSZ), which is delineated by instrumental seismicity in Fig. 4.1. Each of these main shocks was followed by numerous large aftershocks (M>6.0) [*Johnston and Schweig*, 1996]. The main NMSZ

faults include the southwestern segments (the Blytheville arch and the Blytheville Fault

Zone), the NW trending Reelfoot Fault, and the northeastern segment (the New Madrid

North Fault) (Fig. 4.1). Only the Reelfoot Fault is exposed to the surface, other segments

are delineated by seismicity,reflection and aeromagnetic data [*Hildenbrand and Hendricks*,

1995; *Johnston and Schweig*, 1996]. These faults are believed to be within a failed rift

system formed in Late Proterozoic to Early Cambrian times [*Ervin and McGinnis*, 1975].

We hereinafter use NMSZ fault zones when referring to these fault structures.

The cause of seismicity in the NMSZ is not well understood [*Johnston and Schweig*,

1996]. Paleoseismlogical data indicate two major events, around AD 900 and AD 1450, in

the NMSZ comparable to the large 1811-1812 earthquakes [*Tuttle and Schweig*, 1995;

Tuttle et al., 2002]. These data imply a recurrence interval of ~500 years for large

earthquakes in the NMSZ, at least in the past two thousand years [*Tuttle et al.*, 2002].

However, the GPS data show insignificant strain rates around the NMSZ [*Newman et al.*,

1999], inconsistent with the conclusions drawn from the paleoseimsic data. Some workers

attempted to seek solution in some kind of local loading presumably related to the rift

structure in the lower crust [*Kenner and Segall*, 2000; *Pollitz et al.*, 2001], but these

structures are poorly constrained.

Among the uncertainties of the NMSZ seismicity one fact stands solid – some large

earthquakes occurred here in 1811-1812. In this study we choose to focus on the potential

impact of the 1811-1812 large events on seismicity within the NMSZ and surrounding

regions in the following two centuries. Although thousands of micro-earthquakes (M<4)

have been recorded within the NMSZ in the past decades, most of the major earthquakes

(M>5) in this region since 1812 occurred not within the NMSZ fault zone but in the

surrounding areas (Fig. 4.1). This raises the question of where the next large earthquake in

the central United States would most likely occur.
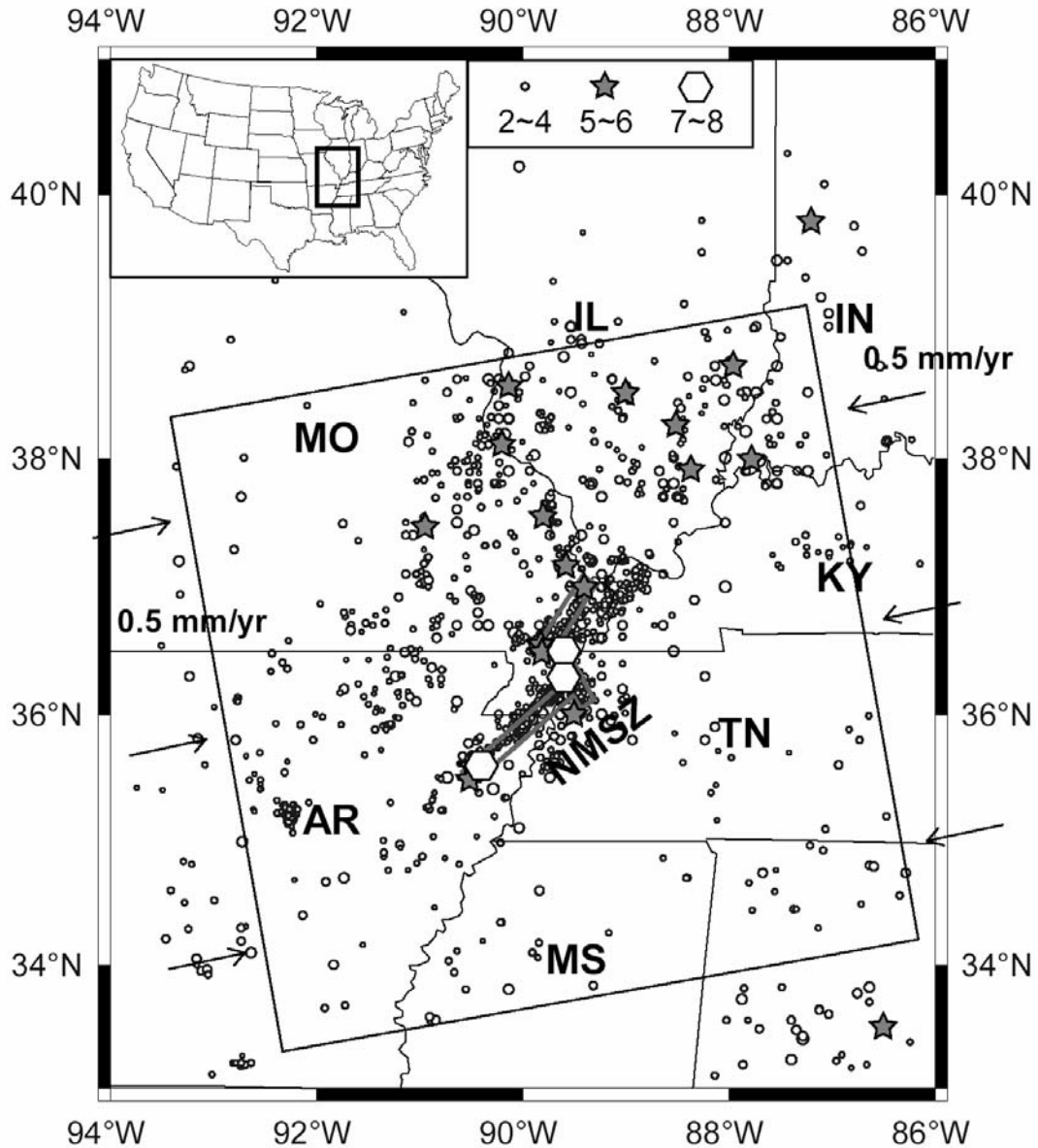
Figure 4.1 Earthquake epicenters in the NMSZ and surrounding regions (the location is shown in the inset). Modern earthquake data (for events M>2 since 1974, circles) are from the NEIC and CERI Catalog (1974-2003); pre-1974 and historic earthquake data (M>5, stars) are from Stover and Coffman [*Stover and Coffman*, 1993]. Hexagons show the large 1811-1812 events [*Stover and Coffman*, 1993]. The NMSZ is delineated by solid lines. The frame and arrows show the model domain and boundary conditions.

4.2 Model

We address this question by simulating the evolution of the Coulomb stress following the 1811-1812 events. Earthquake-induced changes of Coulomb stress have been shown to be useful in predicting spatial patterns of seismicity in plate boundary zones [*King et al.*, 1994; *Stein et al.*, 1992; *Zeng*, 2001], but how these processes work in intraplate settings has not been fully explored. We constructed a three-dimensional finite element model that spans a 556km x 556km area centered on the NMSZ (Fig. 4.1). The model crust is 40 km thick with a viscoelastic rheology. The stiff upper 20 km is assumed to be elastic for deformation over the timescale of hundreds of years. Viscosities between 10^{19} and 10^{21} Pa s, likely the limits for the NMSZ lower crust [*Kenner and Segall*, 2000], were tested in the model. The Young's modulus and the Poisson's ratio are taken to be 8.75×10^{10} Pa and 0.25, respectively, for the entire crust [*Turcotte and Schubert*, 1982].

The compressive stresses across the North American plate were simulated by applying a 0.5 mm/yr velocity boundary condition on the eastern and western edges of the model (Fig. 4.1). This produces a strain rate of ~2x10^{-9}/yr over the model domain, which is likely the upper bound of internal deformation rate within the North American plate based on GPS and seismological data [*Anderson*, 1986; *Newman et al.*, 1999; *Zoback et al.*, 2002]. The NMSZ fault zones are simplified in the model with two vertical strike-slip branches connected by the NW-trending reverse fault dipping 45˚ southwest, based on inferred fault geometry [*Chiu et al.*, 1992; *Mueller and Pujol*, 2001]. The faults were simulated by special fault elements within which plastic deformation is used to simulate stress drop and displacement during earthquakes.   The initial stress state just before the 1811-1812 large earthquakes was unknown; we assume it to be everywhere close to the yield strength of the

upper crust [*Townend and Zoback*, 2000; *Zoback et al.*, 2002], which is consistent with the widespread seismicity in the NMSZ and surrounding regions.

4.3 Results

To focus on stress evolution following the large 1811-1812 earthquakes, we simulated these three events, spanning over three months, as having occurred simultaneously. This was done with ~5 m instant slip along the model NMSZ fault zone, resulting in a Coulomb stress drop of 5 MPa within the fault zone, as estimated by Hough et al. [2000]. The Coulomb stress on a plane is defined as $\sigma_f = \tau_\beta - \mu\sigma_\beta$, where τ_β is the shear stress on the plane, σ_β is the normal stress, and μ is the effective coefficient of friction [*King et al.*, 1994]. For regions outside the NMSZ fault zones where seismogenic faults are not well defined, we calculate the optimal Coulomb stress, which is the stress on planes optimally orientated for failure [*King et al.*, 1994].

Fig. 4.2a shows stress migration immediately following the 1811-1812 events. In the upper crust the maximum stress increases are near the NE and SW ends of the NMSZ. Conversely, stress decreases within the NMSZ fault zones and much of the surrounding areas. Some of the stress migrated to the lower crust under the fault zone, but postseismic viscous relaxation in the ductile lower crust then caused stress to gradually re-accumulate in the upper crust, mainly in the fault zone and in the quadrants of increased coseismic Coulomb stress, similar to previous viscoelastic model results [*Freed and Lin*, 2001; *Rydelek and Pollitz*, 1994]. Although far-field tectonic loading tends to increase stress in the whole region, the rate is slow. Two hundred years after the 1811-1812 large earthquakes, the NMSZ remains in a stress shadow where stress has not reached pre-1811-1812 values.

The largest Coulomb stress increases are in southern Illinois and eastern Arkansas, where most of the major earthquakes since 1812 have occurred (Fig. 4.2).
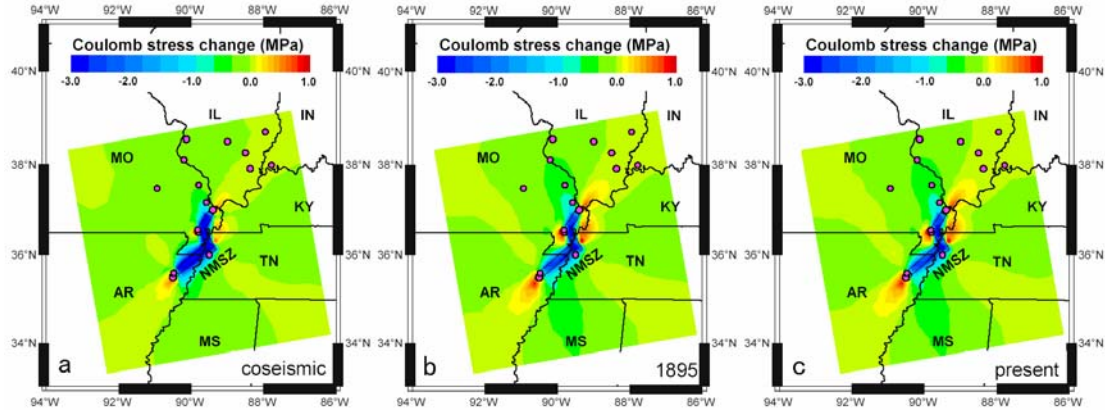
Figure 4.2 (A) Predicted coseismic Coulomb stress change during the 1811-1812 earthquakes in the NMSZ. (B) Predicted Coulomb stress change after the 1843 Marked Tree, Arkansas, and the 1895 Charleston, Missouri, earthquakes. (C) Predicted Coulomb stress change at present. The red dots are the major earthquakes (M>5) since 1812 [*Stover and Coffman*, 1993].

The aftershocks of the 1811-1812 large events were not included in the calculation for lack of constraints, but their effects are likely minor in terms of energy release. This can be seen from Fig. 4.2b where the impact of the two largest earthquakes in the NMSZ region since 1812, the 1895 Charleston, Missouri earthquake (M=6.2) and the 1843 Marked Tree, Arkansas earthquake (M=6.0), were calculated. The results show some local stress changes near the epicentres of these events, but the general stress pattern remains dominated by the 1811-1812 large events. The present Coulomb stress field calculated with these two events (Fig. 4.2c) is similar to that calculated without them. We also found that, although these two events consumed some the strain energy released by the 1811-1812 large events, their impact on the total stain energy budget is minor (see below). Note that the results in Fig.

4.2 were obtained by assuming a complete healing of the NMSZ faults, such that the yield strength returned to the pre-1811-1812 level immediately following the large events. If the NMSZ faults were unhealed or partially healed, stress reaccumulation within the NMSZ fault zone would be even slower.

The postseismic stress change owning to viscous relaxation is dependent on the viscosity of the lower crust and perhaps the lithospheric mantle [*Freed and Lin*, 2001]. Fig. 4.3 shows the predicted stress evolution within the NMSZ and in the ambient regions of increasing Coulomb stresses for two end-member lower crust viscosity values. In both cases postseismic viscous relaxation reduces stress in the lower crust and increases stress in the upper crust; the process is faster when the lower crustal viscosity is lower. However, ineither case stress rebuilding within the NMSZ fault zone lags behind that in the ambient crust including southern Illinois and eastern Arkansas.

Fig. 4.4a shows the calculated seismic energy release based on historic and modern earthquake data from the National Earthquake Information Center (NEIC) catalog (http://neic.usgs.gov/neis/epic/epic.html). We used the Gutenberg-Richter's formula [*Lay and Wallace*, 1995], and approximated all magnitudes as M_s. The spatial pattern is dominated by a dozen moderate sized events (M>5) since 1812, especially the two M~6 events near the NE and SW tips of the NMSZ (Fig. 4.2b). The released seismic energy may be compared with the change of strain energy, which is associated with the stress migration following the 1811-1812 large earthquakes.   Fig. 4.4b shows the excess strain energy, calculated by assigning a strain change in each element, if needed, to bring the deviatoric stress below the yield strength of the crust during a time step. The total excess strain energy accumulation over a single time step at a given place is given by a vertical integration of
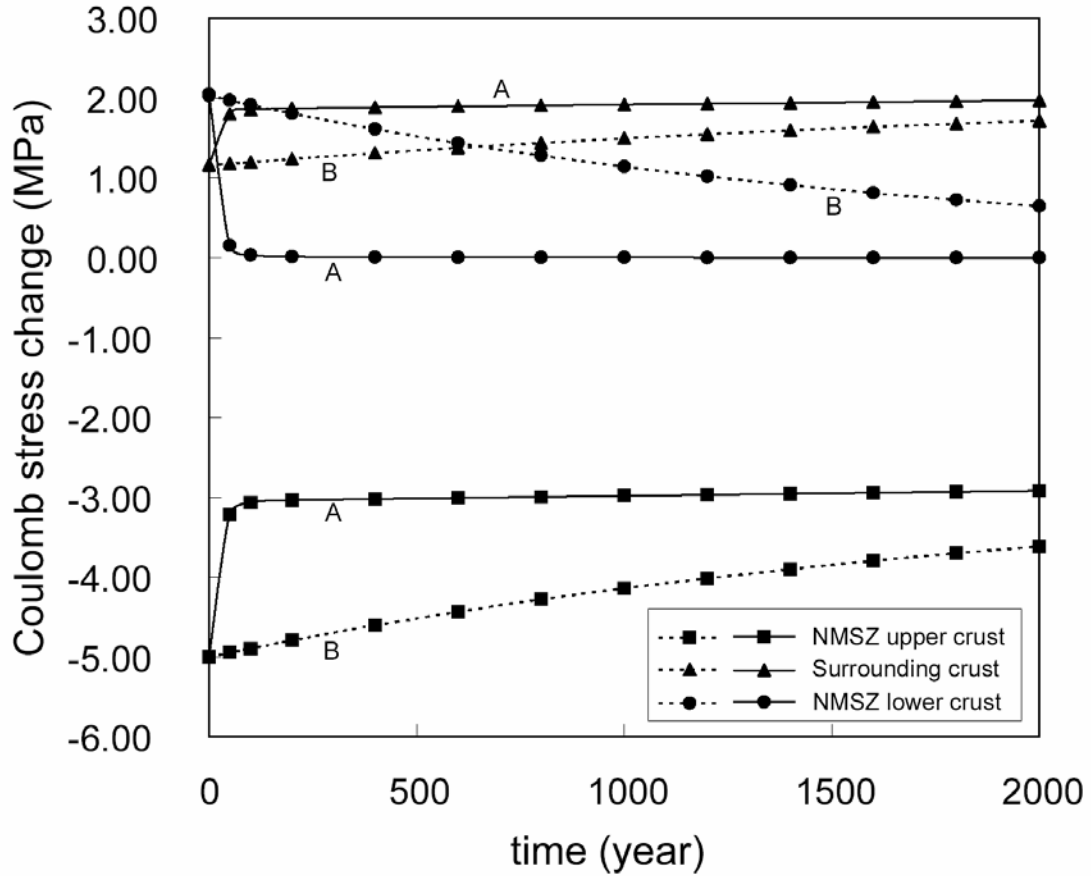
Figure 4.3 The calculated evolution of the Coulomb stress since the 1811-1812 large earthquakes. The dashed lines are for case B with a higher viscosity $(1.0 \times 10^{21}$ Pa s) for the lower crust, and the solid lines are for case A with a lower viscosity $(1.0 \times 10^{19}$ Pa s) for the lower crust. The stress evolution in the upper crust outside of the NMSZ (surrounding crust) is for the quadrants of increasing Coulomb stress (see Fig. 4.2).

the product of stress and the strain change. The spatial pattern of the calculated excess strain energy is consistent with the seismic energy release in the past two centuries (Fig. 4.4a), but the magnitude is two to three orders higher presumably because not all energy has been released via earthquakes. The relation between strain energy before the large earthquakes, the energy released during them, and the fraction of energy radiated as seismic waves remains unclear [Kanamori, 1978]. Assuming only ~10% of the energy was

radiated as seismic waves [Lockner and Okubo, 1983], we can multiply the estimated

seismic energy release (Fig. 4.4a) by 10 to get an estimate of total energy released by

earthquakes in the past two centuries. Subtracting it from the excess strain energy in Fig.

4.4b gives the residual strain energy, some of it may be released by future earthquakes. The

partition between seismic and aseismic energy is uncertain [Ward, 1998]. Fig. 4.4c shows

the available seismic energy if only 2.5% of the total excess strain energy will be released

in future earthquakes. This energy is still capable to produce a number of $M = 6$-7

earthquakes in southern Illinois and eastern Arkansas today.
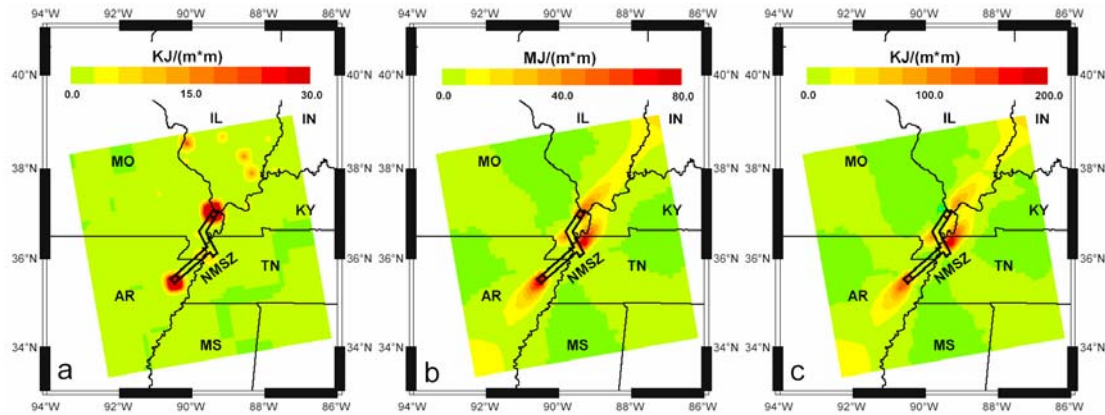
Figure 4.4 (A) Estimated seismic energy release in the NMSZ and surrounding regions since 1812. (B) Predicted total excess strain energy since the 1811-1812 events. (C) Predicted seismic strain energy in the crust today available for producing earthquakes.

4.4 Discussion and Conclusions

We have shown that some of the strain energy released during the 1811-1812

earthquakes may have migrated to the ambient crust and perhaps caused, or at least

triggered, the moderate sized earthquakes in regions surrounding the NMSZ. The

calculated build up of Coulomb stress and strain energy from the 1811-1812 events is high

enough to produce some damaging earthquakes today in southern Illinois and eastern Arkansas. Similar conclusions have been reached from studies of recent instrumentally recorded aftershocks [*Gomberg*, 1993; *Mueller et al.*, 2004].

The prediction of the NMSZ fault zone remaining in a stress shadow two hundred years after the 1811-1812 large earthquakes is hardly surprising, given the stability of the North American plate interior [*Dixon et al.*, 1996; *Gan and Prescott*, 2001]. The $<2 \times 10^{-9}$ /yr strain rate within the stable North America [*Gan and Prescott*, 2001] implies a <0.02 MPa far-field secular loading since 1812, much less than the stress released by the 1811-1812 earthquakes (~5 MPa). This is significantly different from earthquakes in plate boundary zones where the accumulated strain energy is dominated by tectonic loading. To reconcile with the paleoseismic evidence of ~500 year recurrence interval for large earthquakes in the NMSZ, some mechanisms of local loading is required. These mechanisms include sinking of a mafic body within the Reelfoot rift [*Pollitz et al.*, 2001] and a sudden thermal event that weakens the NMSZ lithosphere [*Kenner and Segall*, 2000]. Further testing of these mechanisms needs a more refined images of lower crustal and mantle lithospheric structures than those currently available. A local loading under the NMSZ would enhance the strain energy in the ambient crust predicted in this study.

4.5 Acknowledgements

4.6 References

Anderson, J.G., Seismic strain rates in the central and eastern United States, *Seismo. Soc. Am. Bull.*, *76* (1), 273-290, 1986.

Chiu, J.M., A.C. Johnston, and Y.T. Yang, Imaging the active faults of the central New Madrid seismic zone using PANDA array data, *Seismol. Res. Lett.*, *63* (3), 375-393, 1992.

Dixon, T.H., A. Mao, and S. Stein, How rigid is the stable interior of the North American plate?, *Geophys. Res. Lett.*, *23* (21), 3035-3038, 1996.

Ervin, C.P., and L.D. McGinnis, Reelfoot Rift; reactivated precursor to the Mississippi Embayment, *Geol. Soc. Am. Bull.*, *86* (9), 1287-1295, 1975.

Freed, A.M., and J. Lin, Delayed triggering of the 1999 Hector Mine earthquake by viscoelastic stress transfer, *Nature*, *411*, 180-183, 2001.

Gan, W., and W.H. Prescott, Crustal deformation rates in central and eastern U.S. inferred from GPS, *Geophys. Res. Lett.*, *28* (19), 3733-3736, 2001.

Gomberg, J.S., Tectonic deformation in the New Madrid seismic zone; inferences from map view and cross-sectional boundary element models, *J. Geophys. Res.*, *98* (4), 6639-6664, 1993.

Hildenbrand, T.G., and J.D. Hendricks, Geophysical setting of the Reelfoot Rift and relations between rift structures and the New Madrid seismic zone, *U.S. Geol. Surv. Prof. Pap.*, E1-E30, 1995.

Hough, S.E., J.G. Armbruster, L. Seeber, and J.F. Hough, On the modified Mercalli intensities and magnitudes of the 1811-1812 New Madrid earthquakes, *J. Geophys. Res.*, *105* (10), 23,839-23,864, 2000.

Johnston, A.C., and E.S. Schweig, The enigma of the New Madrid earthquakes of 1811-1812, *Annu. Rev. Earth Planet. Sci.*, 1996.

Kanamori, H., Quantification of earthquakes, *Nature*, *271*, 411-414, 1978.

Kenner, S.J., and P. Segall, A mechanical model for intraplate earthquakes; application to the New Madrid seismic zone, *Science*, *289* (5488), 2329-2332, 2000.

King, G.C.P., R.S. Stein, and J. Lin, Static stress changes and the triggering of earthquakes, *Bull. Seismol. Soc. Am.*, *84* (3), 935-953, 1994.

Lay, T., and T.C. Wallace, *Modern Global Seismology*, 383-385 pp., Academic Press, San

Diego, 1995.

Lockner, D.A., and P.G. Okubo, Measurements of frictional heating in granite, *J. Geophys. Res.*, *88* (5), 4313-4320, 1983.

Mueller, K., S.E. Hough, and R. Bilham, Analysing the 1811-1812 New Madrid earthquakes with recent instrumentally recorded aftershocks, *Nature*, *429*, 284-288, 2004.

Mueller, K., and J. Pujol, Three-Dimensional Geometry of the Reelfoot Blind Thrust: Implications for Moment Release and Earthquake Magnitude in the New Madrid Seismic Zone, *Bull. Seism. Soc. Am.*, *91* (6), 1563-1573, 2001.

Newman, A., S. Stein, J. Weber, J. Engeln, A. Mao, and T. Dixon, Slow deformation and lower seismic hazard at the New Madrid Seismic Zone, *Science*, *284* (5414), 619-621, 1999.

Pollitz, F.F., L. Kellogg, and R. Buergmann, Sinking mafic body in a reactivated lower crust; a mechanism for stress concentration at the New Madrid seismic zone, *Bull. Seismol. Soc. Am.*, *91* (6), 1882-1897, 2001.

Rydelek, P.A., and F.F. Pollitz, Fossil strain from the 1811-1812 New Madrid earthquakes, *Geophys. Res. Lett.*, *21*, 2303-2306, 1994.

Stein, R.S., G.C. King, and J. Lin, Change in failure stress on the southern San Andreas fault system caused by the 1992 magnitude = 7.4 Landers earthquake, *Science*, *258* (5086), 1328-1332, 1992.

Stover, C.W., and J.L. Coffman, Seismicity of the United States, 1568-1989 (revised), *U.S. Geol. Surv. Prof. Pap.*, 418, 1993.

Townend, J., and M.D. Zoback, How faulting keeps the crust strong, *Geology*, *28* (5), 399-402, 2000.

Turcotte, D.L., and G. Schubert, *Geodynamics: Applications of continuum physics to geological problems*, 450 pp., John Wiley & Sons, New York, 1982.

Tuttle, M.P., and E.S. Schweig, Archeological and pedological evidence for large prehistoric earthquakes in the New Madrid seismic zone, central United States, *Geology*, *23*, 253-256, 1995.

Tuttle, M.P., E.S. Schweig, J.D. Sims, R.H. Lafferty, L.W. Wolf, and M.L. Haynes, The earthquake potential of the New Madrid seismic zone, *Bull. Seismol. Soc. Am.*, *92* (6), 2080-2089, 2002.

Ward, S.N., On the consistency of earthquake moment rates, geological fault data, and

space geodetic strain; the United States, *Geophys. J. Int.*, *134* (1), 172-186, 1998.

Zeng, Y., viscoelastic stress-triggering of the 1999 Hector Mine earthquake by the 1992 Landers earthquake, *Geophys. Res. Lett.*, *28* (15), 3007-3010, 2001.

Zoback, M.D., J. Townend, and B. Grollimund, Steady-state failure equilibrium and deformation of intraplate lithosphere, *Int. Geology Rev.*, *44* (5), 383-401, 2002.

Chapter 5   STRESS EVOLUTION AND SEISMICITY IN THE CENTRAL-EASTERN USA: INSIGHTS FROM GEODYNAMIC MODELING

Qingsong Li, Mian Liu, Qie Zhang, and Eric Sandvol

ABSTRACT. Although the central and eastern United States (CEUS) is in the interior of the presumably stable North American plate, seismicity there is widespread, and its causes remain uncertain. Here we explore the evolution of stress and strain energy in intraplate seismic zones, and contrast it with that in interplate seismic zones, using simple viscoelastic finite element models. We find that large intraplate earthquakes can significantly increase Coulomb stress and strain energy in the surrounding crust. This inherited strain energy may dominate the local strain energy budget for thousands of years following main shocks, in contrast to interplate seismic zones where strain energy is dominated by tectonic loading. We show that strain energy buildup from the 1811-1812 large events in the New Madrid seismic zone (NMSZ) may explain some of the moderate sized earthquakes in this region since 1812, and that the inherited strain energy is capable of producing some damaging earthquakes (M>6) today in southern Illinois and eastern Arkansas even in the absence of local loading. Without local loading, however, the NMSZ would have remained in a stress shadow where stress has not fully restored from the 1811-1812 events. We have also derived a Pn velocity map of the CEUS using available seismic data, and simulated the long-term Coulomb stress in the CEUS. The predicted high Coulomb stress concentrates near the margins of the North American tectosphere, correlating spatially with most seismicity in the CEUS.

5.1 Introduction

Plate tectonic theory provides a successful geodynamic framework for understanding the majority of earthquakes that occur along plate boundary zones. However, it offers no ready explanation for earthquakes in the presumably rigid plate interiors. One such region is the central-eastern United States (CEUS), defined broadly as the region of the continental USA east of the Rocky Mountains. Although the CEUS is in the middle of the North America plate where Cenozoic crustal deformation is minimal, both historic earthquakes and instrumentally recorded earthquakes are abundant. Major seismic zones in the CEUS include the following [*Dewey et al.*, 1989] (Fig. 5.1):

1. *The New Madrid seismic zone (NMSZ) and Mississippi Embayment*: was the site of the famous 1811-1812 large earthquakes. The magnitudes of the largest three events were Mw 7-7.5 [*Hough et al.*, 2000]. Paleoseismic results indicate that major earthquakes occurred around 900 and 1400 AD [*Kelson et al.*, 1996; *Tuttle et al.*, 2002]. Modern instrumentation has recorded thousands of events since 1977.

2. *Southern Valley and Ridge:* also referred to as the eastern Tennessee seismic zone, where modern seismicity is concentrated beneath the Valley and Ridge province, near the western edge of the Appalachians. The largest historical event here was the M 5.8 Giles County, Virginia, earthquake of May 31, 1897 [*Nuttli et al.*, 1979].

3. *South Carolina seismic zone:* The best-known event in this region was a destructive (M~ 6.5-7.0) event near Charleston, South Carolina, on August 31, 1886 [*Nuttli et al.*, 1979]. Paleoseismic studies indicate at least two prehistoric

earthquakes in the past 3000 years [*Obermeier et al.*, 1985; *Talwani and Cox*, 1985].

4. *New England and the St. Lawrence River Valley:* Earthquake epicenters in central New England, upstate New York, and adjacent Canada form a northwest-trending belt of seismicity, sometimes called the Boston-Ottawa zone [*Diment et al.*, 1972; *Sbar and Sykes*, 1973]. The largest historic earthquake in the U.S. part of this zone was probably the M~6 Cape Ann, Massachusetts, earthquake of 1755 [*Street and Lacroix*, 1979]. Further north in the St. Lawrence River valley, numerous events with magnitude 6-7 have been recorded.

Despite intensive studies, the mechanics of earthquakes in the CEUS remain poorly understood. Some workers have suggested that these seismic zones are within ancient rifts, thus proposing crustal weakness as the main cause of these earthquakes [*Johnston*, 1996; *Johnston and Kanter*, 1990]. Others have suggested stress concentration by various factors, including regional and local crustal structures, as the main cause [*Grana and Richardson*, 1996; *Grollimund and Zoback*, 2001; *Kenner and Segall*, 2000; *Pollitz et al.*, 2001a; *Stuart et al.*, 1997]. Although intraplate earthquakes are commonly believed to differ fundamentally from interplate earthquakes, their differences in dynamics are not clear. In this study, we first explore the basic mechanics of intraplate seismic zones and compare them to that of interplate seismic zones. We then apply the results to investigate seismicity in the NMSZ. Finally, we present a regional geodynamic model of CEUS constrained by the lithospheric structure based on seismic studies by others and our Pn tomography.
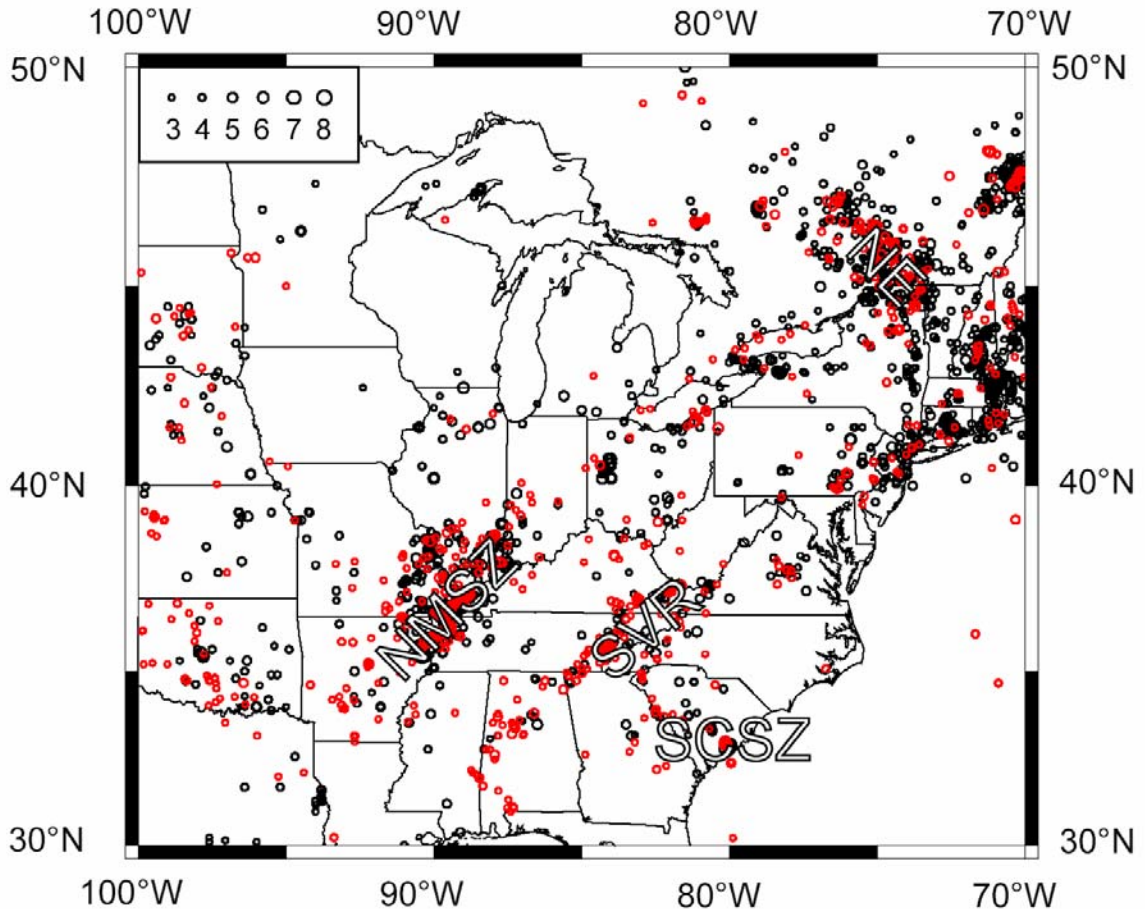
Figure 5.1 Seismicity in central-eastern United States (CEUS) from NEIC catalog. Black circles: historic events (1800-1973); red circles: modern events (1973-2004). Major seismic zones include the New Madrid seismic zone (NMSZ); the Southern Valley and Ridge (SVR); the South Carolina Seismic Zone (SCSZ); the New England and the St. Lawrence River Valley seismic zone (NE).

5.2 The Mechanics of Intraplate vs. Interplate Seismic Zones

We have developed three-dimensional viscoelastic models to explore the differences

in stress evolution between intraplate and interplate strike-slip seismic zones. To illustrate

the basic physics, we have kept the models relatively simple. We consider two contrasting

properties of these zones: 1) intraplate seismic zones are of finite length, surrounded by

strong ambient crust, whereas interplate seismic zones are effectively infinitely long; 2)

tectonic loading for intraplate seismic zones is applied at far-field plate boundaries,

typically producing low strain rates, whereas interplate seismic zones are loaded directly

by relative motions of tectonic plates, causing relatively high strain rates (Fig. 5.2). The

model rheology is a viscoelastic (Maxwellian) medium. Both models include a 20 km thick

stiff upper crust and a ductile lower crust. The viscosity for the upper crust is 8.0×10^{23} Pa s,

making it essentially elastic for the timescales (thousands of years) considered here. For

the lower crust a range of viscosity values (1.0×10^{19} - 1.0×10^{21} Pa s) is explored for the

effects of postseismic relaxation. The model domain is 500 x 500 km. For the intraplate

model (Fig. 5.2a), a 150 km long fault zone is used to simulate a finite seismic zone. The

boundary conditions include 0.5 mm/yr compression imposed on the two sides of the

model domain. The resulting strain rate is ~2.0×10^{-9}/yr, close to the upper bound for the

CEUS [*Gan and Prescott*, 2001; *Newman et al.*, 1999]. Young's modulus and the Poisson's

ratio are 8.75×10^{10} Pa and 0.25, respectively, for the entire crust [*Turcotte and Schubert*,

1982]. For the interplate model, the fault zone cuts across the entire model domain (Fig.

5.2b), and the boundary condition is 10 mm/yr on both sides, causing an average slip rate

of ~28 mm/yr along the fault zone in the model, similar to that on the San Andreas Fault

[*Becker et al.*, 2005; *Bennett et al.*, 2004]. In both models the fault zones are represented by

special elements, on which we simulate earthquakes by using instant plastic strain to lower

the stress to below the yield strength [*Li et al.*, 2005].
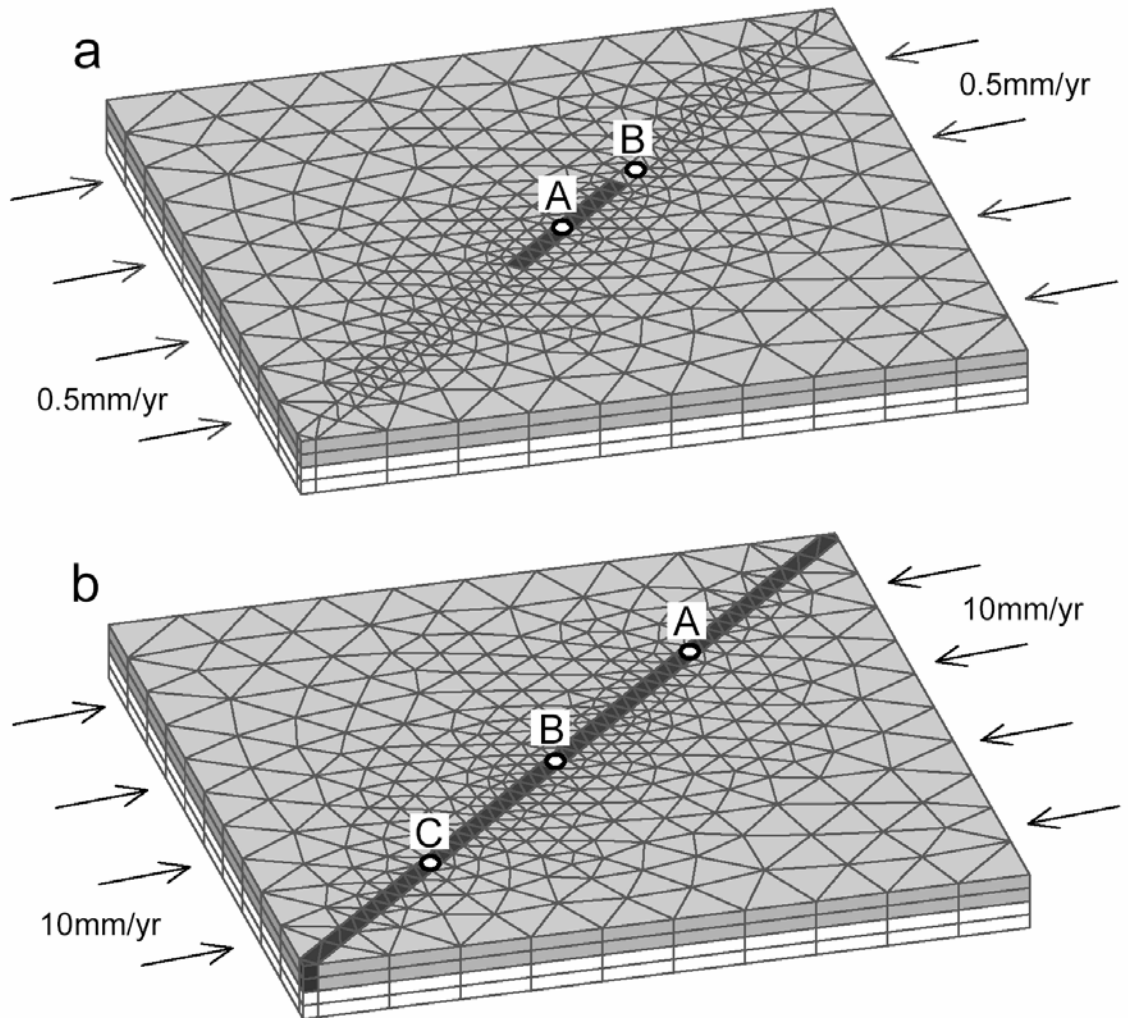
Figure 5.2 Finite element models for intraplate (a) and interplate (b) strike-slip seismic fault zones (in dark). Points A and B are where stress evolution is shown in Fig. 5.4 and 5.7.

5.2.1 Intraplate seismic zones

Many seismic zones in the CEUS are marked by past large earthquakes, whose initial triggering mechanism is uncertain. Here we focus on stress evolution in the seismic zones following a large earthquake.

Fig. 5.3 shows the calculated evolution of the Coulomb stress following a large intraplate earthquake. The Coulomb stress on a plane is defined as

$$\sigma_f = \tau_\beta - \mu\sigma_\beta \qquad\qquad (5\text{-}1)$$

where τ_β is the shear stress on the plane, σ_β is the normal stress, and μ is the effective

coefficient of friction [*King et al.*, 1994]. Outside the main fault zone, we calculate the

optimal Coulomb stress, which is the stress on planes optimally orientated for failure [*King

et al.*, 1994]. We assume that initially in the upper crust the stress is close to the yield

strength, a condition that might be applicable to many continental interiors [*Townend and

Zoback*, 2000; *Zoback et al.*, 2002] and is consistent with the widely scattered seismicity in

and around the seismic zones in the CEUS (Fig. 5.1). The model started with a large

earthquake, simulated by a 7.5-meter sudden slip across the entire fault plane. This event is

equivalent to an M ~ 8.0 earthquake, which caused ~5 MPa stress drop within the fault

zone. Coseismic stress release from the fault zone migrates to the tip regions of the fault

zone and loads the lower crust below the fault zone. Postseismic viscous relaxation in the

lower crust then causes the stress to reaccumulate within the upper crust, mainly near the

tips of the fault zone. Similar results have been reported in previous viscoelastic models

[*Freed and Lin*, 2001; *Pollitz et al.*, 2001b]. Note that 200 years after the main earthquake,

the fault zone remains in a stress shadow where the stress relieved during the earthquake

has not been fully restored. This is mainly due to slow tectonic loading, whose effects are

insignificant over 200 years (compare Fig. 5.3b and 5.3c). In this model we assumed a

complete healing of the fault zone, such that the yield strength returned to the original level

immediately following the main shock. If the fault zone were unhealed or partially healed,

stress reaccumulation within the fault zone would be even slower.

In addition to the rate of tectonic loading, postseismic stress evolution depends on the

rheology of the lithosphere, especially the lower crust. Fig. 5.4 shows the effects of lower

crustal viscosity on the modeled stress evolution. A less viscous lower crust causes more rapid viscous relaxation and stress reloading in the upper crust. However, without fast tectonic loading from the far-field, the total amount of stress restoration within the fault zone is largely determined by the stress relieved from the earthquake. For the viscosity range typical of the lower crust ($10^{19} - 10^{21}$ Pas), viscous relaxation and far-field loading can not fully restore stress in the fault zone thousands of years after the major earthquake. This may be a fundamental difference between intraplate and interplate seismic zones; the latter is directly loaded by plate motions at high rates, and a ruptured fault segment can also be influenced by earthquakes on nearby fault segments (see below).
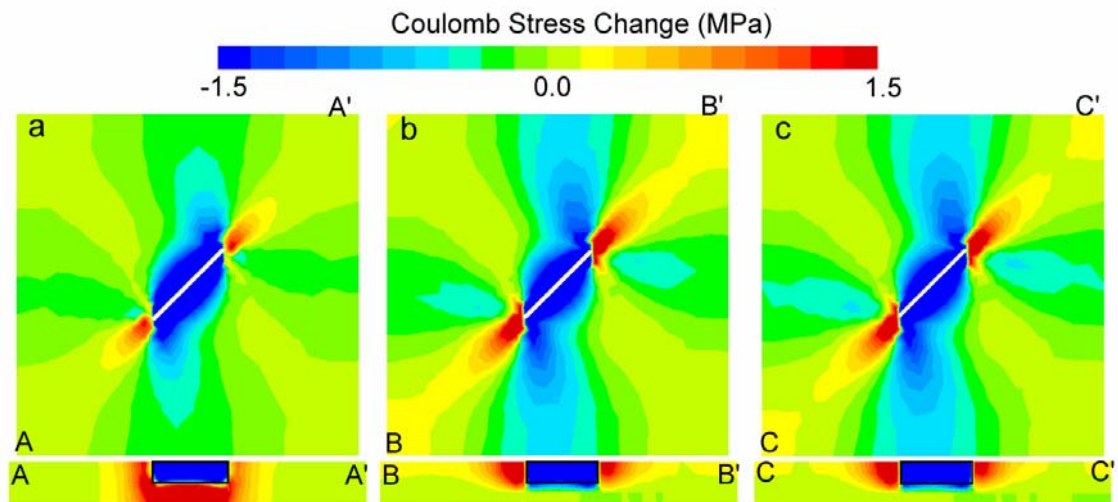
Figure 5.3 Predicted Coulomb stress change following a large earthquake in the intraplate seismic zone. (a) Co-seismic stress change. (b) The sum of co-seismic and post-seismic (200 years) stress change. (c) Same as (b) but without boundary loading. The bottom panels are depth sections, with 200% vertical exaggeration. The white lines (map view) and black frames (depth section) show the ruptured fault zone. Calculated assuming a viscosity of 10^{19} Pa s for the lower crust.
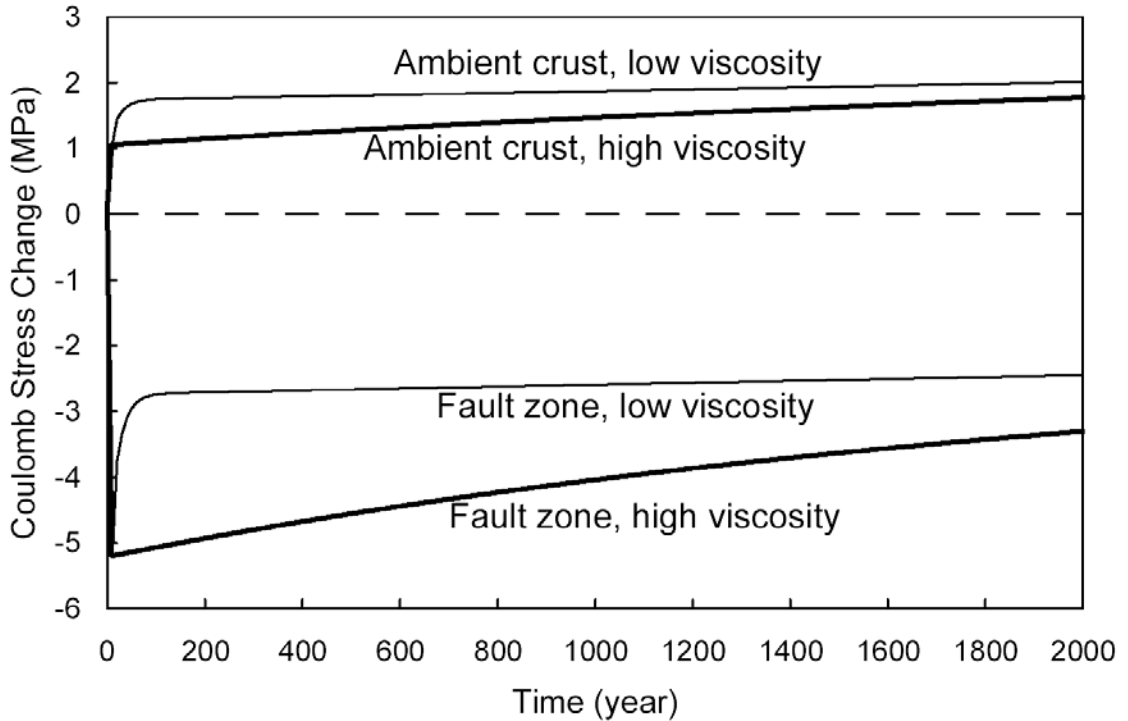
Figure 5.4 Predicted Coulomb stress evolution in the fault zone (point A in Fig. 5.2a) and the ambient crust near the fault tips (point B in Fig. 5.2a) with two values for the lower crust viscosity: high (10^{21} Pa s); low (10^{19} Pa s). The Coulomb stress in the fault zone drops instantly during an earthquake. The initial stress restoration is accelerated by viscous relaxation in the lower crust at a rate that is sensitive to the viscosity. Further stress restoration is mainly controlled by tectonic loading.

Associated with the stress evolution is a migration and accumulation of strain energy, defined as

$$E = \frac{1}{2}\sigma'_{ij}\varepsilon'_{ij} \tag{5-2}$$

where σ'_{ij} and ε'_{ij} are the deviatoric stress and strain tensors respectively, using the Einstein summation convention for indexes i and j. Fig. 5.5 shows the coseismic and postseismic changes of stain energy. Similar to the stress change (Fig. 5.3), most increase of strain energy is near the tips of the fault zone. Because of the slow tectonic loading,

much of the strain energy is inherited from the main shock. It would take thousands of years for the far-field tectonic loading to accumulate a comparable amount of strain energy.
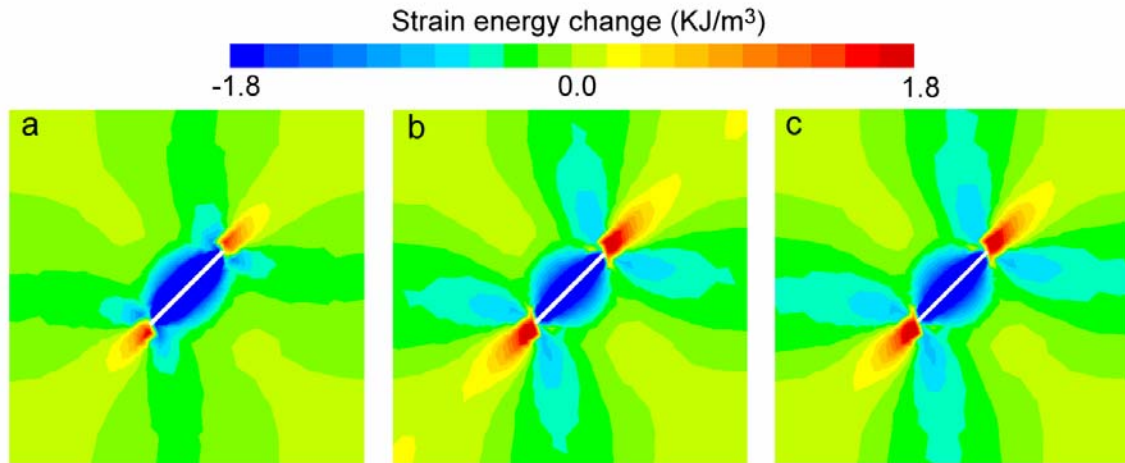
Figure 5.5 Predicted strain energy change in an intraplate seismic zone in map view. (a) co-seismic strain energy change. (b) Total strain energy change 200 years after the main shock. (c) Same as (b) but without tectonic loading. The similarity between (b) and (c) shows the dominance of the inherited strain energy. White lines show the fault zone that ruptured.

5.2.2 Interplate seismic zones

We may better appreciate the stress and strain energy evolution in intraplate seismic zones by contrasting with interplate seismic zones (Fig. 5.2b). Some of the processes are similar. An interplate earthquake relieves stress to the lower crust and the tips of the ruptured fault segment. Viscous relaxation in the lower crust further loads the upper curst, similar to what occurs in intraplate seismic zones. However, the high strain rates associated with plate motions restore stress in the ruptured segment more quickly than in intraplate fault zones. The essentially infinitely long fault zone also confines earthquakes to largely be within, and migrate along, the fault zone (Fig. 5.6a). Usually other segments rupture

before an earthquake repeats on the same segment (Fig. 5.6b). Thus for each segment of the ruptured fault zone, postseismic stress recovery may be affected by three major factors: tectonic loading, viscous relaxation, and stress migration from nearby earthquakes. Fig. 5.7 illustrates such stress evolution at three neighboring points in the fault zone. An earthquake at one of these points causes an instant stress drop. Postseismic stress restoration at the ruptured segment is fast within the first few tens of years because of both tectonic loading and viscous relaxation in the lower crust, transferring stress to the upper crust. A period of roughly steady-state stress buildup follows, resulting from tectonic loading. Sudden stress jumps may occur when a nearby segment ruptures, which may trigger a new earthquake. Such dynamic behavior has been reported in many interplate seismic zones including the San Andreas Fault [*Lin and Stein*, 2004; *Rydelek and Sacks*, 2001; *Stein et al.*, 1997].

We have shown that, in an intraplate seismic zone, strain energy released from a large earthquake will migrate to the surrounding regions and dominate the local strain energy budget for thousands of years (Fig. 5.5). This is generally not true for interplate seismic zones, where tectonic loading dominates the strain energy budget. Fig. 5.8 shows one selected episode of the interplate model experiment. Here postseismic energy evolution is influenced by strain energy migration from the ruptured segment, viscoelastic reloading, and tectonic loading. Fig. 5.8c and Fig. 5.8d compare strain energy in the model crust 200 years after the earthquake, with and without tectonic loading. Clearly, tectonic loading dominates the strain energy evolution. To show the cumulative strain energy produced from tectonic loading, we artificially prohibited earthquakes for the period shown here. In reality strain energy will be modulated by ruptures of other segments of the fault zone (Fig. 5.6-5.7).
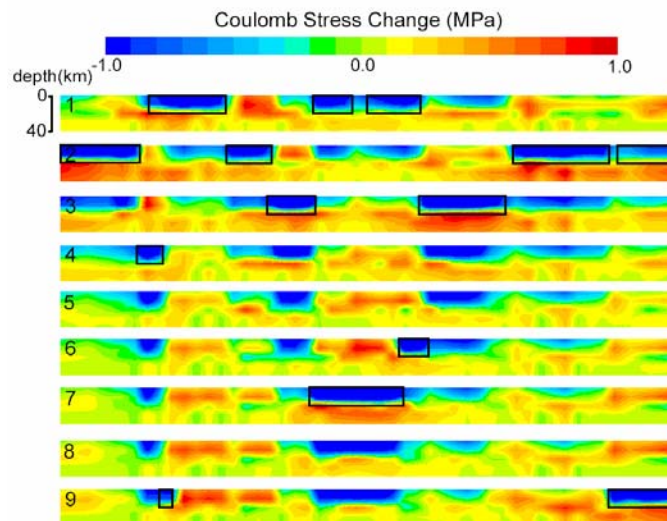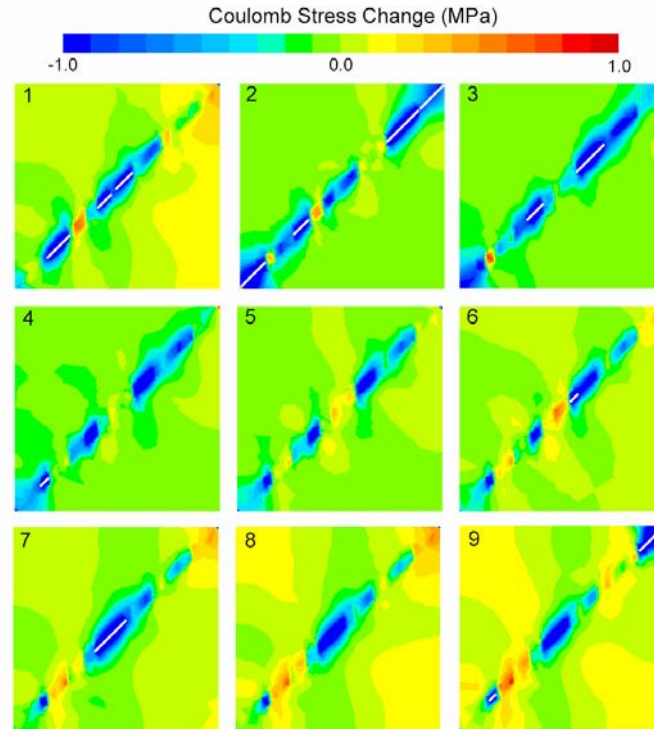
Figure 5.6 (a) Snapshots of the predicted stress evolution (map view) for the model of interplate seismic zone (Fig. 5.2b). The time interval between successive panels is 20 years. The sequence shows a selected period of the simulations of stress changes with ruptures of the high stress segments. (b) Depth sections of the predicted stress evolution shown in Fig. 5.6a. The labels of the panels correspond to the map view panels in Fig. 5.6a. The white lines (map view) and black frames (depth sections) mark the fault segments that have ruptured during the 20-year time interval.
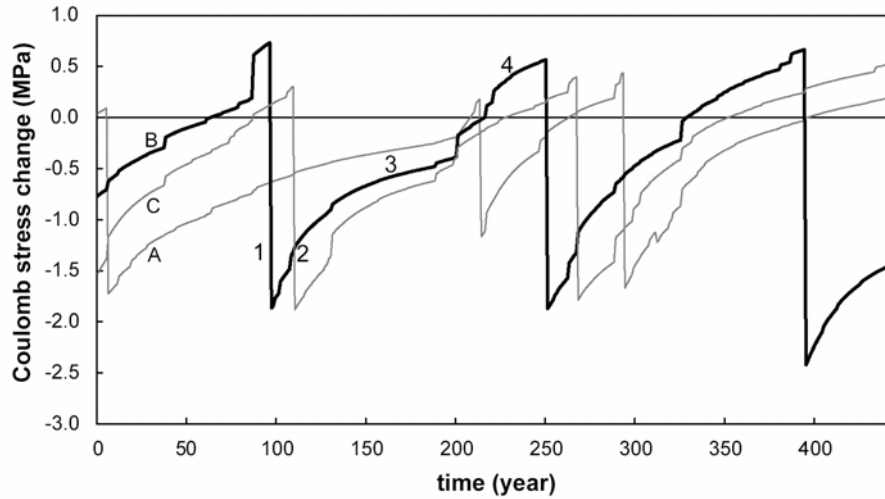
Figure 5.7 Predicted Coulomb stress evolution at three points on the interplate seismic fault zone (see Fig. 5.2b). At each point the cycle of stress evolution includes four stages: (1) stress drop during an earthquake; (2) accelerated stress restoration because of viscous relaxation of the lower crust; (3) steady stress increase mainly from tectonic loading, and (4) stress jump due to triggering effect of nearby earthquakes.
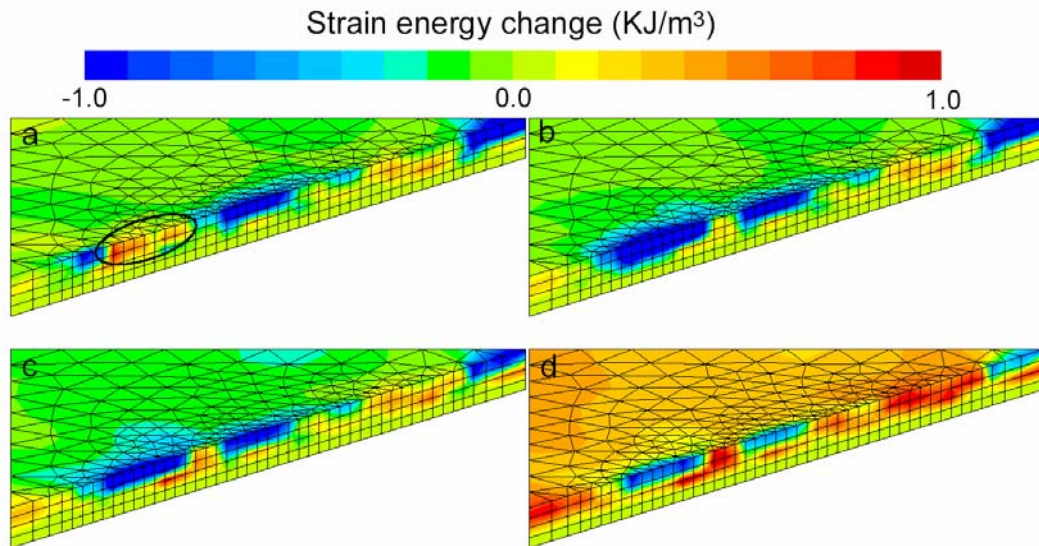
Figure 5.8 Predicted evolution of strain energy in an interplate seismic zone for a selected period. (a) energy distribution before an earthquake (ellipse marks the ruptured area); (b) energy distribution immediately after the earthquake; (c) energy distribution after 200 years without tectonic boundary loading; (d) energy distribution after 200 years with tectonic boundary loading.

5.3 Stress Evolution and Seismicity in the NMSZ

In this section we apply the model results to the NMSZ, perhaps the best known seismic zone in the CEUS. At least three large earthquakes occurred here within three months in the winter of 1811-1812. The magnitudes of these events are estimated to be 7-7.5 [*Hough et al.*, 2000]. Since then a dozen or so major events (M 5-6) have occurred in the NMSZ and surrounding regions, and modern instruments have recorded thousands of small events in the past few decades (Fig. 5.9).

The NMSZ fault zone is generally delineated by the seismicity. Only one segment of the fault system, the NW-trending Reelfoot Fault, has clear surface expression. Other parts of the NMSZ fault zone, including the southwestern segments (Cottonwood Grove fault) and the northeastern segment (New Madrid North Fault), are inferred mainly from reflection seismic and aeromagnetic data, and seismicity [*Hildenbrand and Hendricks*, 1995; *Johnston and Schweig*, 1996]. The Reelfoot fault is a reverse fault; whereas the southwestern and northeastern segments are inferred to be right-lateral faults from morphologic and geologic features [*Gomberg*, 1993]. These faults are believed to be within a failed rift system formed in Late Proterozoic to Early Cambrian times [*Ervin and McGinnis*, 1975]. Below we use "NMSZ" when referring to the geographic region of concentrated seismicity, and "NMSZ fault zone" when referring to these fault structures.

The results in the previous section indicate that following the 1811-1812 large earthquakes, the NMSZ fault zone would still remain in a stress shadow where Coulomb stress is lower than the pre-1811-1812 level, a condition unfavorable for repetition of the large earthquakes. This has important implications for assessing earthquake hazards in the NMSZ. Here we further explore this issue with a more realistic model (Fig. 5.9). The
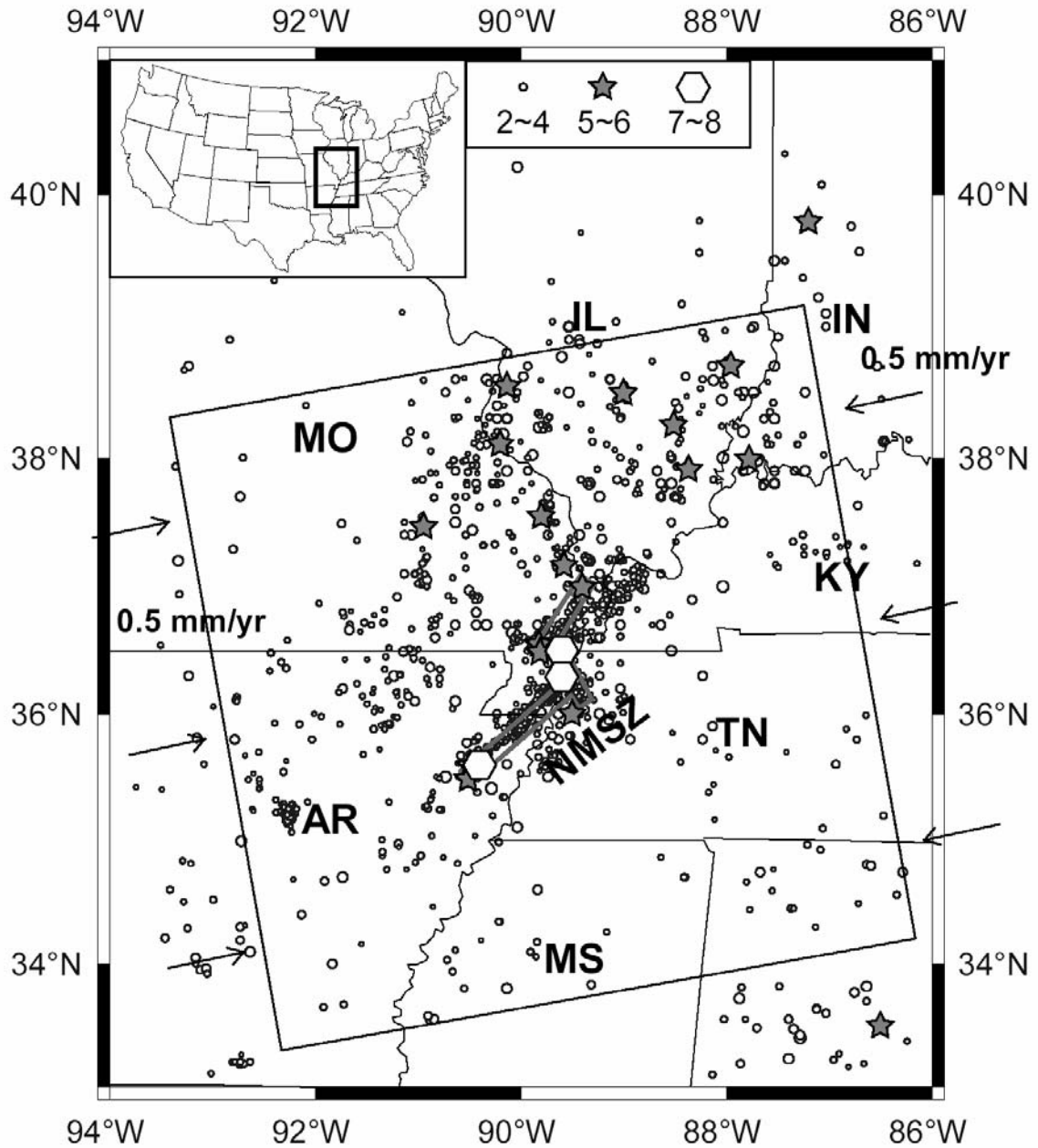
Figure 5.9 Earthquake epicenters in the NMSZ and surrounding regions (the inset shows the location). Modern earthquake data (for events M>2 since 1974, circles) are from the NEIC and CERI Catalog (1974-2003); pre-1974 and historic earthquake data (M>5, stars) are from Stover and Coffman [1993]. Hexagons show the large 1811-1812 events [*Stover and Coffman*, 1993]. The NMSZ is delineated by thick grey lines. The frame and arrows show the model domain and boundary conditions.

NMSZ fault zones are represented by two vertical strike-slip branches approximating the northeastern and southwestern fault segments, connected by the NW-trending reverse fault dipping 45˚ southwest, based on inferred geometry of the Reelfoot Fault [*Chiu et al.*, 1992; *Mueller and Pujol*, 2001]. The compressive stresses across the North American plate were simulated by applying a 0.5 mm/yr velocity boundary condition on the eastern and western edges of the model domain (Fig. 5.9). This produces a strain rate of $\sim2x10^{-9}$/yr within the model domain, likely the upper bound of internal deformation rate within the North American plate based on GPS and seismological data [*Anderson*, 1986; *Newman et al.*, 1999; *Zoback et al.*, 2002]. Other model parameters, including the initial conditions and rheological structures, are similar to those in Fig. 5.2a.

It has been concluded that three large earthquakes occurred on the Reelfoot fault and the southwestern branch of the NMSZ (the Cottonwood Grove fault) between December 1881 to February 1882 [*Johnston*, 1996; *Johnston and Schweig*, 1996]. Some recent studies have suggested that there may be four large events in the 1811-1812 sequence of events [*Hough et al.*, 2000], and at least one of the main shocks may be outside the NMSZ [*Hough et al.*, 2005; *Mueller et al.*, 2004]. Because our focus here is the long-term effects of the large 1811-1812 events, we ignore the detailed rupture sequences and treat these large events as having occurred simultaneously along the entire fault zones. This was simulated with ~5 m instant slip along the model fault zones, resulting in a Coulomb stress drop of 5 MPa within the fault zones, as estimated by Hough et al. [2000]. Fig. 5.10 shows the calculated Coulomb stress evolution following the 1811-1812 events. In the upper crust, the maximum stress increases are near the NE and SW ends of the NMSZ fault zones. Conversely, stress decreases within the NMSZ fault zones and along a broad zone

extending roughly NNW-SSE across the NMSZ. This general pattern is similar to that in

Fig. 5.3.
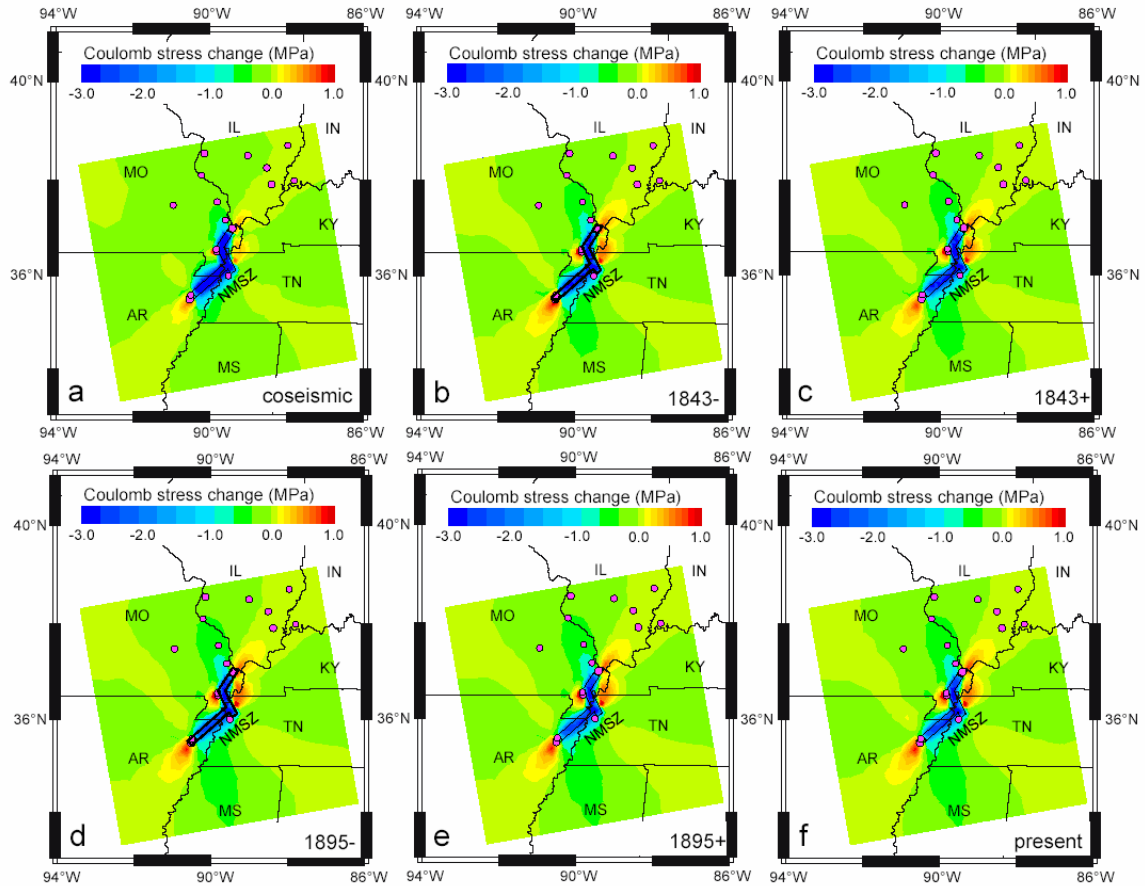
Figure 5.10 Predicted Coulomb stress evolution in the NMSZ and surrounding regions following the 1811-1812 large events. (a) coseismic; (b) before the 1843 Marked Tree, Arkansas, earthquake; (c) after the 1843 Marked Tree event; (d) before the 1895 Charleston, Missouri, earthquake, (e) after the 1895 Charleston event. (f) at present. The red dots are the epicenters of the major events (M>5) since 1812 [*Stover and Coffman*, 1993].

Each of the large 1811-1812 events was followed by numerous large aftershocks

(M>6.0) [*Johnston and Schweig*, 1996], and since 1812 a dozen or so moderate sized

events (M>5) occurred in the NMSZ and surrounding regions (Fig. 5.9). Although not all

these events were included in the calculation, their effects are likely minor in terms of energy release. This can be seen from the stress perturbation by two of the largest earthquakes in the NMSZ region since 1812: the 1895 Charleston, Missouri earthquake (M=5.9) and the 1843 Marked Tree, Arkansas earthquake (M=6.0) [*Stover and Coffman*, 1993] (Fig. 5.10). The results show some local stress changes near the epicenters of these events, but the general stress pattern remains dominated by the 1811-1812 large events, leaving the NMSZ in a stress shadow where stress has not reached the pre-1811-1812 level. The largest Coulomb stress increases are in southern Illinois and eastern Arkansas. Interestingly, these are where many of the major earthquakes (M>5) since 1812 have occurred (Fig. 5.10). The spatial correlation is not perfect, because seismicity is controlled by both stress and crustal strength; but the lateral variations of strength in the ambient crust are not included in the model. Thus the clustering of moderate earthquakes in southern Illinois and western Indiana may be attributed to both the increased Coulomb stress and the relatively weak crust in the Wabash Valley seismic zone, and seismicity near the Missouri-Illinois bounder, where the Coulomb stress actually decreased following the 1811-1812 large events, may indicate weakness in both crust and the uppermost mantle (see below). If one of the 1811-1812 main shocks occurred outside of the NMSZ, as suggested by Mueller et al. [2004] and Hough et al. [2005], the predicted stress field may differ somewhat from that in Fig. 5.10.

The predicted stress evolution is consistent with seismic energy release in the NMSZ and surrounding regions following the 1811 -1812 large events. Fig. 5.11a shows the calculated seismic energy release based on historic and modern earthquake data from the National Earthquake Information Center (NEIC) catalog

77

(http://neic.usgs.gov/neis/epic/epic.html). We used the Gutenberg-Richter formula [*Lay and Wallace*, 1995], and approximated all magnitudes as M_s. The spatial pattern is dominated by a dozen moderate sized events (M>5) since 1812, especially the two M~6 events near the NE and SW tips of the NMSZ (Fig. 5.9). Fig. 5.11b shows the excess strain energy, calculated by assigning a strain change in each element, if needed, to bring the deviatoric stress below the yield strength of the crust during a time step. A vertical integration of the product of such strain changes and stress gives the total excess strain energy accumulated over a single time step at a given place. The spatial pattern of the
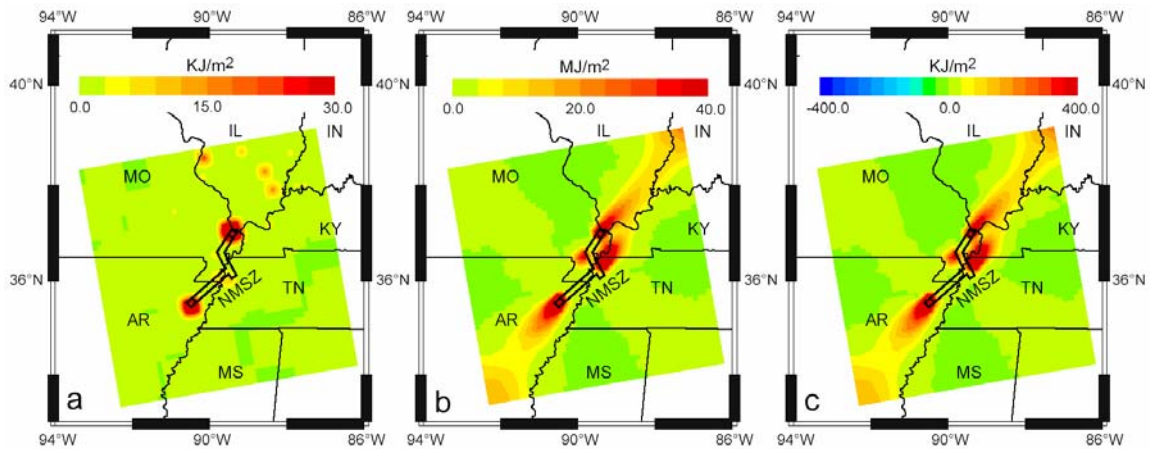
Figure 5.11 (a) Estimated seismic energy release in the NMSZ and surrounding regions since 1812. (b) Predicted total excess strain energy since the 1811-1812 events. (c) Predicted seismic strain energy in the crust today available for producing earthquakes, assuming 10% of the total excess strain energy will be released in future earthquakes.

calculated excess strain energy is consistent with the seismic energy release in the past two centuries (Fig. 5.11a), but the magnitude of the excess strain energy is two to three orders higher, presumably because not all energy has been released via earthquakes. The relation between strain energy before the large earthquakes, the energy released during them, and

the fraction of energy radiated as seismic waves remains unclear [*Kanamori*, 1978]. It is possible that the fraction of the energy release radiated as seismic waves (seismic efficiency) is only ~10% [*Lockner and Okubo*, 1983]. Multiplying the estimated seismic energy release (Fig. 5.11a) by a factor of 10 provides an estimate of total energy released by earthquakes. Subtracting it from the excess strain energy in Fig. 5.11b gives the residual strain energy, some of which may be released by future earthquakes. The partition between seismic and aseismic energy release is uncertain, estimations range from 2% to 80% [*Ward*, 1998]. Fig. 5.11c shows the estimated seismic energy in the NMSZ region assuming 10% of the total excess strain energy will be released in future earthquakes. This energy is capable of producing a number of Mw 6-7 earthquakes in southern Illinois and eastern Arkansas.

The basic mechanics illustrated by the simple model of intraplate seismic zones (Fig. 5.2a) thus appear to apply to the NMSZ. Without some kind of local loading, the NMSZ fault zone is expected to remain in a stress shadow today, and the repetition of large earthquakes within the NMSZ fault zones would be unlikely in the next few hundred years. On the other hand, much of the strain energy released by the 1811-1812 events has migrated to southern Illinois and eastern Arkansas, where a number of moderate earthquakes have occurred since 1812. Based on this model, the residual strain energy in these regions, even without additional contribution from local loading, is capable of producing damaging earthquakes.

5.4 Lithospheric Structure and Seismicity in the CEUS

So far our discussion of intraplate earthquakes has focused on postseismic evolution

after a large earthquake. Given the low strain rates in the CEUS and most other stable

continents, it remains unclear what caused these large earthquakes in the first place. It has

been suggested that that most intraplate earthquakes, especially the large events (Mw>6.0),

occur in ancient rift zones [*Johnston and Kanter*, 1990]. This is true for the NMSZ, which

is within the Mesozoic Reelfoot rift system [*Ervin and McGinnis*, 1975]. Most hypotheses

of local loading mechanisms responsible for the large earthquakes in the NMSZ are based

on inferred properties of the rift, including the sinking of an intrusive mafic body in the rift

[*Grana and Richardson*, 1996; *Pollitz et al.*, 2001a], detachment faulting at the base of the

rifts [*Stuart et al.*, 1997], and an unspecified sudden weakening of the lower crust [*Kenner

and Segall*, 2000]. However, Fig. 5.12 shows that not all seismic zones in the CEUS are

associated with rifts, and not all rifts are seismically active. One notable example is the

Mid-Continent Rift, one of the most prominent rift systems in the CEUS that has been

essentially aseismic in historic times. On the other hand, earthquakes in the CEUS appear

to concentrate along the margins of the seismologically inferred North American craton, or

the "tectosphere" [*Jordan*, 1979] defined by the abnormally thick lithosphere.

5.4.1 Stress field in the CEUS

Could the lithosphere-tectosphere transition zone concentrate stresses and thus

contribute to seismicity in the CEUS? To address this question, we developed a finite

element model for the CEUS (Fig. 5.13). To simulate the long-term stress pattern, we treat

the lithosphere as a power-law fluid continuum with a relative high viscosity (10^{24} Pa s),

underlain by a viscous asthenosphere with a lower viscosity of 10^{21} Pa s. The thickness of

the model lithosphere is based on seismologically derived thermal lithosphere thickness

[*Goes and van der Lee*, 2002]. The bottom of the model domain is a free slip boundary. The

model domain is loaded on both sides by a 30 MPa compressive stress oriented N60ºE, the direction of maximum tectonic compression for the CEUS [*Zoback and Zoback*, 1989]. The calculated Coulomb stress is concentrated in the zones of relatively thin lithosphere, around the margin of the North American tectosphere and under the Mississippi embayment (Fig. 5.14). The regions of high Coulomb stress show a strong spatial correlation with seismic zones in the CEUS, suggesting that the lateral heterogeneity of lithospheric structures is an important factor for seismicity in the CEUS.
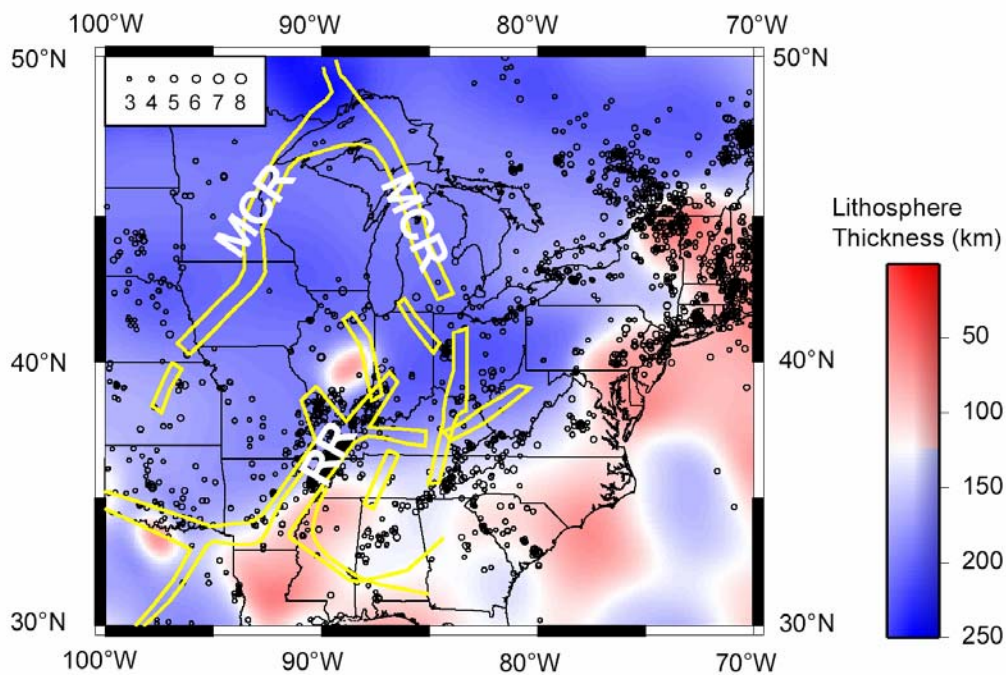
Figure 5.12 Thermal lithospheric thickness [*Goes and van der Lee*, 2002] and seismicity (1800-2004) in the CEUS. Yellow lines show the rift zones. MCR: Middle Continental Rift; RR: Reelfoot Rift.
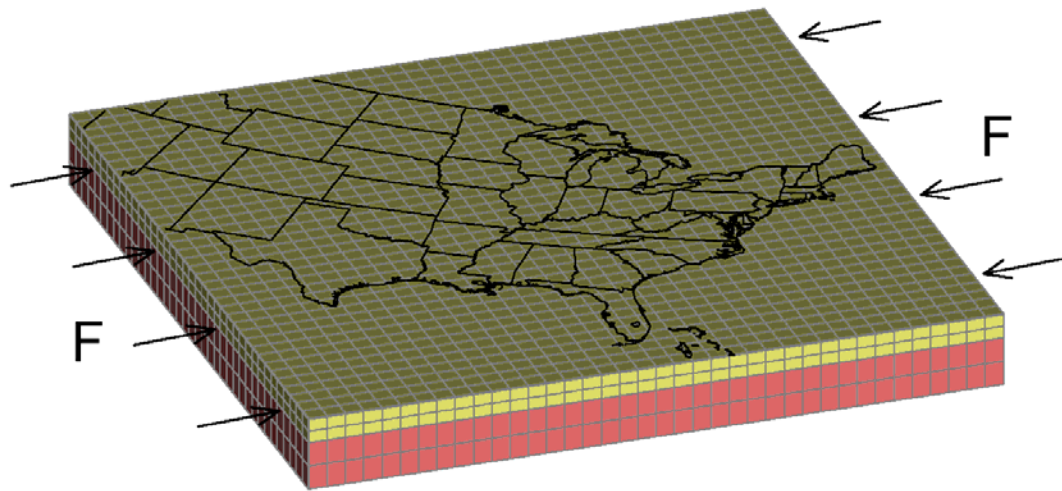
Figure 5.13 Finite element model for calculating long-term stresses in the CEUS. See text for detail.
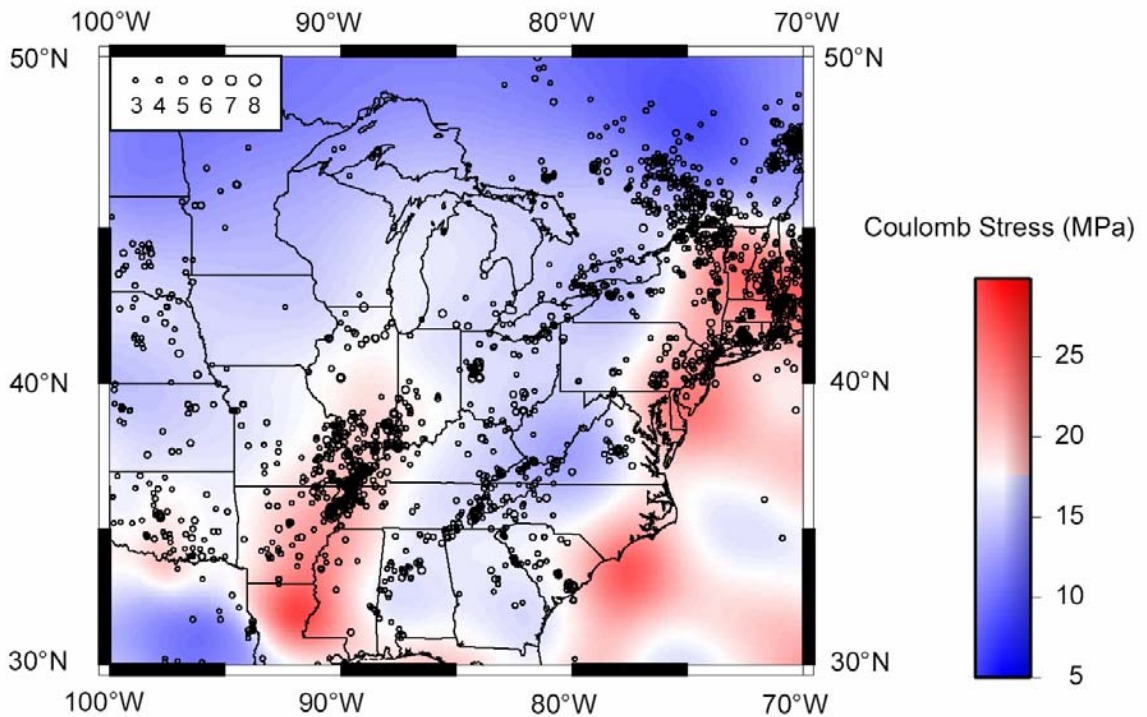
Figure 5.14 Calculated optimal Coulomb stress. Note the spatial correlation   between seismicity and regions of high Coulomb stresse in the CEUS.

5.4.2 Pn tomography of CEUS

The calculated high Coulomb stress in the Mississippi embayment results from relatively thin lithosphere inferred from low Vs velocities [*Goes and van der Lee*, 2002] (Fig. 5.12), which relate to heat flow anomalies in the NMSZ region [*Liu and Zoback*, 1997]. To refine the uppermost mantle velocity structure beneath the central and eastern U.S., we have derived a preliminary Pn velocity map (Fig. 5.15). Pn is a leaky mode guided wave that travels primarily through the uppermost mantle and is therefore most sensitive to seismic velocity fluctuations there. Pn tomography has become a common method to explore the lithospheric mantle velocity structure [*Hearn et al.*, 1994]. This method commonly uses a least squares algorithm [*Paige and Saunders*, 1982] to iteratively solve for all event-station pairs to obtain slowness, anisotropy, and station and event delays. The method includes damping parameters on both velocity and anisotropy to regularize the solution and reduce noise artifacts. P-wave travel time residuals (<10 s) from sources at 1.8° to 15° are inverted for uppermost mantle velocity. A straight line fit for the initial travel time residuals versus distance gives an apparent Pn velocity of 8 km/s for the study area.

To map the Pn velocity structure in the CEUS, we collected approximately 11,900 Pn travel times from ISC, NEIC, and 750 handpicked arrivals from both permanent and temporary stations throughout the CEUS. To compensate for the relatively small numbers of ray paths, we used a relatively large cell size in our model parameterization (0.5°x 0.5°). Overall we have a relatively high density of ray paths within the active seismic zones in the CEUS and lower ray coverage in much of the shield portions of the North American plate (Fig. 5.15a).
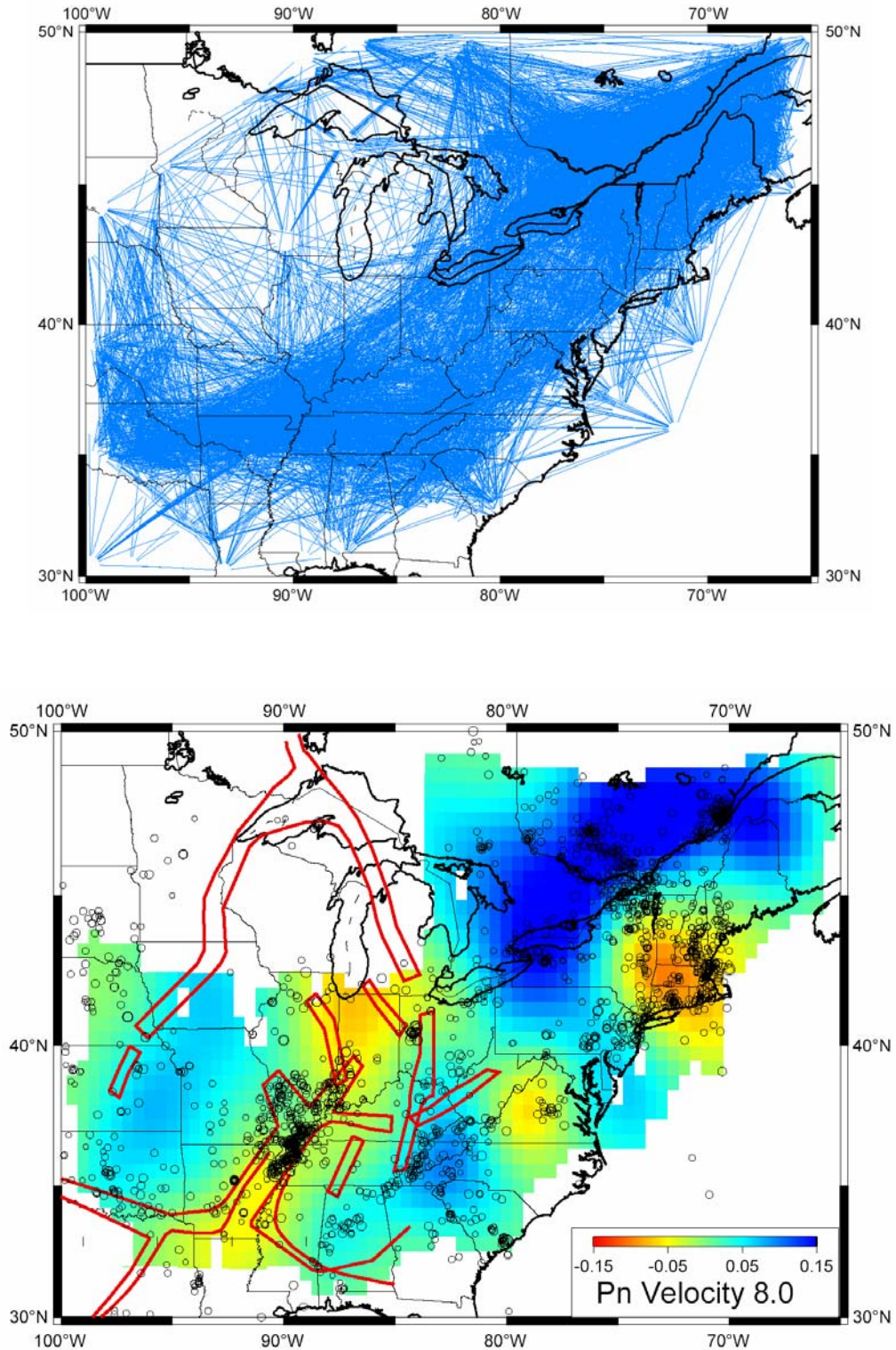
Figure 5.15 (a) Ray coverage for Pn paths between 2 and 15 degrees distance in the CEUS. Approximately 11,900 ray paths are used in the model. (b) Preliminary Pn tomographic map for the CEUS. Black circles are the same earthquake epicenters shown in Fig. 5.9.

We found a first order agreement between the NA00 model [*Goes and van der Lee*, 2002] and our Pn tomographic velocity model. However, we also observed interesting small scale heterogeneity, such as the surprising low velocities beneath the central Appalachians and Adirondack mountains along the eastern coast of North America (Fig. 5.15b). The velocities within the Mississippi Embayment and at the eastern margin of the Eastern Tennessee Seismic Zone (ETSZ) are relatively slow (~7.9 km/s). The lithospheric mantle velocities within the North American shield are consistent with the high S-wave velocities measured at 100 km depth. Our results also show relatively low velocities (~7.9 km/s) beneath the Illinois Basin.

The primary difference between our P-wave velocity measurements and the surface wave velocities [*Goes and van der Lee*, 2002] are in the southern Appalachians. Specifically, near the ETSZ we found a region of relatively high velocity that is not apparent in the NA00 model. A viscosity contrast and hence a change of lithospheric mantle properties here may concentrate stress and thus help to explain the ETSZ seismicity.

5.5 Discussion

One major result from this study is that the strain energy inherited from large intraplate earthquakes may dominate the local strain energy budget for hundreds to thousands of years. This result is expected, given the generally low strain rates in stable continents including the North American plate interior [*Dixon et al.*, 1996; *Gan and Prescott*, 2001]. Applied to the NMSZ, we have shown that the predicted spatial pattern and values of the stress and strain energy buildup following the 1811-1812 large events may explain the

occurrence of many moderate sized earthquakes in areas surrounding the NMSZ since 1812. Some of these events may be viewed as aftershocks, as slow loading usually causes a long duration of aftershocks [*Stein and Newman*, 2004]. Many of these events occurred outside the NMSZ and were triggered or even directly produced (in terms of energy source) by the main events. Furthermore, we have shown that, after large earthquakes, intraplate seismic zones tend to stay in a stress shadow where full stress restoration may take thousands of years, longer than predictions based solely on regional strain rate estimates. This is because seismic zones within a stable continent are of finite length, surrounded by relatively strong crust. As long as deviatoric stresses are supported by the ambient crust, little stress is available to reload the fault zones. This result is consistent with geodetic measurements in the NMSZ and surrounding regions that show the current strain rates are very slow (0 ± 2 mm/yr) [*Gan and Prescott*, 2001; *Newman et al.*, 1999], rather than 5-8 mm/yr reported earlier [*Liu et al.*, 1992]. More recent GPS data confirm the low strain rate around the NMSZ [*Smalley et al.*, 2005a]; whether or not higher strain rates within the fault zone can be detected from present GPS data is debatable [*Calais et al.*, 2005; *Smalley et al.*, 2005b].

These results do not contradict the present rate of seismicity in the NMSZ. Although thousands of events have been recorded in the NMSZ in recent decades, most are small (M<4) and thus release little energy. No major (M>5) events have occurred within the NMSZ fault zone since 1812, and the two largest events in the past two centuries, the 1895 Charleston, Missouri earthquake (M=5.9) and the 1843 Marked Tree, Arkansas earthquake (M=6.0), occurred near the tip of the inferred NMSZ fault zones, consistent with the model prediction.

However, the model results are inconsistent with paleoseismic data indicating that at least two more events similar to the 1811-1812 large events occurred in the NMSZ, around AD 900 and 1400 [*Kelson et al.*, 1996; *Tuttle et al.*, 2002]. Given the difficulties in determining the size and location of paleoearthquakes from liquefaction data, it is not surprising that some conclusions drawn from paleoseismic data were questioned. Newman et al. [*Newman et al.*, 1999], for instance, argued that the size of these paleoevents may be overestimated – these may be M~7, rather than M~8, events, more in line with the new estimates for the 1811-1812 events [*Hough et al.*, 2000]. However, our model shows that it is difficult even for M~7 events to repeat in the NMSZ fault zone every few hundred years. Thus explaining paleoseismic data requires local loading. Various local loading mechanisms have been proposed, including sinking of a "mafic pillow" within the Reelfoot rift [*Grana and Richardson*, 1996; *Pollitz et al.*, 2001a]. We have avoided including these models in our calculations because of large uncertainties of these models. Because seismic activity in the NMSZ likely started in the Holocene [*Pratt*, 1994; *Schweig and Ellis*, 1994; *Van Arsdale*, 2000], any local loading mechanism must also explain why it started in the Holocene. Stress triggering associated with glacial isostatic adjustment (GIA) provides some interesting possible causes. James and Bent [1994] and Wu and Johnston [2000] concluded that GIA may be significant for seismicity in the St. Lawrence valley but not for the more distant NMSZ, because GIA predicts predominately thrust faulting in the NMSZ, not strike-slip faulting as expected, and the stress change is too small (0.01 MPa). Hough et al. [2000] suggest that the main mechanism in the NMSZ is actually reverse faulting. Grollimund and Zoback [2001] show that GIA could have caused   three orders of seismic strain rate increase in the vicinity of the New Madrid by suggesting a weak zone there.

Refined imaging of crustal and lithospheric structures under the NMSZ and other seismic zones in the CEUS would help to test potential local loading mechanisms.

The stress field in the CEUS is characterized by a nearly horizontal, NE to E-striking axis of maximum compressive stress [*Herrmann*, 1979; *Sbar and Sykes*, 1973; *Zoback and Zoback*, 1989]. The uniformity of stress-tensor orientation over a broad area of the CEUS suggests that the stress field arises from forces that drive or resist plate motions [*Richardson and Solomon*, 1979; *Zoback and Zoback*, 1989]. Given the rather uniform far-field stresses and the stability of the plate interior, crustal weakness, often found in ancient rift zones, is commonly related to intraplate earthquakes [*Johnston and Kanter*, 1990; *Johnston and Schweig*, 1996]. This seems true in the central US, especially in the Mississippi embayment (Fig. 5.12), but not in the eastern US, where seismic zones seem spatially associated with ancient faults developed when the eastern United States was near plate boundaries [*Dewey et al.*, 1989], or faults that may be related to transform fracture zones in the Atlantic ocean floor [*Sykes*, 1978]. Whereas these seismic zones may be associated with different structural causes, we suggest that there may be a common and deep cause for most of the seismicity in the CEUS: the transition zone between the thick North American tectosphere and the surrounding lithosphere. Our calculations show that such lateral heterogeneity of lithospheric structure could concentrate stress near the margins of the tectosphere, and the predicted regions of high stresses have a strong correlation with seismicity in the CEUS. However, our regional model does not include lateral heterogeneity of crustal structure, which would further affect stress distribution and seismicity. Further testing of the causal relationship between lithospheric structures and seismicity must await more detailed crustal and lithospheric structures of the CEUS.

5.6 Conclusions

Our major conclusions are:

1. Intraplate seismic zones tend to remain in a Coulomb stress shadow for thousands of years following large earthquakes. The slow far-field tectonic loading rates and the relatively strong ambient crust make stress re-accumulation within intraplate fault zones difficult, unless there are some local loading mechanisms. On the other hand, a significant amount of the stress relieved from large intraplate earthquakes, and the associated strain energy, may migrate to and be trapped within the neighboring crust, mainly near the tips of the fault zones. Such inherited strain energy may dominate the strain energy budget in the intraplate fault zone and surrounding regions for hundreds to thousands of years, and can produce aftershocks hundreds of years after the main shocks. These behaviors are fundamentally different from interplate seismic zones, which are constantly loaded by plate motions.

2. The 1811-1812 large earthquakes in the NMSZ caused significant buildup of Coulomb stress and strain energy in the surrounding regions, mainly southern Illinois and eastern Arkansas. Many of the moderate sized earthquakes (M>5) in these regions since 1812 may have been triggered or facilitated by stress and strain energy inherited from the 1811-1812 large events. The residual strain energy from the 1811-1812 main shocks is capable of producing some damaging (M>6) earthquakes in areas surrounding the NMSZ today, even in the absence of local loading. Conversely, the NMSZ fault zones should remain in a stress shadow where thousands of years may be needed to restore the stress

to the pre-1811-1812 level. Thus, some local loading mechanism would be needed if numerous large events similar to the 1811-1812 events have occurred in the fault zones during the Holocene, as suggested by paleoseismic data. Although a number of local loading mechanisms have been proposed, more studies, including refined imaging of the crustal and lithospheric structures in the NMSZ region, are needed to test these hypotheses.

3. Seismicity in the CEUS shows a strong spatial correlation with the margins of the North American tectosphere, consistent with our model prediction of high Coulomb stress in the tectosphere-lithosphere transition zones. In the NMSZ, the seismicity seems to be related to an abnormally thin lithosphere under the Mississippi embayment. Again, further imaging of the crustal and lithospheric structure will help to address the cause of seismicity in the NMSZ and other seismic zones in the CEUS.

5.7 Acknowledgements

5.8 References

Anderson, J.G., Seismic strain rates in the central and eastern United States, *Seismo. Soc. Am. Bull.*, *76* (1), 273-290, 1986.

Becker, T.W., J.L. Hardebeck, and G. Anderson, Constraints on fault slip rates of the southern California plate boundary from GPS velocity and stress inversions, *Geophys. J. Int.*, *160*, 634-650, 2005.

Bennett, R.A., A.M. Friedrich, and K.P. Furlong, Codependent histories of the San Andreas and San Jacinto fault zones from inversion of fault displacement rates, *Geology*, *32*, 961-964, 2004.

Calais, E., G. Mattioli, C. Demets, J.M. Nocquet, S. Stein, A. Newman, and P. Rydelek, Tectonic strain in plate interiors?, *Nature*, *438*, E9-E10, 2005.

Chiu, J.M., A.C. Johnston, and Y.T. Yang, Imaging the active faults of the central New Madrid seismic zone using PANDA array data, *Seismol. Res. Lett.*, *63* (3), 375-393, 1992.

Dewey, J.W., D.P. Hill, W.L. Ellsworth, and E.R. Engdahl, Earthquakes, faults, and the seismotectonic framework of the contiguous United States, in *Geophysical Framework of the Continental United States*, edited by L.C. Pakiser, and W.D. Mooney, pp. 541-576, GSA, Boulder, CO, 1989.

Diment, W.H., T.C. Urban, and F.A. Revetta, Some geophysical anomalies in the eastern United States, in *The Nature of the Solid Earth*, edited by E.C. Robertson, pp. 544-572, McGraw-Hill Book Co., New York, 1972.

Dixon, T.H., A. Mao, and S. Stein, How rigid is the stable interior of the North American plate?, *Geophys. Res. Lett.*, *23* (21), 3035-3038, 1996.

Ervin, C.P., and L.D. McGinnis, Reelfoot Rift; reactivated precursor to the Mississippi Embayment, *Geol. Soc. Am. Bull.*, *86* (9), 1287-1295, 1975.

Freed, A.M., and J. Lin, Delayed triggering of the 1999 Hector Mine earthquake by viscoelastic stress transfer, *Nature*, *411* (6834), 180-183, 2001.

Gan, W., and W.H. Prescott, Crustal deformation rates in central and eastern U.S. inferred from GPS, *Geophys. Res. Lett.*, *28* (19), 3733-3736, 2001.

Goes, S., and S. van der Lee, Thermal structure of the North American uppermost mantle inferred from seismic tomography, *J. Geophys. Res.*, *107* (B3), 2050, doi:10.1029/2000JB000049, 2002.

Gomberg, J.S., Tectonic deformation in the New Madrid seismic zone; inferences from map view and cross-sectional boundary element models, *J. Geophys. Res.*, *98* (4), 6639-6664, 1993.

Grana, J.P., and R.M. Richardson, Tectonic stress within the New Madrid seismic zone, *J. Geophys. Res.*, *101* (3), 5445-5458, 1996.

Grollimund, B., and M.D. Zoback, Did deglaciation trigger intraplate seismicity in the New Madrid seismic zone?, *Geology*, *29* (2), 175-178, 2001.

Hearn, T.M., A.C. Rosca, and M.C. Fehler, Pn tomography beneath the southern Great Basin, *Geophys. Res. Lett.*, *21* (20), 2187-2190, 1994.

Herrmann, R.B., Surface wave focal mechanisms for eastern North American earthquakes with tectonic implications, *J. Geophys. Res.*, *84* (B7), 3543-3552, 1979.

Hildenbrand, T.G., and J.D. Hendricks, Geophysical setting of the Reelfoot Rift and relations between rift structures and the New Madrid seismic zone, *U.S. Geol. Surv. Prof. Pap.*, E1-E30, 1995.

Hough, S.E., J.G. Armbruster, L. Seeber, and J.F. Hough, On the modified Mercalli intensities and magnitudes of the 1811-1812 New Madrid earthquakes, *J. Geophys. Res.*, *105* (10), 23,839-23,864, 2000.

Hough, S.E., R. Bilham, K. Mueller, W. Stephenson, R. Williams, and J. Odum, Wagon Loads of Sand Blows in White County, Illinois, *Seismol. Res. Lett.*, *76* (3), 373-386, 2005.

James, T.S., and A.L. Bent, A comparison of eastern North American seismic strain-rates to glacial rebound strain-rates, *Geophys. Res. Lett.*, *21*, 2127-2130, 1994.

Johnston, A.C., Seismic moment assessment of earthquakes in stable continental regions; III, New Madrid 1811-1812, Charleston 1886 and Lisbon 1755, *Geophys. J. Int.*, *126* (2), 314-344, 1996.

Johnston, A.C., and L.R. Kanter, Earthquakes in stable continental crust, *Sci. Am.*, *262(3)*, 68-75, 1990.

Johnston, A.C., and E.S. Schweig, The enigma of the New Madrid earthquakes of 1811-1812, *Annu. Rev. Earth Planet. Sci.*, 1996.

Jordan, T.H., Mineralogies, densities and seismic velocities of garnet lherzolites and their geophysical implications, in *The mantle sample; inclusions in kimberlites and other volcanics; Proceedings of the Second international kimberlite conference; Volume 2*, Am. Geophys. Union, 1979.

Kanamori, H., Quantification of earthquakes, *Nature*, *271*, 411-414, 1978.
Kelson, K.I., G.D. Simpson, R.B. VanArsdale, C.C. Haraden, and W.R. Lettis, Multiple late Holocene earthquakes along the Reelfoot Fault, central New Madrid seismic zone, *J. Geophys. Res.*, *101* (3), 6151-6170, 1996.

Kenner, S.J., and P. Segall, A mechanical model for intraplate earthquakes; application to the New Madrid seismic zone, *Science*, *289* (5488), 2329-2332, 2000.

King, G.C.P., R.S. Stein, and J. Lin, Static stress changes and the triggering of earthquakes,

Bull. Seismol. Soc. Am., *84* (3), 935-953, 1994.

Lay, T., and T.C. Wallace, *Modern Global Seismology*, 383-385 pp., Academic Press, San Diego, 1995.

Li, Q., M. Liu, and A. Sandvol Eric, Stress Evolution Following the 1811-1812 Large Earthquakes in the New Madrid Seismic Zone, *Geophys. Res. Lett*, *32* (L11310), doi:10.1029/2004GL022133, 2005.

Lin, J., and R.S. Stein, Stress triggering in thrust and subduction earthquakes, and stress interaction between the southern San Andreas and nearby thrust and strike-slip faults, *J. Geophys. Res.*, *109* (B02303), doi:10. 1029/2003JB002607, 2004.

Liu, L., and M.D. Zoback, Lithospheric strength and intraplate seismicity in the New Madrid seismic zone, *Tectonics*, *16* (4), 585-595, 1997.

Liu, L., M.D. Zoback, and P. Segall, Rapid intraplate strain accumulation in the New Madrid seismic zone, *Science*, *257*, 1666-1669, 1992.

Lockner, D.A., and P.G. Okubo, Measurements of frictional heating in granite, *J. Geophys. Res.*, *88* (5), 4313-4320, 1983.

Mueller, K., S.E. Hough, and R. Bilham, Analysing the 1811-1812 New Madrid earthquakes with recent instrumentally recorded aftershocks, *Nature*, *429*, 284-288, 2004.

Mueller, K., and J. Pujol, Three-Dimensional Geometry of the Reelfoot Blind Thrust: Implications for Moment Release and Earthquake Magnitude in the New Madrid Seismic Zone, *Bull. Seism. Soc. Am.*, *91* (6), 1563-1573, 2001.

Newman, A., S. Stein, J. Weber, J. Engeln, A. Mao, and T. Dixon, Slow deformation and lower seismic hazard at the New Madrid Seismic Zone, *Science*, *284* (5414), 619-621, 1999.

Nuttli, O.W., G.A. Bollinger, and D.W. Griffiths, On the relation between modified Mercalli intensity and body-wave magnitude, *Bull. Seismol. Soc. Am.*, *69* (3), 893-909, 1979.

Obermeier, S.F., G.S. Gohn, R.E. Weems, R.L. Gelinas, and M. Rubin, Geologic evidence for recurrent moderate to large earthquakes near Charleston, South Carolina, *Science*, *227* (4685), 408-411, 1985.

Paige, C.C., and M.A. Saunders, LSQR: an algorithm for sparse linear equations and sparse least squares, *ACM Transactions on Mathematical Software (TOMS)*, *8* (1), 43-71, 1982.

Pollitz, F.F., L. Kellogg, and R. Buergmann, Sinking mafic body in a reactivated lower crust; a mechanism for stress concentration at the New Madrid seismic zone, *Bull. Seismol. Soc. Am.*, *91* (6), 1882-1897, 2001a.

Pollitz, F.F., C. Wicks, and W. Thatcher, Mantle flow beneath a continental strike-slip fault; postseismic deformation after the 1999 Hector Mine earthquake, *Science*, *293* (5536), 1814-1818, 2001b.

Pratt, T.L., How old is the New Madrid seismic zone?, *Seismol. Res. Lett.*, *65*, 172-179, 1994.

Richardson, R.M., and S.C. Solomon, Tectonic stress in the plates, *Rev. Geophys. Space Phys.*, *17* (5), 981-1019, 1979.

Rydelek, P.A., and I.S. Sacks, Migration of large earthquakes along the San Jacinto Fault; stress diffusion from 1857 Fort Tejon earthquake, *Geophys. Res. Lett.*, *28* (16), 3079-3082, 2001.

Sbar, M.L., and L.R. Sykes, Contemporary compressive stress and seismicity in eastern North America; an example of intra-plate tectonics, *Geol. Soc. Am. Bull.*, *84* (6), 1861-1881, 1973.

Schweig, E.S., and M.A. Ellis, Reconciling short recurrence intervals with minor deformation in the New Madrid seismic zone, *Science*, *264* (5163), 1308-1311, 1994.

Smalley, R., M.A. Ellis, J. Paul, and R.B. Van Arsdale, Space geodetic evidence for rapid strain rates in the New Madrid seismic zone of central USA, *Nature*, *435*, 1088-1090, 2005a.

Smalley, R., M.A. Ellis, J. Paul, and R.B. Van Arsdale, Tectonic strain in plate interiors? Reply, *Nature*, *438*, E10-E10, 2005b.

Stein, R.S., A.A. Barka, and J.H. Dieterich, Progressive failure on the North Anatolian fault since 1939 by earthquake stress triggering, *Geophys. J. Int.*, *128*, 594-604, 1997.

Stein, S., and A. Newman, Characteristic and Uncharacteristic Earthquakes as Possible Artifacts: Applications to the New Madrid and Wabash Seismic Zones, *Seis. Res. Lett.*, *75*, 173-187, 2004.

Stover, C.W., and J.L. Coffman, Seismicity of the United States, 1568-1989 (revised), *U.S. Geol. Surv. Prof. Pap.*, 418, 1993.

Street, R., and A. Lacroix, An empirical study of New England seismicity: 1727-1977, *Bull. Seismol. Soc. Am.*, *69* (1), 159-175, 1979.

Stuart, W.D., T.G. Hildenbrand, and R.W. Simpson, Stressing of the New Madrid seismic zone by a lower crust detachment fault, *J. Geophys. Res.*, *102* (12), 27,623-27,633, 1997.

Sykes, L.R., Intraplate seismicity, reactivation of preexisting zones of weakness, alkaline magmatism, and other tectonism postdating continental fragmentation, *Rev. Geophys. Space Phys.*, *16* (4), 621-688, 1978.

Talwani, P., and J. Cox, Paleoseismic evidence for recurrence of earthquakes near Charleston, South Carolina, *Science*, *229* (4711), 379-381, 1985.

Townend, J., and M.D. Zoback, How faulting keeps the crust strong, *Geology*, *28* (5), 399-402, 2000.

Turcotte, D.L., and G. Schubert, *Geodynamics: Applications of continuum physics to geological problems*, 450 pp., John Wiley & Sons, New York, 1982.

Tuttle, M.P., E.S. Schweig, J.D. Sims, R.H. Lafferty, L.W. Wolf, and M.L. Haynes, The earthquake potential of the New Madrid seismic zone, *Bull. Seismol. Soc. Am.*, *92* (6), 2080-2089, 2002.

Van Arsdale, R., Displacement history and slip rate on the Reelfoot Fault of the New Madrid seismic zone, *Engineering Geology*, *55* (4), 219-226, 2000.

Ward, S.N., On the consistency of earthquake moment rates, geological fault data, and space geodetic strain; the United States, *Geophys. J. Int.*, *134* (1), 172-186, 1998.

Wu, P., and P. Johnston, Can deglaciation trigger earthquakes in N. America?, *Geophys. Res. Lett.*, *27* (9), 1323-1326, 2000.

Zoback, M.D., J. Townend, and B. Grollimund, Steady-state failure equilibrium and deformation of intraplate lithosphere, *Int. Geology Rev.*, *44* (5), 383-401, 2002.

Zoback, M.L., and M.D. Zoback, Tectonic stress field of the continental United States, in *Geophysical framework of the continental United States*, edited by L.C. Pakiser, and   W.D. Mooney, pp. 523-539, Geological Society of America (GSA), Boulder, CO, United States, 1989.

Chapter 6   GEOMETRICAL IMPACT OF THE SAN ANDREAS FAULT ON STRESS AND SEISMICITY IN CALIFORNIA

Qingsong Li and Mian Liu

Abstract. Most large earthquakes in northern and central California clustered along the main trace of the San Andreas Fault (SAF), the North American-Pacific plate boundary. However, in southern California earthquakes were rather scattered. Here we suggest that such along-strike variation of seismicity may largely reflect the geometrical impact of the SAF. Using a dynamic finite element model that includes the first-order geometric features of the SAF, we show that strain partitioning and crustal deformation in California are closely related to the geometry of the SAF. In particular, the Big Bend is shown to reduce slip rate on southern SAF and cause high shear stress and strain energy over a broad region in southern California, and a belt of high strain energy in the Eastern California Shear Zone.

6.1 Introduction

As the plate boundary, the San Andreas Fault (SAF) accommodates a large portion of the ~49 mm/yr relative motion between the Pacific and North American plates [*Bennett et al.*, 1996; *DeMets et al.*, 1994; *Meade and Hager*, 2005] and hosts many of the large

earthquakes in California (Fig. 6.1). However, both slip rate and seismicity show large

along-strike variations. In northern and central California, up to ~34 mm/yr of the plate

motion is accommodated by the SAF and some of the closely subparallel faults
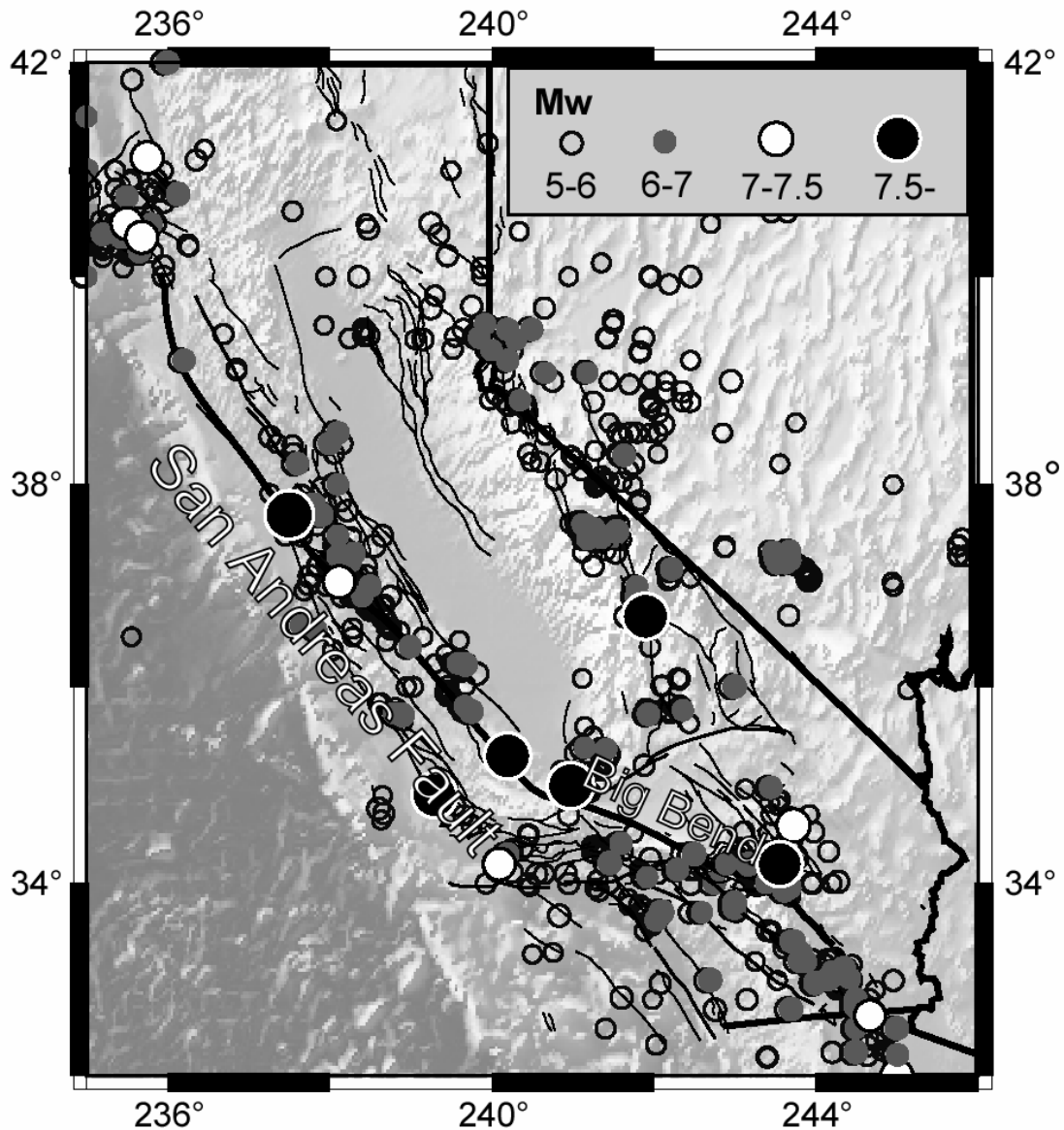

Figure 6.1 Topographic relief and seismicity in California and surrounding regions. Data of seismicity (includes M>5.0 earthquakes from 1800 to present) are from the NEIC catalog.

[California Geological Survey, http://www.consrv.ca.gov/CGS/rghm/psha/index.htm, hereafter referred to as CGS]; most large earthquakes occurred on or clustered to the main trace of the SAF. However, in southern California the relative plate motion is distributed among a complex system of faults. Slip rate on the main-trace of the SAF drops to 24-25 mm/yr [CGS]. Recent estimates based on GPS and seismicity [*Becker et al.*, 2005] indicate low slip rate on the Big Bend segments of the SAF: 15.7±12 mm/yr for the Mojave segment, 11±12 (combined normal and strike-slip components) for the San Bernardino Mountains segment. Seismicity in southern California is much diffuse, with many of the large earthquakes occurred off the main-trace of the SAF.

Although along-strike variations of seismicity and slip rate may have numerous causes, such as stressing rate [*Parsons*, 2006] and distribution and properties of active secondary faults [*Bird and Kong*, 1994], a particularly important cause may be the geometry of the SAF, especially the Big Bend, a ~25° counterclockwise bending in southern California (Fig. 6.1). Numerous studies have suggested that a non-planar fault geometry may have significant impact on fault slip, stress, and deformation in surrounding regions [*Du and Aydin*, 1996; *Duan and Oglesby*, 2005; *Fialko et al.*, 2005; *Fitzenz and Miller*, 2004; *Griffith and Cooke*, 2005; *Smith and Sandwell*, 2003; *Williams and Richardson*, 1991]. However, many of these studies were either based on two-dimensional models or with oversimplified fault geometry. Some are kinematic models with prescribed slip rates [*Smith and Sandwell*, 2003; *Williams and Richardson*, 1991], thus the effect of fault geometry on slip rates cannot be directly tested. In previous dynamic models [*Du and Aydin*, 1996; *Duan and Oglesby*, 2005; *Fitzenz and Miller*, 2004], fault slip rates were not explicitly calculated. Furthermore, most studies have focused on the fault zone; the

anelastic deformation outside the fault zone, hence the effects of fault geometry on off-main-trace seismicity, remain to be explored.

In this study, we developed a three-dimensional dynamic finite element model to investigate how the particular geometry of the SAF may have impacted on long-term fault slip, stress pattern, and seismicity in California.

6.2 Model Description

The finite element model encompasses most of California and the entire length of the SAF with realistic first-order features of the surface-trace geometry (Fig. 6.2). A 300-km wide extra model domain is added to both ends of the SAF to minimize artificial boundary effects. The model includes a 20-km thick upper crust with an elasto-plastic rheology (non-associated Drucker-Prager model), and a 40-km thick viscoelastic (Maxwell model) layer representing both the lower crust and the uppermost mantle. Viscosity for the lower crust and upper mantle between 1019 Pa s and 1021 Pa s [*Hager*, 1991; *Kenner and Segall*, 2000; *Pollitz et al.*, 2001] are explored. For both crust and mantle, the Young's Modulus is 8.75×1010 N/m^2 and the Poisson's ratio is 0.25. The SAF has a cohesion of 10 MPa, which is close to the upper bound permitted by heat flow data [*Lachenbruch and Sass*, 1980], and an effective frictional coefficient of 0. Outside the fault zone, the upper crust is relatively strong, with a cohesion of 50 MPa and effective frictional coefficient of 0.4.

The model SAF has a uniform dip angle of 90°. It is simulated with a 4-km thick layer of special fault elements, which deform plastically when reaching the yield criterion. This process simulates relative crustal motion across the fault zone. We developed the finite element codes based on a commercial FE package (www.fegensoft.com) [*Li et al.*, 2005],

and run the model on a 16-nodes PC cluster.
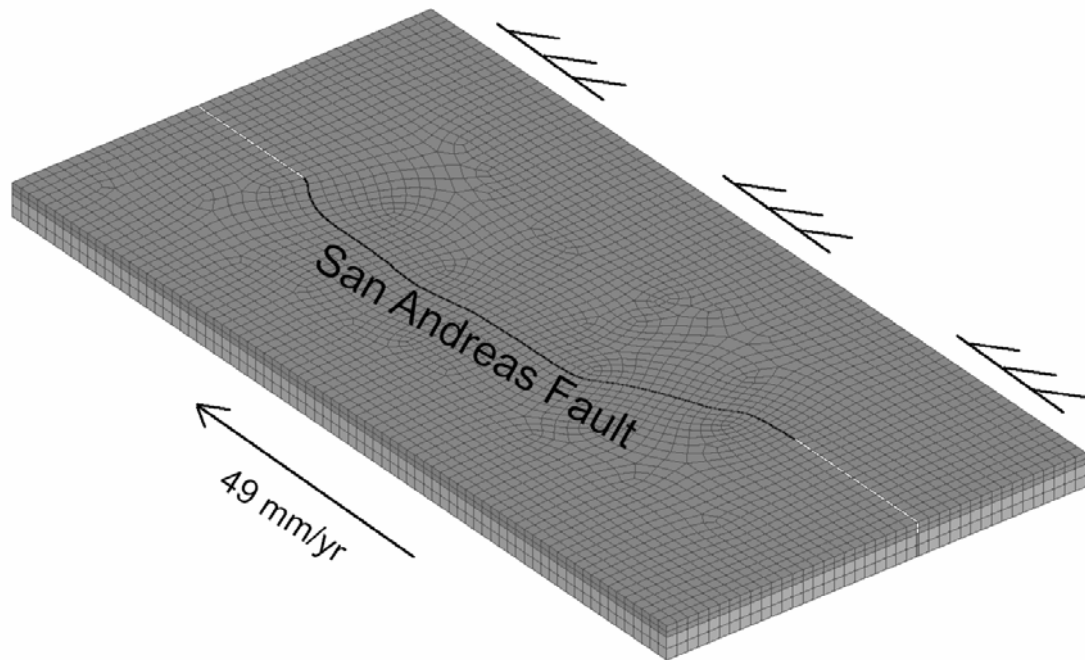
Figure 6.2 Numerical mesh and boundary conditions of the finite element model. The entire San Andreas Fault (black line) is explicitly included in the model.

The eastern side of the model domain is fixed, while the western side is loaded by a shear velocity of 49 mm/yr representing relative motion between the Pacific and the North American plates. Stress evolution is calculated at ten-year time steps. To minimize effects of artificial initial stress, the model is run till it reaches a steady state, which reflects the long-term slip on the SAF owing to tectonic loading from plate motion. We then calculated stress evolution over a period of tens of thousands of years with continuous tectonic loading. Over this time scale, the SAF creeps continuously. This is a long-term approximation of repeated rupture and locking on the SAF over shorter timescales. Outside the fault zone, excess stress over the yield strength is released by plastic

deformation.
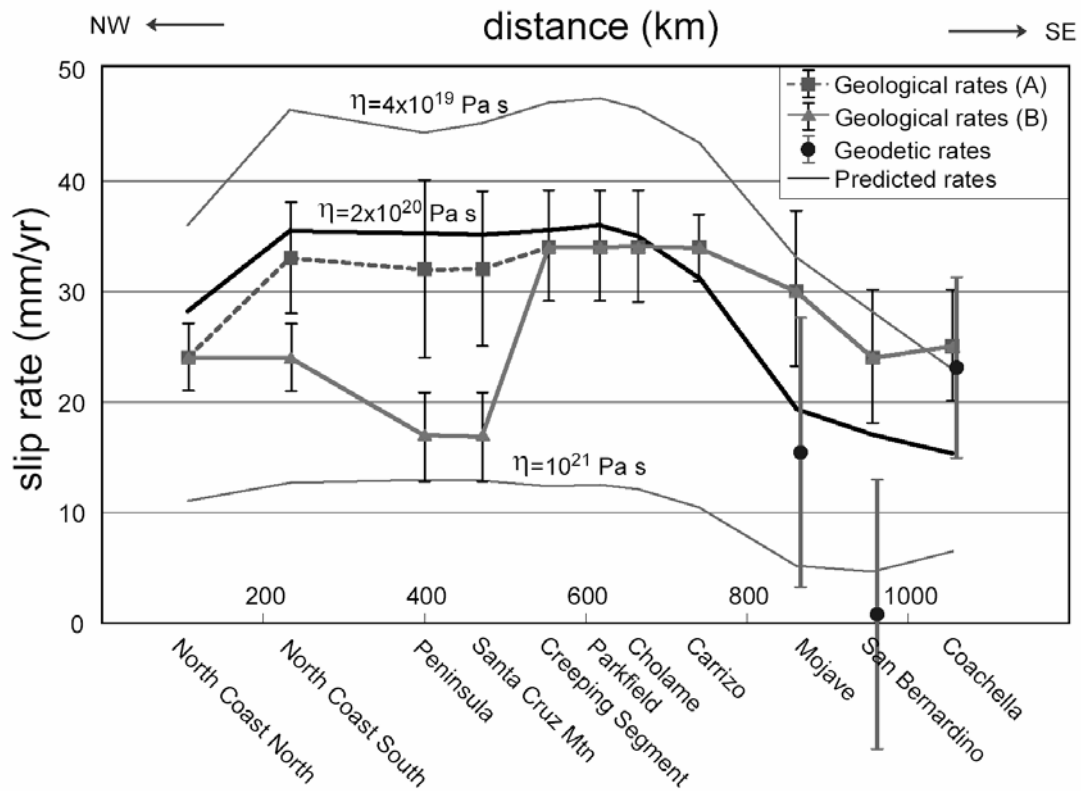
Figure 6.3 Comparison of the predicted slip rates (curves marked by viscosity values of the lower crust and upper mantle) and geological and geodetic slip rates (lines with error bars) along the SAF. Geological slip rates are from California Geological Survey [http://www.consrv.ca.gov/CGS/rghm/psha/index.htm]. Geological Rates A shows the sum of slip rates on several subparallel faults in northern California. Geological Rates B shows slip rates on the SAF main trace alone. Geodetic slip rates are from Becker et al. [2005].

6.3 Model Results

6.3.1 Slip rates on the SAF

Although slip rates along the SAF remain somewhat uncertain [CGS; *Becker et al.,*

2005; *Meade and Hager*, 2005], the general along-strike variations are clear (Fig. 6.3). The central segments of the SAF have the highest geological slip rates (~34 mm/yr). Slip rate on the northern segments of the SAF are lower (17-24 mm/yr) because some of the slip is taken up by the closely subparallel faults (the Rodgers Creek Fault, the Hayward Fault, and the Calaveras Fault). Adding up slip rates on these faults brings the total rates to near 34 mm/yr. Over the Big Bend slip rate lowers significantly. The slip rate is ~16 mm/yr on the Mojave segment, and even lower on the San Bernardino segment, with ~15 mm/yr slip accommodated by the subparallel San Jacinto fault [*Becker et al.*, 2005].

The model results indicate that such along-strike variation of slip rate may be largely explained by the geometry of the SAF. The relatively straight traces of the northern and central segments of the SAF, all subparallel to the direction of relative plate motion, account for the relatively high slip rate on these segments. Conversely, the Big Bend is shown to significantly hamper fault slip. The absolute values of the predicted slip rates depend on the viscosity of the lower crust and uppermost mantle (Fig. 6.3). A value of 2×10^{20} Pa s provides a close fit for the northern and central segments of the SAF. For the southern segments of the SAF, the predicted slip rates are significantly lower than the geological value, but close to those inverted from GPS data [*Becker et al.*, 2005; *Meade and Hager*, 2005]. Incorporating the series of weak faults and spreading centers to the southeast of the Salton Sea would produce a higher and better-fitting slip rate on the southernmost SAF.

6.3.2 Shear stress and seismicity

Fig. 6.4 shows the predicted steady-state maximum shear stress ($|\sigma_1 - \sigma_3|/2$),

where σ_1 and σ_3 are first and third principle stress, respectively. In regions where the stress has reached the Drucker-Prager yield strength, the maximum shear stress is capped by the yield strength envelope: $\alpha I_1 + \sqrt{J_2'} - k = 0$, where I_1 and J_2' are first invariant and second deviatoric invariant of the stress tensor, respectively; α and k are parameters related to cohesion and effective coefficient of friction.

Fig

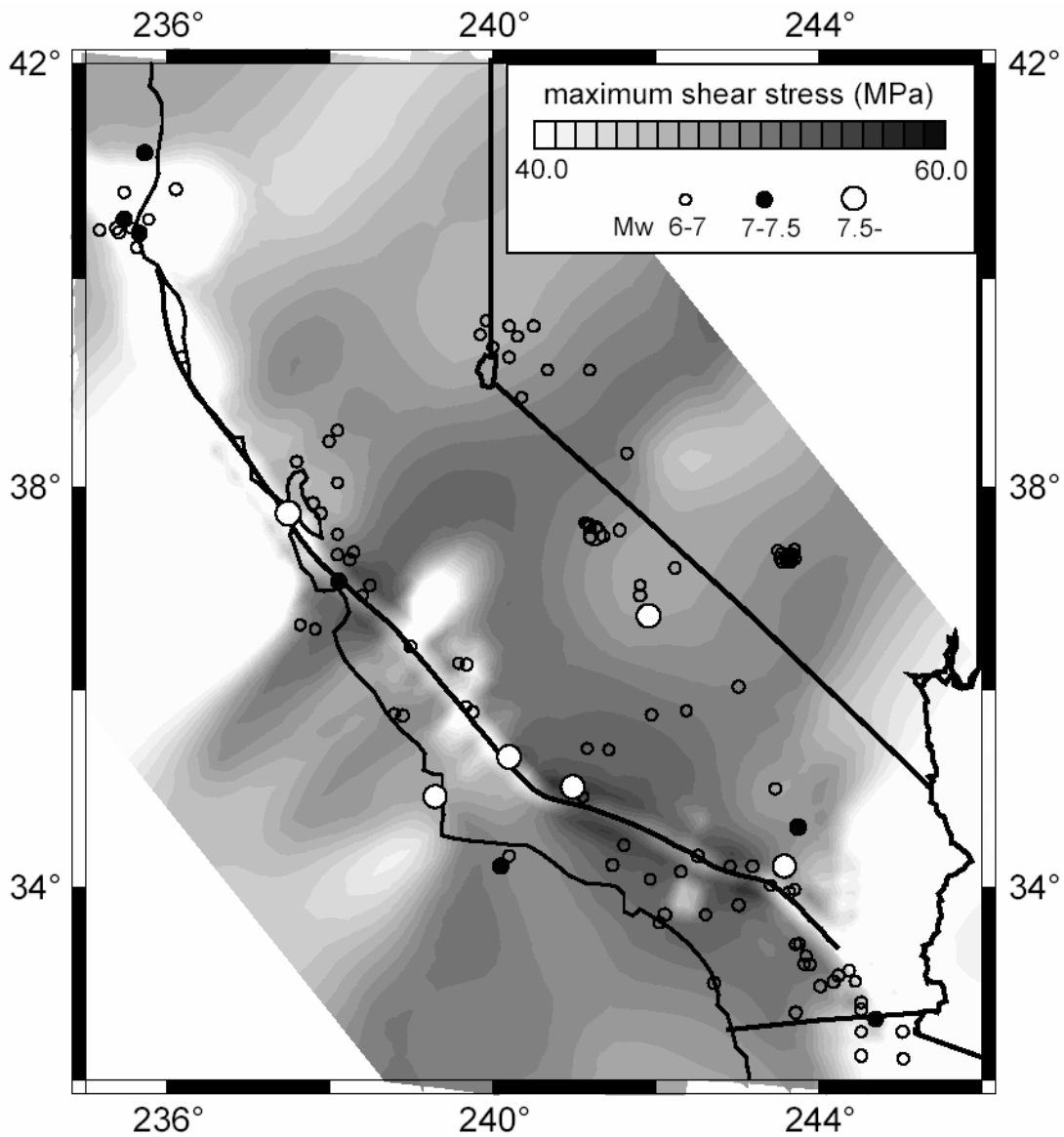**Figure 6.4** The predicted maximum shear stress (see text for definition). The dots show earthquakes (M>6.0) from 1800 to present (data from the NEIC catalog).

The most conspicuous feature in Fig. 6.4 is the broad area of high stress that spans over much of southern California where many of the large earthquakes occurred off the main-trace of the SAF. This is a direct consequence of the Big Bend. The small trans-compressive bending of the SAF south of the San Francisco Bay Area also causes a region of high stress, showing the sensitivity of stress field to fault geometry. The low shear stress around the northern part of the SAF results from the relatively straight SAF and a trans-extensional bend of the SAF near the Mendocino Triple Junction, which allows plastic deformation at lower shear stress. The low shear stress around the central SAF segments, which include the "creeping" section, arises solely from the relatively straight SAF. Assuming a weaker fault zone for the "creeping" section would further reduce the maximum shear stress in this part of the SAF.

6.3.3 Release of plastic strain energy outside the SAF

In this model plastic deformation occurs both within and outside the fault zone when stress reaches the yield criterion. Fig. 6.5 shows the predicted long-term rates of energy release outside the SAF, given by the product of stress tensor and the tensor of plastic strain necessary to absorb the excess stress. Again, the results indicate significant impact of the geometry of the SAF; each subtle bending of the SAF causes high plastic energy release in its surrounding. The Big Bend causes two elongated belts of high energy release. One is to the west of the SAF, coincides with the Palos Verdes Fault and the Coronado Bank Fault; the other coincides with the Eastern California Shear Zone (ECSZ). We have found that, if the San Jacinto fault, which absorbs a significant portion of the relative plate motion in southern California [*Bennett et al.*, 2004], is included in the model, the predicted energy
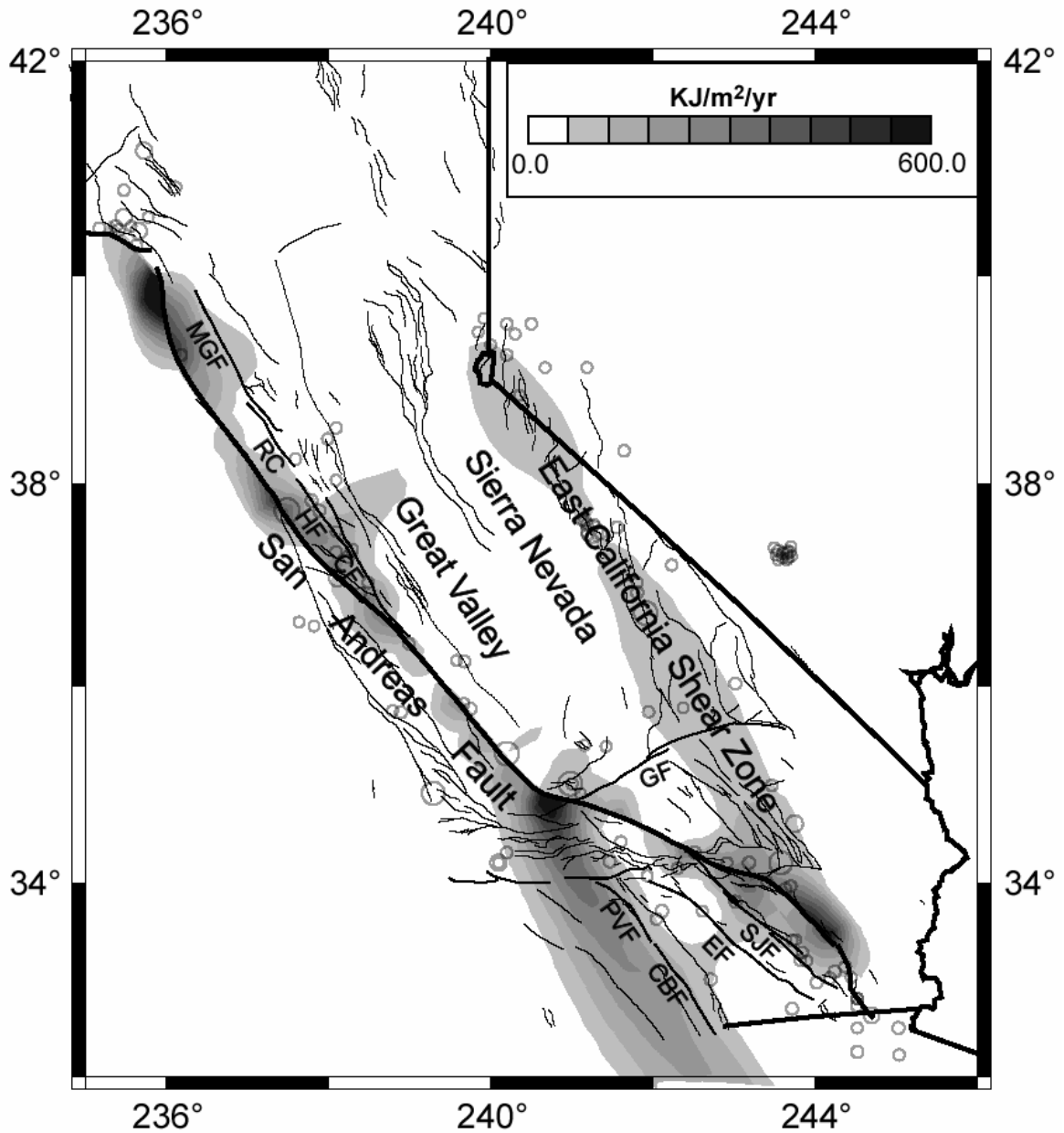
Figure 6.5 The predicted plastic energy release off the SAF main trace. The energy release is vertically integrated through the upper crust per unit surface area. The areas of high energy release coincide with many active faults in California, including the Maacama-Garberville Fault (MGF), the Rodgers Creek Fault (RC), the Hayward Fault (HF), the Calaveras Fault (CF), the Garlock Fault (GF), the East California Shear Zone, the San Jacinto Fault (SJF), the Elsinore Fault (EF), the Palos Verdes Fault (PVF), and the Coronado Bank Fault (CBF). Cycles are seismicity as explained in Fig. 6.4.

release in the western belt weakens considerably, while energy release in the ECSZ amplifies and high energy release is distributed over the entire Mojave desert [*Li and Liu*, 2005].

6.4 Discussion and Conclusions

The results are affected by other model inputs besides the geometry of the SAF, noticeably viscosity of the lower crust and uppermost mantle, and the ratio between the cohesion of the upper crust outside and within the fault zone. High viscosity of the lower crust and upper mantle (>1021 Pa s), and low cohesion ratio (<2) tend to cause more relative plate motion to be absorbed outside the SAF, thus weaken its geometrical impact. Within reasonable ranges of viscosity (4×1019 Pa s - 1021 Pa s) and cohesion ratio (>2), the main features of model results remain the same. The along-strike variation of the geological slip rates are best fit with a lower crust and mantle viscosity of ~2×1020 Pa s (Fig. 6.3), which is higher than the viscosity (~1019 Pa s) estimated from postseismic relaxation studies [*Kenner and Segall*, 2000; *Pollitz et al.*, 2001]. This may be due to the much longer timescale (> 10^3 years) considered in this model than that for postseismic studies (days to decades). As *Pollitz* [2003] has shown, the effective viscosity of upper mantle may increase as much as two orders of magnitude when the timescale of deformation increases.

The model results provide useful insights into the observed along-strike variation of slip rate, stress, and seismicity, much of those may reflect the geometrical impact of the SAF. The relatively straight segments of central and northern SAF help to explain the relatively high slip rates and seismicity that clusters to the SAF main-trace. Each

trans-compressive bending of the SAF causes high stress and high energy release, which are consistent with the clustered seismicity south of the Bay Area and the broad distribution of seismicity in southern California.

Although the model includes only the main trace of the SAF, the coincidence of the resulting spatial pattern of plastic energy release with many of the secondary faults in southern California and the ECSZ (Fig. 6.5) suggests that these faults may be genetically related to the geometry of the SAF, as suggested by others [Du and Aydin, 1996]. This may reflect the natural evolution of the plate boundary zone in searching for the most efficient way to accommodate the relative plate motion. Thus the initiation of the San Jacinto fault straightens the southern SAF and eases plate motion in this part of California, and the ECSZ, which absorbs 9-23% of the relative plate motion [Dokka and Travis, 1990], makes up some of the fault slip deficiency caused by the Big Bend. If the ECSZ further weakens, it may eventually replace the SAF as a straighter and hence more efficient fault zone to accommodate the North American-Pacific plate motion.

6.5 Acknowledgments

6.6 References

Becker, T.W., J.L. Hardebeck, and G. Anderson, Constraints on fault slip rates of the southern California plate boundary from GPS velocity and stress inversions, *Geophys. J. Int.*, *160*, 634-650, 2005.

Bennett, R.A., A.M. Friedrich, and K.P. Furlong, Codependent histories of the San Andreas and San Jacinto fault zones from inversion of fault displacement rates, *Geology*, *32*, 961-964, 2004.

Bennett, R.A., W. Rodi, and R.E. Reilinger, Global positioning system constraints on fault slip rates in southern California and northern Baja, Mexico, *J. Geophys. Res.*, *101* (B10), 21943-21960, 1996.

Bird, P., and X. Kong, Computer simulations of California tectonics confirm very low strength of major faults, *GSA Bull.*, *106* (2), 159-174, 1994.

DeMets, C., R.G. Gordon, D.F. Argus, and S. Stein, Effect of recent revisions to the geomagnetic reversal time scale on estimates of current plate motion, *Geophys. Res. Lett.*, *21*, 2191-2194, 1994.

Dokka, R.K., and C.J. Travis, Role of the eastern California shear zone in accommodating Pacific-North American plate motion, *Geophys. Res. Lett.*, *17* (9), 1323-1326, 1990.

Du, Y., and A. Aydin, Is the San Andreas big bend responsible for the landers earthquake and the Eastern California shear zone?, *Geology*, *24* (3), 219-222, 1996.

Duan, B., and D.D. Oglesby, Multicycle dynamics of nonplanar strike-slip faults, *J. Geophys. Res.*, *110*, B03304, 2005.

Fialko, Y., L. Rivera, and H. Kanamori, Estimate of differential stress in the upper crust from variations in topography and strike along the San Andreas fault, *Geophys. J. Int.*, *160* (2), 527-532, 2005.

Fitzenz, D.D., and S.A. Miller, New insights on stress rotations from a forward regional model of the San Andreas fault system near its Big Bend in southern California, *J. Geophys. Res.*, *109*, B08404, 2004.

Griffith, W.A., and M.L. Cooke, How sensitive are fault-slip rates in the Los Angeles basin to tectonic boundary conditions?, *Bull. Seismol. Soc. Am.*, *95* (4), 1263-1275, 2005.

Hager, B.H., Mantle viscosity: A comparison of models from postglacial rebound and from the geoid, plate driving forces, and advected heat flux, in *Glacial Isostacy, Sea Level and Mantle Rheology*, edited by R. Sabadini, K. Lambeck, and E. Boschi, pp. 493-513, Kluwer Academic Publishers, London, 1991.

Kenner, S.J., and P. Segall, Postseismic deformation following the 1906 San Francisco earthquake, *J. Geophys. Res.*, *105* (6), 13,195-13,209, 2000.

Lachenbruch, A.H., and J.H. Sass, Heat flow and energetics of the San Andreas fault zone, *J. Geophys. Res.*, *85* (B11), 6185-3222, 1980.

Li, Q., and M. Liu, Interaction between the San Andreas and San Jacinto faults in southern California: A 3D numerical model, *Eos Trans. AGU*, *86* (52), Fall Meet. Suppl., Abstract S53A-1087, 2005.

Li, Q., M. Liu, and A. Sandvol Eric, Stress Evolution Following the 1811-1812 Large Earthquakes in the New Madrid Seismic Zone, *Geophys. Res. Lett*, *32* (L11310), doi:10.1029/2004GL022133, 2005.

Meade, B.J., and B.H. Hager, Block models of crustal motion in southern California constrained by GPS measurements, *J. Geophys. Res.*, *110* (B3), B03403, 2005.

Parsons, T., Tectonic stressing in California modeled from GPS observations, *J. Geophys. Res.*, *111*, doi:10.1029/2005JB003946, 2006. (in press)

Pollitz, F.F., Transient rheology of the uppermost mantle beneath the Mojave Desert, California, *Earth and Planet. Sci. Lett.*, *215* (89-104), 2003.

Pollitz, F.F., C. Wicks, and W. Thatcher, Mantle flow beneath a continental strike-slip fault; postseismic deformation after the 1999 Hector Mine earthquake, *Science*, *293* (5536), 1814-1818, 2001.

Smith, B., and D. Sandwell, Coulomb stress accumulation along the San Andreas Fault system, *Journal of Geophysical Research-Solid Earth*, *108* (B6), 2003.

Williams, C.A., and R.M. Richardson, A rheological layered three-dimensional model of the San Andreas Fault in central and southern California, *J. Geophys. Res.*, *96*, 16597-16623, 1991.

Chapter 7   INTERACTION BETWEEN THE SAN ANDREAS AND SAN JACINTO FAULTS IN SOUTHERN CALIFORNIA: A 3D NUMERICAL MODEL

Qingsong Li and Mian Liu

Abstract. The San Andreas Fault (SAF) and San Jacinto Fault (SJF) are the most important faults in southern California, absorbing ~75% relative motion between the Pacific plate and North American plate. Geological and geodetic observations show that the fault slip rates on these two faults may be strongly covariant after the initiation of the SJF. It has been proposed that the SJF was formed at 1.5-1 Ma ago and much younger than the SAF. As the SJF accumulates more fault slip, it may become weaker according to previous studies, which suggest that mature faults are weaker than nascent faults in California plate boundary zone. In this study, we apply a 3D dynamic finite element model to simulate fault slip on these two faults using several possible stages of the SJF evolution, which include: 1, before the initiation of the SJF; 2, the SJF is much stronger (3 times) than the SAF; 3, the SJF is moderately stronger (2 times) than the SAF; 4, the SJF is as strong as the SAF. The modeled fault slip rates in different stages are comparable to different arguments of fault slip rates on these two faults. This comparability suggests that the argued fault slip rates may exist at different evolution stages of the SAF and SJF system. The fault slip rate partitioning on these two faults observed by GPS inversion studies indicates that the SJF is presently much stronger than the SAF. The model results also show that the initiation and evolution of the SJF may have caused the observed westward movement of deformation belt in the East California Shear Zone (ECSZ).

7.1 Introduction

The SAF and SJF are the most important faults in southern California, absorbing 35-40 mm/yr out of ~49mm/yr relative fault motion between the Pacific plate and North American plates (Fig. 7.1). However the accurate fault slip rates on these two faults are still under intense debates. Based on geological and geodetic observations, one kind of arguments places ~20-26 mm/yr on the Indio segment of the SAF, ~9-15 mm/yr on the SJF, and ~15 mm/yr on the San Bernardino Mountains (SBM) segment of the SAF. The other kind of arguments places ~15-20 mm/yr on both the Indio SAF and the SJF, and ~5-10 mm/yr on the SBM segment. (see summaries in Becker et al. [2005]).

The apparent discrepancy between geological and geodetic fault slip rate estimations may be partially reconciled by time varying fault slip rates [*Bennett et al.*, 2004]. It has been concluded that secular variations in slip rate may be the rule, rather than the exception, on most faults [*Chevalier et al.*, 2005]. In Bennett et al's model [2004]: the slip rate on the SAF decelerated from ~35 mm/yr at 1.5 Ma to as low as 9±4 mm/yr by 90 ka. Over this same time period, the rate on the SJF accelerated from an initial value of zero to a rate of 26±4 mm/yr. The rate of the SAF accelerated since ca. 90ka, from ~9 mm/yr to the modern rate of 27±4 mm/yr, whereas the SJF decelerated from 26±4 mm/yr to the modern rate of 8±4 mm/yr.

One of the possible reasons to cause the time-varying fault slip rates in southern SAF system may be the initiation and evolution of the SJF. The initiation of the SJF is proposed to be between 1.5 and 1.0 Ma with geological and stratigraphic evidences [*Albright*, 1999; *Dorsey*, 2002; *Morton and Matti*, 1993], and coincides roughly with the formation of a major restraining bend in the southernmost SAF [*Matti and Morton*, 1993; *Morton and*

Matti, 1993]. As the SJF accumulates more fault slip, it may become weaker according to previous studies, which suggest that mature faults are weaker than nascent faults in California plate boundary zone [*Bird and Kong*, 1994].
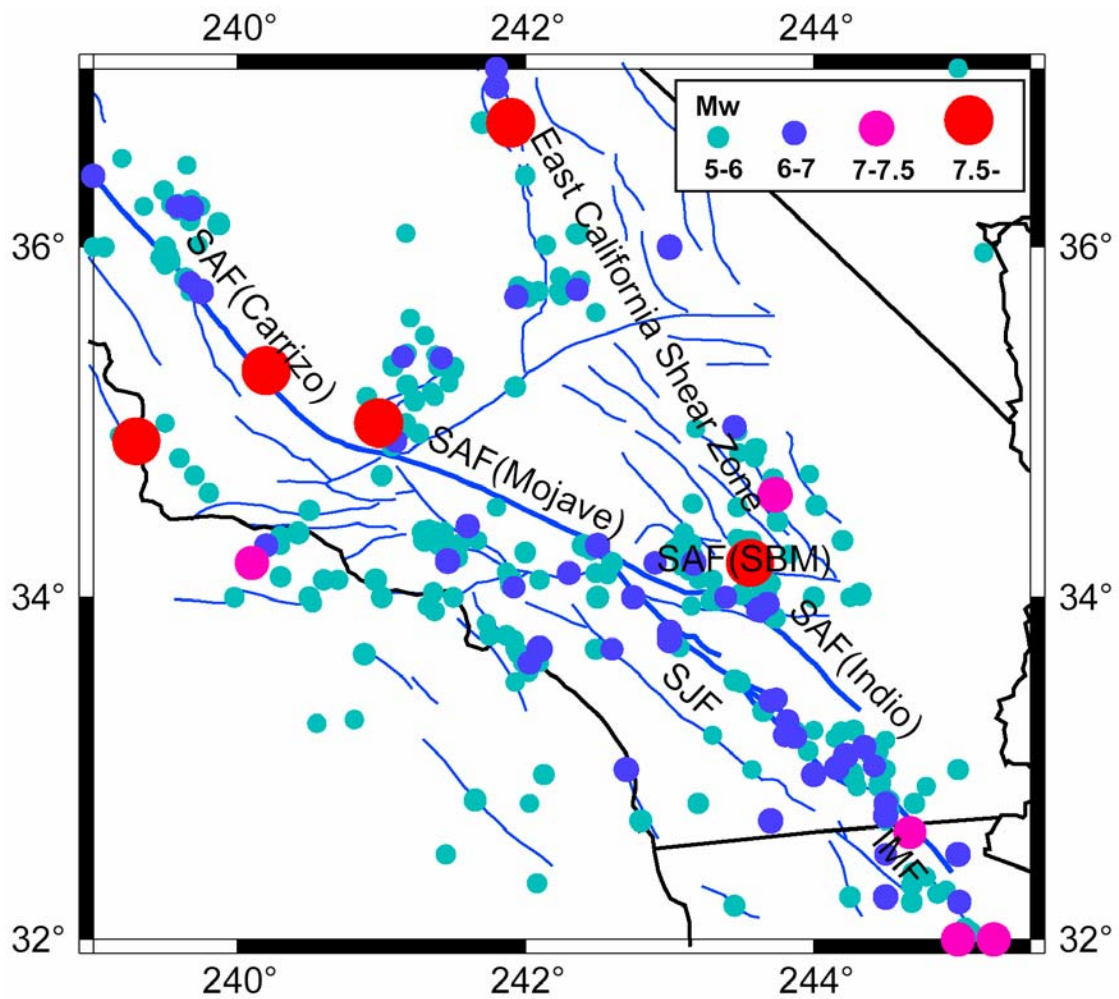
Figure 7.1 Active faults and seismicity in southern California. Fault traces are taken from SCEC Fault Map. San Andreas Fault (SAF), San Jacinto Fault (SJF), and Imperial Fault (IMF) are labeled in the figure. The seismicity data are from NEIC catalog. It includes M>5.0 earthquakes from 1800-present.

Numerous dynamic models have been introduced to simulate formation and slip of normal and strike-slip faults [*Griffith and Cooke*, 2005; *Hetzel and Hampel*, 2005; *Lavier*

and Buck, 2002; *Lavier et al.*, 2000; *Li and Liu*, 2005; *Roy and Royden*, 2000a; *Roy and Royden*, 2000b]. Many of these models are two dimensional finite element models in transection view. They have been used to explore factors controlling formation of fault zones, and/or to explain geodetically observed fault slip rates with vertically varying rheological structure. The effect of laterally varying fault geometry and spacing are neglected. Three dimensional boundary element models are very suitable for exploring fault slip in a complex fault system [*Griffith and Cooke*, 2005]; however, they are not capable to incorporate anelastic deformation of ambient upper crust outside fault plane, while incorporating anelastic deformation is very important to avoid pathological stress buildup in ambient upper crust in long time scale dynamic modeling.

In this study, we apply the dynamic visco-elasto-plastic finite element model developed by Li and Liu [2005], which is capable to incorporate non-planar fault geometry and an-elastic deformation in ambient crust, to study how the interaction between the SAF and SJF affects fault slip rates and deformation in southern California.

7.2 Numerical Model

The model is dimensioned with 800km in length and 500km in width, covering the southern California region (Fig. 7.2). The SAF and SJF in the model have realistic surface traces and dip at 90 degree. The model consists of a 20 km thick elasto-plastic layer (non-associated Draker-prager model), which represents upper crust. The model also consists of a 40 km thick visco-elastic layer (linear Maxwell model) representing lower crust and uppermost mantle. The young's module and poison's ratio are 8.75×1010 Pa and 0.25, respectively, for the whole model region. The viscosity for lower crust and upper

mantle is set to be 2.0×1020 Pa s [*Li and Liu*, 2005]. The ambient upper crust has cohesion

of 50 MPa and internal frictional coefficient of 0.4. The faults in the upper crust are

simulated with 4 km thick plastic layers with zero internal frictional coefficients. The

cohesion for the SAF is 10 MPa, which shows a weak fault and is in the range constrained

by surface heat flux measurements [*Lachenbruch and Sass*, 1980]. The cohesion for the

SJF varies in different model cases representing different evolution stages of the SJF.

Boundary conditions are applied to simulate right lateral shear between the Pacific plate

and North America plate (Fig. 7.2). Gravitational force is neglected in the model.
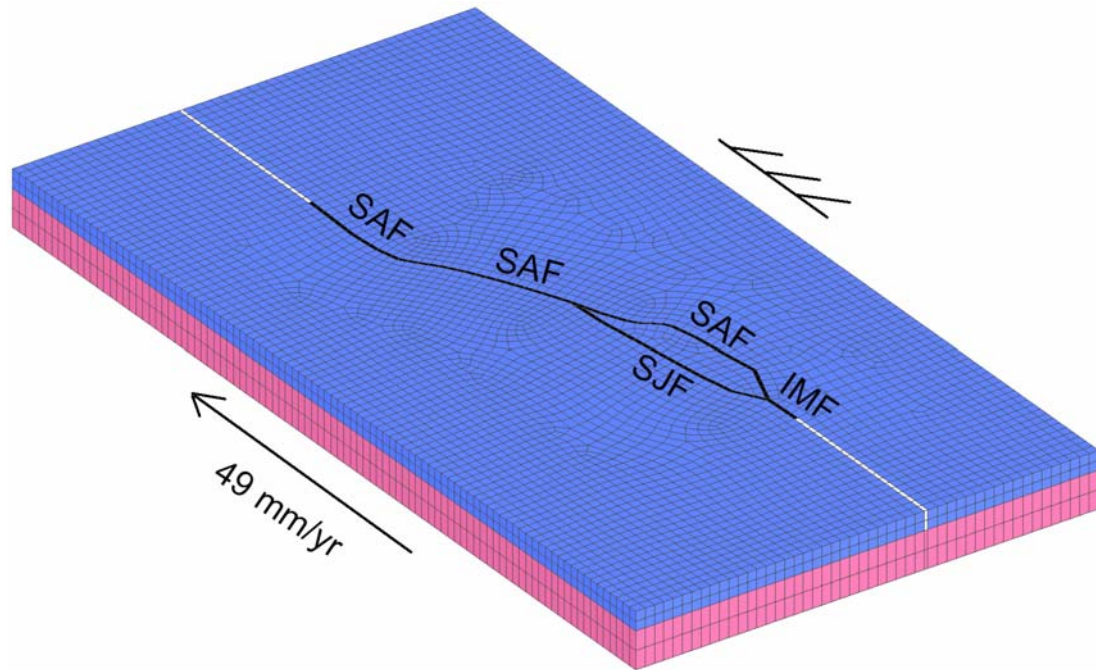

Figure 7.2 Finite element model with boundary conditions.

The model calculation is started with zero initial stress. The boundary displacement is

applied continuously in 10-year time steps. The stress and strain in the model evolves with

model time (Fig. 7.3): first, the stress in the model increases linearly with time and

bypasses the strength of the fault after 20,000-year model time; second, the faults start to slip (creep). And the stress in ambient upper crust increases nonlinearly; third, the fault slip rates increase continuously, and the stresses in some regions bypass the strength of the ambient upper crust; finally, both fault slip rates and stresses in the model get to a steady state. The model results at the steady state are believed to reflect the secular fault slip in a time period with specified fault properties.
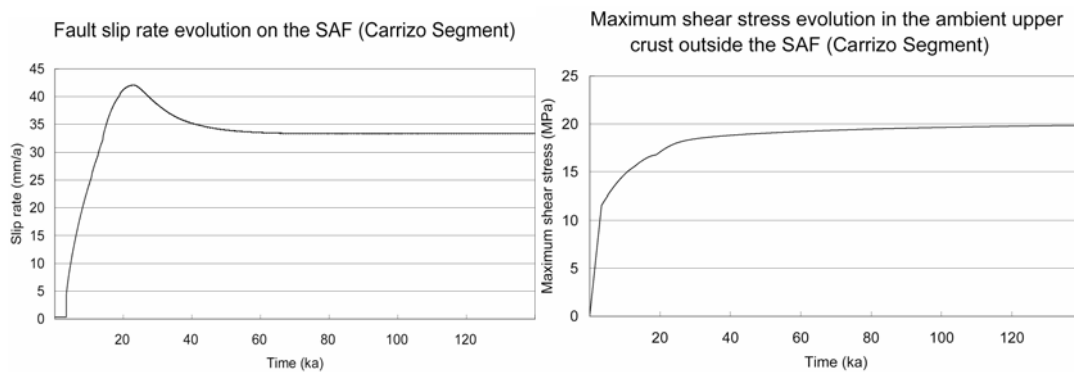
Figure 7.3 An example showing slip rate/stress evolution under continuous plate boundary loading.

7.3 Model Results

We have performed calculations with different model inputs, which reflect possible evolution stages of the SJF. The stages we explored include: 1, before the initiation of the SJF; 2, the SJF is much stronger (3 times) than the SAF; 3, the SJF is moderately stronger (2 times) than the SAF; 4, the SJF is as strong as the SAF. The predicted fault slip rate patterns are contrasted with geological and geodetic observations.

7.3.1 Before the initiation of the SJF

The SJF is not explicitly incorporated in the model in this case. The cohesion and frictional coefficient of the SJF are assumed to be the same as ambient upper crust. The model predicts high slip rates (~30mm/yr) on the southernmost SAF (Fig. 7.4a), which is close to the upper bound of geological fault slip rate estimation. Also the model predicts high slip rate on the SAF Mojave segment (~25mm/yr) and SAF SBM segment (~17mm/yr). These two predictions are higher than slip rates from geodetic observations and lower than the highest geological observations. One proposed explanation for the discrepancy between geological and geodetic slip rates is postseismic relaxation effect [*Savage and Lisowski*, 1998]. Another possible explanation is time varying fault slip rates, which may be a common phenomenon on major faults [*Chevalier et al.*, 2005]. On the other hand, these are the highest predictions in all the cases (evolution stages of the SJF) we studied. We suggest that the highest fault slip rates on the southern SAF could have occurred before the initiation of the SJF.

Because of the non-planar fault geometries of the SAF and SJF, the relative plate motion between the pacific plate and the North American plate can not be fully absorbed by the SAF and SJF. The remaining part of the relative plate motion occurs on other secondary faults. In the model, we use plastic deformation in the ambient upper crust to roughly simulate deformation caused by the slip on secondary faults. The predicted plastic strain release pattern is comparable with historical seismicity in southern California (Fig. 7.4b). The model predicts two belts of concentrated plastic deformation to the northeast and southwest of the SAF. The northeast belt is located roughly at the location of East California Shear Zone (ECSZ), while the southwest belt is roughly along the trend of a

series of parallel faults, including Elsinore Fault, Newport-Inglewood Fault, Rose Canyon Fault, Palos Verdes Fault, Coronado Bank Fault and San Clemente Fault. Along the location of the SJF, the model also predicts a belt of high plastic deformation. These results indicate that the particular geometry of the SAF may have influenced the formation and activity of secondary faults in southern California.

7.3.2 The SJF is much stronger (3 times) than the SAF

We set the cohesion of the SJF to be 30 MPa, which is three times the cohesion on the SAF. The model predicts ~23mm/yr slip rates on the southernmost SAF, ~14 mm/yr on the SBM segment of the SAF, ~24 mm/yr on the Mojave segment of the SAF, and ~11mm/yr on the SJF (Fig. 7.5a). The predicted slip rates are slightly lower than the slip rates on the SAF in case 1, i.e. before the initiation of the SJF. However, the predicted slip rates on the SAF are still higher than the slip rates on the SJF in this case.

The predicted fault slip rates on both the southern SAF and the SJF are close to the first kind of estimations summarized in Becker et al. [2005]. The slip rates are also comparable with the block model results from GPS and/or stress inversion studies [*Becker et al.*, 2005; *Meade and Hager*, 2005], although the slip rates on the SBM segment and Mojave segment of the SAF are ~10 mm/yr higher. This slip rate discrepancy may have been caused by postseismic effects [*Savage and Lisowski*, 1998] or temporal variation of slip rates. The comparability with geodetic fault slip rate estimations may indicate that the SJF at present is much stronger than the SAF. This conclusion looks reasonable given that the SJF is much younger than the SAF, whereas Kong and Bird [1994] proposed that mature SAF may be weaker than other nascent secondary faults in southern California.
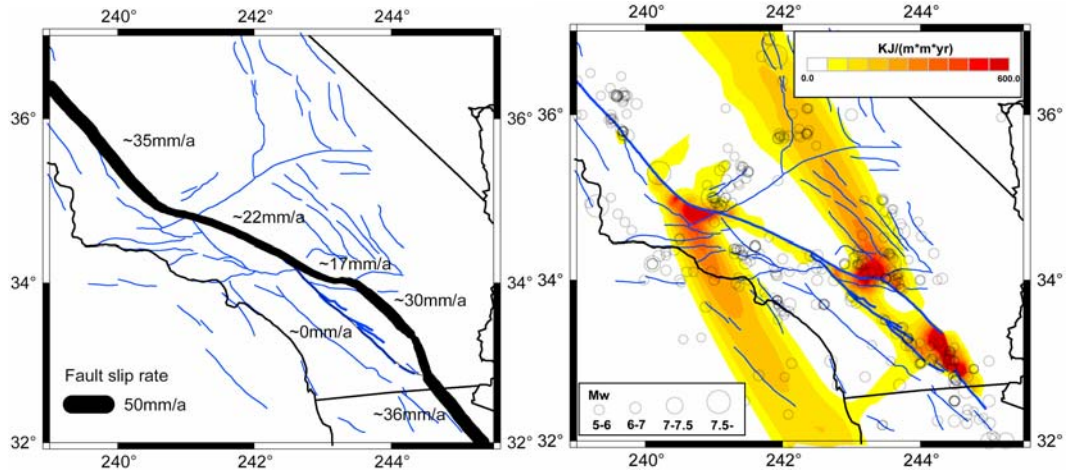
Figure 7.4 Predicted slip rates (a) and an-elastic deformation (b) before the initiation of the SJF.
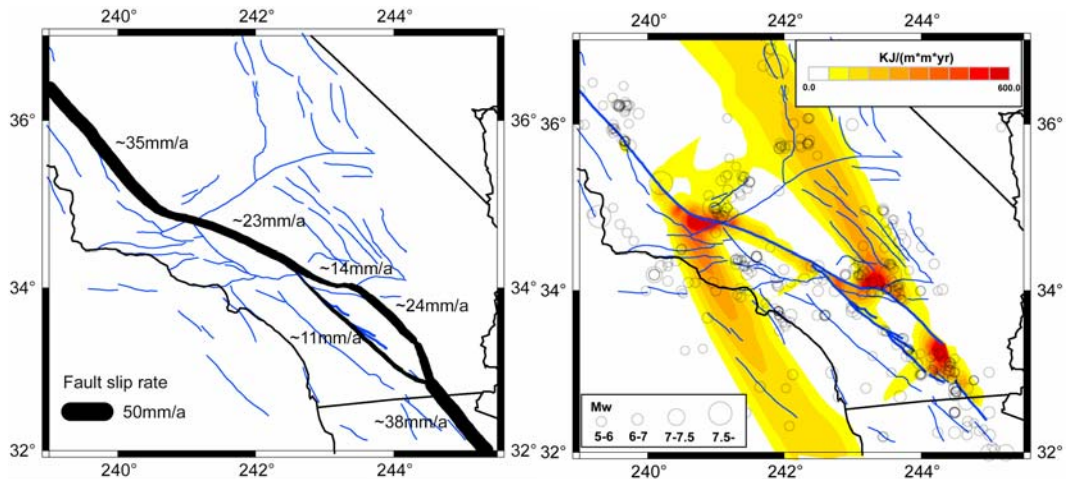
Figure 7.5 Predicted slip rates (a) and an-elastic deformation (b) if the SJF is much stronger (3 times) than the SAF.

The predicted plastic strain release pattern looks almost the same as that in case 1 (Fig.

7.5b); however, the pattern difference caused by the initiation of the SJF is still noticeable.

The plastic deformation belt along SJF disappears, while most of the an-elastic

deformation moves on the SJF. The plastic deformation belt along the ECSZ becomes a

118

little more diffused. The plastic deformation to the southwest of the SAF decreases a little bit. These findings indicate that the initiation of the SJF may have caused second order effect on the deformation pattern in southern California.

7.3.3 The SJF is moderately stronger (2 times) than the SAF

In this case, the model predicts roughly identical slip rates on the southernmost SAF and the SJF (~19mm/yr) (Fig. 7.6a). Also the model predicts ~10 mm/yr slip rates on the SBM segment of the SAF, and ~23 mm/yr on the Mojave segment of the SAF. These predictions are close to the second kind of estimations as summarized by Becker et al. [2005]. These results plus the results in case 2 indicate that the two kinds of estimated fault slip rates may both possibly have existed in the past if the fault strength on the SJF had evolved from much stronger to moderately stronger than the SAF.

The change of plastic deformation pattern continues the trend as in case 2 (Fig. 7.6b): the plastic deformation in ECSZ is more diffused and the plastic deformation to the southwest of the SAF becomes less. In these ways, the impact of the SJF on the deformation pattern in southern California becomes larger.

7.3.4 The SJF is as strong as the SAF

The model predicts higher fault slip rate on the SJF (~26 mm/yr) than that on the southernmost SAF (~11mm/yr) in this case (Fig. 7.7a). The fault slip rate partitioning on these two parallel faults is close to the estimated pattern at 90 ka after the initiation of the SJF by Bennett et al. [2004]. This consistency indicates that the strength of the SJF may be as strong as that on the SAF at that time based on the Bennett et al.'s model of time varying fault slip rates. The model predicts ~5 mm/yr slip rates on the SBM segment of the SAF

and ~22 mm/yr on the Mojave segment of the SAF, which are the lowest rates among all cases. This result indicates that one of the major impacts of the fault slip on the SJF is to reduce the slip rates on the southern SAF, which includes Mojave segment, SBM segment, and Indio segment (or named Cochella segment or Salton Sea segment).
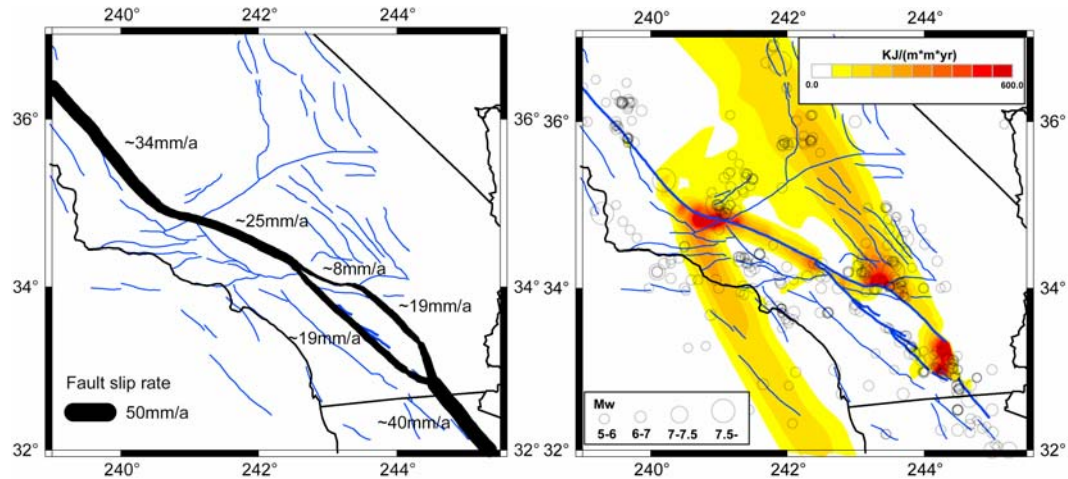
Figure 7.6 Predicted slip rates (a) and an-elastic deformation (b) if the SJF is moderately stronger (2 times) than the SAF.

The plastic deformation pattern change in the ambient upper crust continues the trend in case 2 and 3 (Fig. 7.7b). The deformation along the ECSZ in this case becomes the most diffused. The plastic deformation to the southwest of the SAF becomes the least. The evolution of plastic deformation from case 1 to case 4 indicates that the initiation and activation of the SJF may cause the diffusing of the ECSZ deformation belt and less deformation along the coastal region of the southern California.
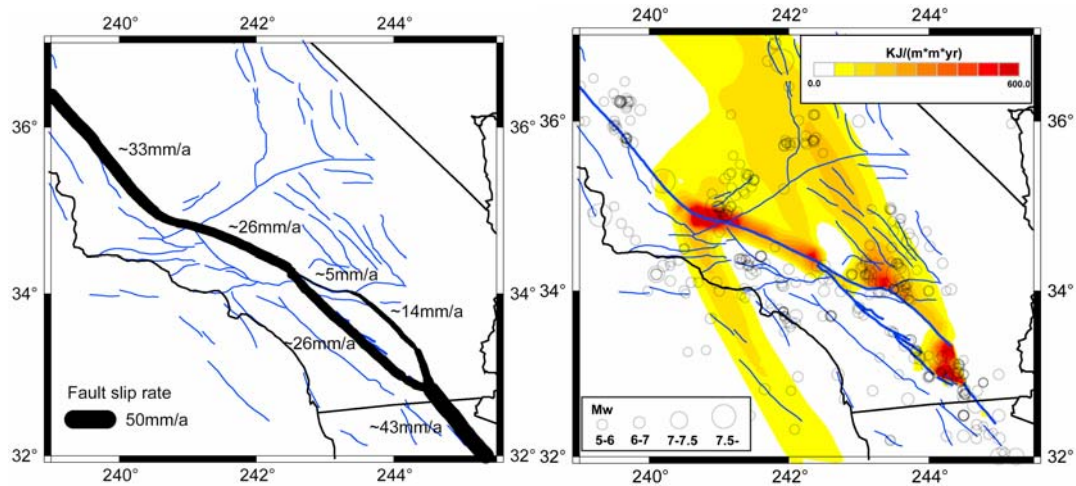
Figure 7.7 Predicted slip rates (a) and an-elastic deformation (b) if the SJF is as strong as the SAF.

7.4 Discussion

The viscosity of lower crust and upper mantle is chosen to be 2.0×1020 Pa s, which is between ~ 1019 Pa s derived from postseismic relaxation studies [*Kenner and Segall*, 2000; *Pollitz et al.*, 2001] and ~ 1021 Pa s from postglacial rebound studies [*Hager*, 1991]. We have tried a range of viscosities from 1019 Pa s to 1021 Pa s. We found that the predicted fault slip rates are sensitive to the viscosity in the lower crust and uppermost mantle. High viscosity causes low fault slip rates both on the SAF and on the SJF, and vice versa. With the viscosity of 2.0×1020 Pa s, the model predicts ~ 34 mm/yr slip rates on the Carrizo segment of the SAF in all the above cases. This prediction is close to geological and geodetic estimations [*Argus and Gordon*, 2001; *Meade and Hager*, 2005; *Minster and Jordan*, 1987; *Sieh and Jahns*, 1984]. As we know, the slip rates on this site may be most reliable and have less debate.

We simulate secular fault slip with continuously fault creeping instead of stick-slip

fault movement, while this study mainly focuses on long term fault slip rates, which can be seen as an average among many earthquake cycles. The stick-slip behavior of faults may have different effects on long term fault slip rates than that continuously fault creeping has; however, it is uncertain how much the difference can be. Here, we assume that fault strength, geometry and spacing may have the first order impacts on fault slip rates while the stick-slip behavior has only second order impacts. This assumption seems to work given the comparability between our model results and geological/geodetic estimations.

We calculate fault slip rates in steady state, without considering the transient effects caused by time varying fault strength. A sudden change of fault strength may cause high or low transient slip rates in a time period following the strength change. The length of the time period may vary from thousands to tens of thousands of years given a lower crust and upper mantle viscosity of 10^{19} Pa s to 10^{21} Pa s. The observed geological and geodetic slip rates may include transient components if fault strength varies with time. However, as we compare our model results with geological and geodetic estimations, we have assumed that the transient components are only a small portion of slip rate estimations. The assumption may hold given that the fault strength changes smoothly on the SJF in the last 1.0-1.5 Ma.

With constraints from Garlock fault geometry and GPS observations, Gan et al. [*Gan et al.*, 2003] suggested that deformation across the western part of the shear zone started ~1.6 Ma later than the eastern part. Our model results show similar westward migration of deformation in the ECSZ after the initiation of the SJF. This similarity suggests that the initiation of the SJF may have significant impacts on the evolution of the ECSZ.

7.5 Conclusions

The geometry of the SAF, especially its Big Bend in South California, would have caused a stress and strain energy field favorable for initiation and growth of the SJF. Once the SJF has initiated, it causes decrease of fault slip rate on the southernmost SAF. The initiation of the SJF also causes less strain energy release rate in regions to the west of the SJF, and diffuses a belt of concentrated strain energy along the ECSZ. By comparing model predictions with geodetic estimations of fault slip rates, we suggest that the fault strength on the SJF at present is much larger than that on the SAF. The comparability between model predictions and geological/geodetic estimations also suggests that initiation of new faults and fault strength changes may cause temporal varying fault slip rates, which may partly explain discrepancy among geodetic and geological estimations.

7.6 Reference

Albright, L.B., Magnetostratigraphy and biochronology of the San Timoteo Badlands, Southern California, with implications for local Pliocene-Pleistocene tectonic and depositional patterns, *Geol. Soc. Am. Bull.*, *111*, 1265-1293, 1999.

Argus, D.F., and R.G. Gordon, Present tectonic motion across the Coast Ranges and San Andreas fault system in central California, *Geol. Soc. Am. Bull.*, *113* (12), 1580-1592, 2001.

Becker, T.W., J.L. Hardebeck, and G. Anderson, Constraints on fault slip rates of the southern California plate boundary from GPS velocity and stress inversions, *Geophys. J. Int.*, *160*, 634-650, 2005.

Bennett, R.A., A.M. Friedrich, and K.P. Furlong, Codependent histories of the San Andreas and San Jacinto fault zones from inversion of fault displacement rates, *Geology*, *32*, 961-964, 2004.

Bird, P., and X. Kong, Computer simulations of California tectonics confirm very low strength of major faults, *GSA Bull.*, *106* (2), 159-174, 1994.

Chevalier, M.-L., F.J. Ryerson, P. Tapponnier, R.C. Finkel, J. Van Der Woerd, H. Li, and Q. Liu, Slip-rate measurements on the Karakorum fault may imply secular variations in fault motion, *Science*, *307*, 411-414, 2005.

Dorsey, R.J., Stratigraphic record of Pleistocene initiation and slip on the Coyote Creek Fault, lower Coyote Creek, Southern California, in *Contributions to crustal evolution of the Southwestern United States*, edited by A. Barth, pp. 251-269, Geological Society of America, 2002.

Gan, W.J., P. Zhang, and Z.K. Shen, Initiation of deformation of the Eastern California Shear Zone: Constraints from Garlock fault geometry and GPS observations, *Geophys. Res. Lett.*, *30* (10), 1496, doi:10.1029/2003GL017090, 2003.

Griffith, W.A., and M.L. Cooke, How sensitive are fault-slip rates in the Los Angeles basin to tectonic boundary conditions?, *Bull. Seismol. Soc. Am.*, *95* (4), 1263-1275, 2005.

Hager, B.H., Mantle viscosity: A comparison of models from postglacial rebound and from the geoid, plate driving forces, and advected heat flux, in *Glacial Isostacy, Sea Level and Mantle Rheology*, edited by R. Sabadini, K. Lambeck, and E. Boschi, pp. 493-513, Kluwer Academic Publishers, London, 1991.

Hetzel, R., and A. Hampel, Slip rate variations on normal faults during glacial-interglacial changes in surface loads, *Nature*, *435*, 81-84, 2005.

Kenner, S.J., and P. Segall, Postseismic deformation following the 1906 San Francisco earthquake, *J. Geophys. Res.*, *105* (6), 13,195-13,209, 2000.

Lachenbruch, A.H., and J.H. Sass, Heat flow and energetics of the San Andreas fault zone, *J. Geophys. Res.*, *85* (B11), 6185-3222, 1980.

Lavier, L.L., and W.R. Buck, Half graben versus large-offset low-angle normal fault: Importance of keeping cool during normal faulting, *J. Geophys. Res.*, *107* (B6), doi:10.1029/2001JB000513, 2002.

Lavier, L.L., W.R. Buck, and A.B.N. Poliakov, Factors controlling normal fault offset in an ideal brittle layer, *J. Geophys. Res.*, *105*, 23,431-23,442, 2000.

Li, Q., and M. Liu, Geometrical impact of the San Andreas Fault on stress and seismicity in California, *Geophys. Res. Lett.*, (Submitted), 2005.

Matti, J.C., and D.M. Morton, Paleogeographic evolution of the San Andreas fault in southern California: A reconstruction based on a new cross fault correlation, in *The San Andreas fault system: Displacement, palinspastic reconstruction, and geologic evolution*, edited by R.E. Powell, R.J. Weldon, and J.C. Matti, pp. 107-159, Geological Society of America Memoir, 1993.

Meade, B.J., and B.H. Hager, Block models of crustal motion in southern California constrained by GPS measurements, *J. Geophys. Res.*, *110* (B3), B03403, 2005.

Minster, B., and T.H. Jordan, Vector constraints on western U.S. deformation from space geodesy, neotectonics, and plate motions, *J. Geophys. Res.*, *92*, 4798-4804, 1987.

Morton, D.M., and J.C. Matti, Extension and contraction within an evolving divergent strike-slip fault complex: the San Andreas and San Jacinto fault zones at their convergence in Southern California, in *The San Andreas fault system: displacement, palinspastic reconstruction, and geologic evolution*, edited by R.E. Powell, R.J. Weldon, and   J.C. Matti, pp. 217-230, Geological Society of America Memoir, 1993.

Pollitz, F.F., C. Wicks, and W. Thatcher, Mantle flow beneath a continental strike-slip fault; postseismic deformation after the 1999 Hector Mine earthquake, *Science*, *293* (5536), 1814-1818, 2001.

Roy, M., and L.H. Royden, Crustal rheology and faulting at strike-slip plate boundaries; 1, An analytic model, *J. Geophys. Res.*, *105* (3), 5583-5597, 2000a.

Roy, M., and L.H. Royden, Crustal rheology and faulting at strike-slip plate boundaries; 2, Effects of lower crustal flow, *J. Geophys. Res.*, *105* (3), 5599-5613, 2000b.

Savage, J.C., and M. Lisowski, Viscoelastic coupling model of the San Andreas Fault along the big bend, Southern California, *J. Geophys. Res.*, *103* (4), 7281-7292, 1998.

Sieh, K.E., and R.H. Jahns, Holocene activity of the San Andreas fault at Wallace Creek, California, *Geol. Soc. Am. Bull.*, *95*, 883-896, 1984.

Chapter 8   CONCLUSIONS

The most significant original works in this study include: develop a 3D parallel visco-elasto-plastic finite element model for active tectonics (In my knowledge, similar model has not existed before); mechanically test two hypotheses for the cause of intraplate earthquakes; investigate the stress/strain energy evolution in the NMSZ, which have implication for the seismic hazard assessment for NMSZ itself and surrounding regions; quantitatively compare stress/strain energy evolution in interplate and intraplate settings; simulate long term fault slip and fault interaction of the SAF system with 3D dynamic models, which improve our understanding of strike-slip plate boundary zone evolution. The main findings of these original works include the following.

(1)   The cause for intraplate earthquakes may not be an enigma. Intraplate
        earthquakes are caused by either elevated tectonic stress or weakened structure
        in fault zones. For instance, the seismicity belt in the central-eastern United
        States is located along the edge of Canadian Craton. The lithosphere thickness
        variation causes elevated stress along this belt that may be the reason for the
        seismicity. Another example is the 2001 Bhuj, India earthquake located at
        western India plate (~400 km from nearest plate boundary). The particular
        thrust-strike/slip plate boundary to the west causes elevated compressive stress
        in Bhuj region. If the intraplate structures, such as Bhuj Basin and New Madrid
        Seismic Zone, are weaker than regional crust, they will be more prone for

earthquakes.

(2)   Following large earthquakes, intraplate seismic zones (e.g., the New Madrid fault zone) tend to remain in a Coulomb stress shadow for thousands of years. On the other hand, a significant amount of the stress relieved from large intraplate earthquakes, and the associated strain energy, may migrate to and be trapped within the ambient crust, mainly near the tips of the fault zones (e.g., southern Illinois and eastern Arkansas). The elevated strain energy can be equivalent to the energy release of some middle sized earthquakes. Some present intraplate seismicity, especially middle sized earthquakes, occurs in regions with elevated stress and strain energy following large intraplate earthquakes (the NMSZ is a typical example). So part of the present seismicity in intraplate seismic zones and surrounding regions can be viewed as aftershocks of large historical intraplate earthquakes.

(3)   The above described stress and strain energy evolution in intraplate seismic zones are some of the fundamental differences from interplate settings, where the evolution of stress and strain energy are dominated by tectonic loading. Following a large interplate earthquake, the stress on the fault increases rapidly due to viscous relaxation in the lower crust and uppermost mantle. Afterwards, the stress still rapidly increases due to tectonic loading. At the same time, the stress may sudden increase an amount due to earthquakes on neighboring fault segments.

(4)   Earthquakes and faulting in interplate settings are largely controlled by fault structures, especially those of the main plate boundary fault. One typical

example is the California plate boundary zone. The observed along-strike variation of slip rate, stress, and seismicity along the SAF may reflect the geometrical impact of the SAF. The relatively straight segments of central and northern SAF helps to explain the relatively high slip rates and seismicity that clusters to the SAF main-trace. On the other hand, each trans-compressive bending of the SAF causes high stress and high energy release, which is consistent with the clustered seismicity south of Bay Area and the broad distribution of seismicity in southern California.

(5)   The faults in plate boundary zones dynamically interact with each other that may reflect the natural evolution of the plate boundary zone in searching for the most efficient way to accommodate the relative plate motion. For instance, the geometry of the SAF, especially the Big Bend in southern California, causes a stress and strain energy field favorable for initiation and growth of the SJF. Once the SJF has initiated, it causes decrease of fault slip rate on the southernmost SAF. The initiation of the SJF straightens the southern SAF and eases plate motion in this part of California. The initiation of the SJF also causes less strain energy release rate in regions to the west of the SJF, and focus strain energy in the Mojave Desert and along the East California Shear Zone, consistent with the spatial distribution of earthquakes in southern California.

VITA

Qingsong Li was born January 9, 1975 (Chinese Lunar Calendar), in Peng'an County, Sichuan Province, People's Republic of China. After attending high school in Sichuan Province, he received the following degrees: B.S. in Geology from Beijing University at Beijing, China (1996); M.S. in Geophysics from Beijing University (1999); Ph.D. in Geophysics from the University of Missouri-Columbia (2006). He is married to Yin Luo of Wuhan city, China, and he is going to be a postdoctoral fellow of Lunar and Planetary Institute at Houston, Texas.